Sapienza University of Rome

Ph.D. Program in Structural and Geotechnical Engineering

Random Lattice Particle Modeling of Fracture Processes in Cementitious Materials

Candidate:
Alessandro Fascetti

Advisor:
Prof. Nicola Nisticò

Co-Advisor:
Prof. John E. Bolander

Academic Year 2014 - 2015

the earth is not a cold dead place

explosions in the sky

Abstract

The capability of representing fracture processes in non-homogeneous media is of great interest among the scientific community for at least two reasons: the first one stems from the fact that the use of composite materials is ubiquitous within structural applications, since the advantages of the constituents can be exploited to improve material performance; the second consists of the need to assess the non-linear post-peak behavior of such structures to properly determine margins of safety with respect to strong excitations (e.g. earthquakes, blast or impact loadings).

Different kinds of theories and methodologies have been developed in the last century in order to model such phenomena, starting from linear elastic equivalent methods, then moving to plastic theories and fracture mechanics.

Among the different modeling techniques available, in recent years lattice models have established themselves as a powerful tool for simulating failure modes and crack paths in heterogeneous materials. The basic idea dates back to the pioneeristic work of Hrennikoff [73]: a continuum medium can be modeled through the interaction of unidimensional elements (e.g. springs or beams) spatially arranged in different ways. The set of nodes that interconnect the elements can be regularly or irregularly placed inside the domain, leading to regular or random lattices. It has been shown [26] that lattices with regular geometry can strongly bias the direction of cracking, leading to incorrect results.

A variety of lattice models have been developed. Such models have seen a wide field of applications, ranging from aerodynamics (using Lattice-

Boltzman models [67]) to heat transfer [131], crystallography [27] and many others [44] [127] [41].

Every material used in civil and infrastructure engineering is constituted of different phases. This is due to the fact that the different features of different elements are usually coupled in order to obtain greater advantages with respect to the original constituents. Even structural steel, which is usually thought of as a homogeneous continuum-type medium, includes carbon particles that can be seen as inhomogeneities at the microscopic level. The mechanical behavior of concrete, which is the main object of the present work, is strongly affected not only by the presence of inclusions (i.e. the aggregates pieces) but also by their arrangement. For this reason, the explicit, statistical representation of their presence is of great interest in the simulations of concrete behavior. Lattice models can directly account for the presence of different phases, and so are advantageous from this perspective. The definition of such models, their implementation in a computer program, together with validation on laboratory tests will be presented. The present work will briefly review the state of the art and the basic principles of these models, starting from the geometrical and computing tools needed to build the simulations. The implementation of this technique in the Matlab environment will be presented, highlighting the theoretical background. The numerical results will be validated based on two complementary experimental campaigns,which focused on the meso- and macro-scales of concrete.

Whereas the aim of this work is the representation of the quasi-brittle fracture processes in cementitious materials such as concrete, the discussed approach is general, and therefore valid for the representation of damage and crack growth in a variety of different materials.

Acknowledgments

Foremost, I would like to express my deepest gratitude to my advisor Professor Nicola Nisticò, for his irreplaceable guidance throughout the rough times the writing of a work like this requires.

I would also like to thank Professor John E. Bolander for the time spent with me in Davis. His kindness and constant excitement about every little result obtained significantly encouraged me into improving my models.

I want to say thanks to Prof. Gianluca Cusatis for warmly welcoming me during my short, but extremely fruitful, stay in Chicago.

My dearest thoughts go to my family, my father Fernando, my mother Nella and my brother Andrea, for the support they gave me during my studies, and for reminding me so often how much they missed me. The hard and busy times that this phase of my life required have been much easier knowing that such a great family will always be behind my shoulders. I love you.

To my uncle Clemente Alessandro goes all my gratitude for helping me understand what I wanted to become and achieve in my life. I wish he could be here celebrating this goal with me.

To Federica, for teaching me so much about myself. Because every time I look into your eyes I have the feeling we have been knowing each other forever. I can not (nor I want to!) imagine my life without your smile.

My colleagues surely represented a big part of my life during the long days spent in front of my laptop. This whole period would not have been the same without Serena: our long talks and exchange of ideas on our models

have been fundamental. I also want to express my gratitude to Salvatore for the great work he did by applying my work on fiber-reinforced elements. Last but not least, Mahmoud, for teaching me that the simplest things we usually give for granted represent the most important part of our lives.

"Human beings have always been in the need to express their purest emotions through music". I am very grateful I could share these emotions with Giovanni, Jacopo and Tommaso. This makes us human.

Space-time continua, technology anomalies, explosions in the sky songs: these are just some of the things I could only share with Matteo. The different perspective on things he always points out has helped me understand so much about myself. For this he has my gratitude.

Last year was extremely hard for me. Andrea and Valeria represented my anchor in so many moments when I was feeling down. They never let me think I was going through all of that just by myself. Their support has been fundamental. Thank you.

To my house mates Tobia, Tullia and Martina, because home is where the heart is.

All the experimental work I have done could not have been possible without Engineer Michele Di Benedetto, to whom I owe so much. I hope you are in a better place now.

Last but not least, I want to thank all the friends in the United States, for making me feel home away from home. Special thanks go to: Pauline for her invaluable advices and company, Gugu for always showing me the bright side of life, Sissi for her company (and her wine!) and Alex, because a good friend is just what you need when you are far from home. All my gratitude goes to all the people I met during my time in Davis, I hope to see you guys soon.

Alessandro Fascetti

Contents

List of Figures

List of Tables

Chapter 1

Introduction and State of the Art

The ability to predict damage development in concrete members is crucial, due to the extensive use of these materials within the civil infrastructure. Moreover, the capability of simulating and predicting damage phenomena is increasingly important for both structural optimization and the definition of safety factors against strong excitations (i.e. earthquakes, blast or impact loadings). For this reason, many different theories and procedures have been developed to predict the behavior of such elements. This chapter summarizes some of the advancements in modeling fracture of concrete materials, leading up to lattice models, which are the object of this work, that established themselves as a powerful tool to model fracture processes in cementitious materials while explicitly accounting for the material structure.

Reinforced concrete (RC) technology has evolved through several key developments since the early applications at the start of the last century. The first theoretical step, which made application of the technology possible, was the "elastic no-tension" sectional analysis. This theory, under the assumption that the concrete has no tensile strength, together with the classical beam theory, permitted the diffusion of the technology; it served as the basis for most building codes, given its simplicity. However, the basic assumptions of the method (linear material behavior, neglect of post-peak behavior and bond-slip effects, etc.) did not permit the characterization of failure.

During the 1940's, plastic limit analysis was introduced on the basis of the plasticity theories [91] [121]. This new standpoint led to great advancements in analysis and design of RC structures, even with its limitations (such as the difficulties correlated to the definition of the strain-softening behavior, the objectivity of calculations and the generalization of the determination of the required parameters). Objective characterizations of failure did not come until the introduction of fracture mechanics concepts to concrete technologies, several decades later.

1.1 Historical Overview on Concrete Fracture Mechanics

Fracture mechanics provides failure theories based on energy criteria, possibly in combination with strength criteria, that account for the propagation of failure within the structure [49]. Advantages of fracture mechanics-based approaches include: the definition of energy criteria to control the evolution of the damage in the material, objectivity of the obtained results, the capability to characterize localized phenomena, and the explicit managing of size effect. For these reasons, the last four decades have witnessed the application of such theories into FEM programs and other analysis codes. It is convenient to distinguish between the three elementary fracture modes (see Fig. 1.1):

1. Mode I: Opening Mode
2. Mode II: Planar Shear Mode
3. Mode III: Antiplane Shear Mode

While Modes I and II are respectively planar symmetric and antisymmetric, Mode III is three-dimensional. Any fracture process can be seen as a composition of the three basic modes.

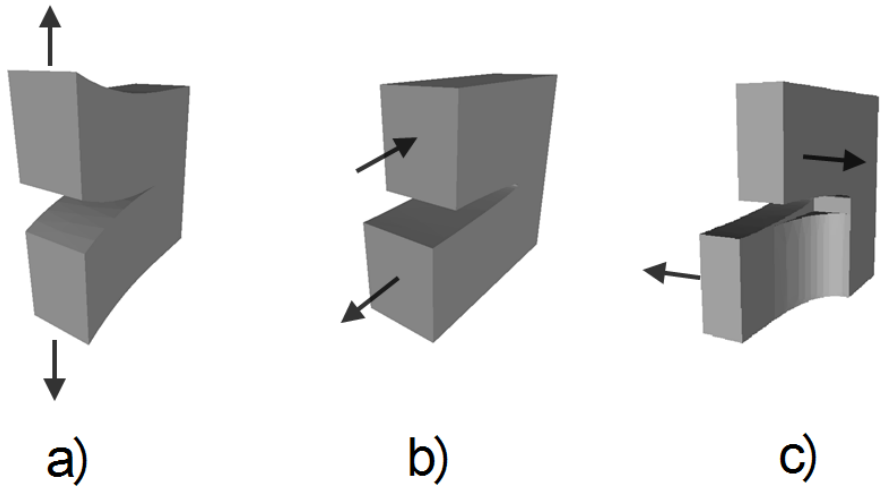

Figure 1.1: Basic fracture modes: (a) opening; (b) plane shear; (c) antiplane shear

1.2 Linear Elastic Fracture Mechanics

Modern applications of fracture mechanics to concrete materials have their origins in Linear Elastic Fracture Mechanics (LEFM). The hypothesis behind this theory is that the fracture process occurs at the crack tip, while the remaining part of the domain remains elastic, so that the problem can be solved by methods of linear elasticity. The introduction of a discontinuity (crack) inside a linear elastic body produces stress concentration at the crack tip, with the magnitude of the stress components approaching infinity as the distance from the tip tends to zero (see Fig. 1.2). This fact, recognized by Griffith [62] [63], implies that strength criteria cannot be properly used as a condition of failure. Instead, the condition of crack propagation requires an energy basis. To this end, it is possible to evaluate the energy release rate as:

$$G_b = -\frac{\partial \Pi(a)}{\partial a} \approx -\frac{1}{\Delta a}[\Pi(a + \frac{\Delta a}{2}) - \Pi(a - \frac{\Delta a}{2})] \tag{1.1}$$

in which Π is the potential energy of the structure as a function of the crack length a. The finite difference approximation given in 1.1 can be used

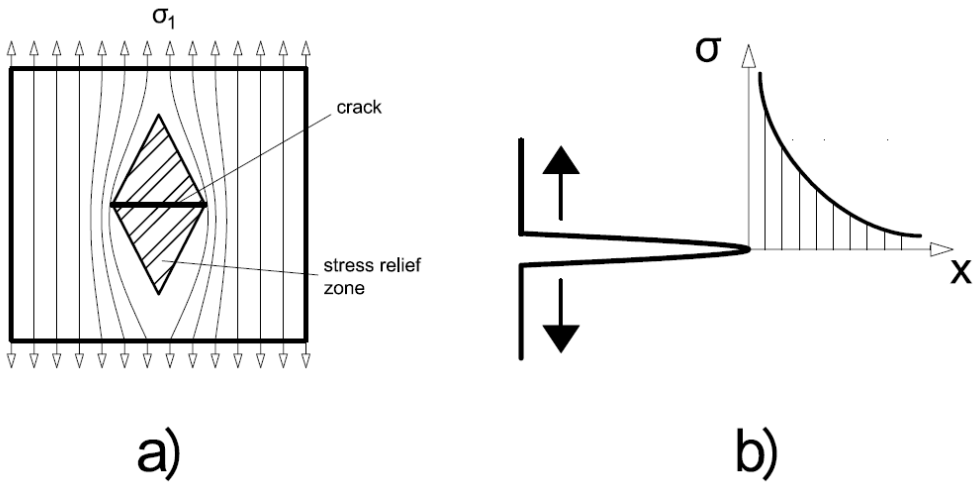

Figure 1.2: Basic assumptions for the LEFM theory: (a) principal stress trajectories; (b) stress approaching infinity at the crack tip

to evaluate the released fracture energy G by structural analysis methods. According to Griffith [62], the critical state is represented by the condition $G = G_f$, where G_f is the material fracture energy, considered as a basic material property.Crack propagation occurs when $G > G_f$.

One main problem with this approach is that fracture does not happen at a point, as the theory would suggest, but it always involves a wider "fracture process zone". The length and width of the process zone can be roughly estimated numerically or experimentally, but the method is only applicable when the fracture process zone is small compared to the dimensions of the structure in the direction of the crack trajectory. Due to the relatively large inhomogeneities within concrete, and the concomitantly large fracture process zone, this condition is not typical of most concrete structures.

1.3 Nonlinear Fracture Mechanics

The real fracture behavior of concrete differs from that of LEFM, because the Fracture Process Zone (FPZ) is sizeable and involves various toughening mechanisms that contribute to softening behavior at the macroscopic level

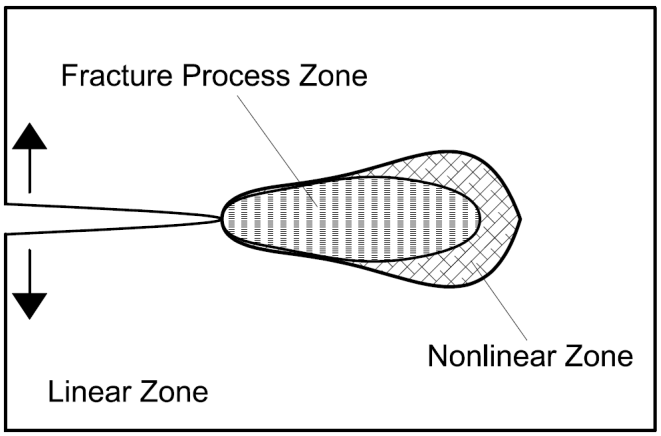

Figure 1.3: Nonlinear fracture model for concrete

(see Fig. 1.3). Nonlinear fracture models can account for such softening behavior. The first such approaches were developed by Barrenblatt [12] and Dugdale [47], with the idea that a cohesive plastic zone must exist behind the tip of the forming crack, and its (finite) length must satisfy the condition that the stress in the process zone cancels the stress singularity caused at the tip by the applied load. To this end, the crack opening can be seen as a material property. In this framework, Hillerborg and coworkers [1] [70] [71] specialized the theory to the concrete case, giving it the name of fictitious crack model. The material fracture properties are defined in terms of a stress versus crack-opening displacement relation. The area under this stress-displacement relation is directly representative of the fracture energy dissipated in the process of forming a unit area of fracture surface. The criterion used to initiate damage is based on the tensile strength of the material, and the post-peak behavior is governed by the different shapes curves that have been used in literature.

Rather than defining the damage process in terms of a stress-displacement curve, it can be advantageous to treat the discontinuity in terms of stress-strain relationship. This choice is particularly suitable when noticing that the cracks are generally tortuous (mainly because of the presence of the aggregates), and the microcracking zone does not follow a straight line. This

approach is also advantageous in computer programs because it does not require separation of the nodes along crack lines. Fracture is handled by modifying the strength and the stiffness of the elements undergoing damage processes. The *Crack Band Model* [14] uses this "smeared" approach, in which the material behavior (including strain softening) is represented by scaling the constitutive relationships within the element, usually at the element integration points, while a fixed width w_c of the crack front is imposed as a material property. The choice of a fixed crack width is due to the need of assuring that the proper energy dissipation is constant and equal to the fracture energy of the material:

$$G_f = w_c \int_0^\infty \sigma d\epsilon \tag{1.2}$$

where σ and ϵ are the stress and strain orthogonal to the crack, respectively. As already stated, the fracture is smeared over a certain width, which is considered as a material basic parameter. The so obtained fracturing strain can then be incorporated in the compliance tensor, so that, in the direction orthogonal to the crack, one obtains:

$$\epsilon = \frac{\omega\, C}{1-\omega}\sigma \tag{1.3}$$

in which ω is called the damage parameter, and can be seen as a function of the the strain normal to the crack, or the maximum principal strain. For $\omega = 0$ there is no damage, while $\omega = 1$ indicates the fully cracked state. The use of this parameter is particularly convenient in computer programs, because it allows to easily manipulate the compliance matrix in order to evaluate the new stiffness of the system.

Provided the influence of element size is properly incorporated within the strain-softening relation (see Fig. 1.4), such that energy dissipation per unit area of new fracture surface is preserved, the model results are objective with respect to mesh size [15] [17]. Smeared parallel cracks are assumed to form in the direction normal to the maximum principal stress, and this orientation may be kept fixed even if the principal stress rotates.

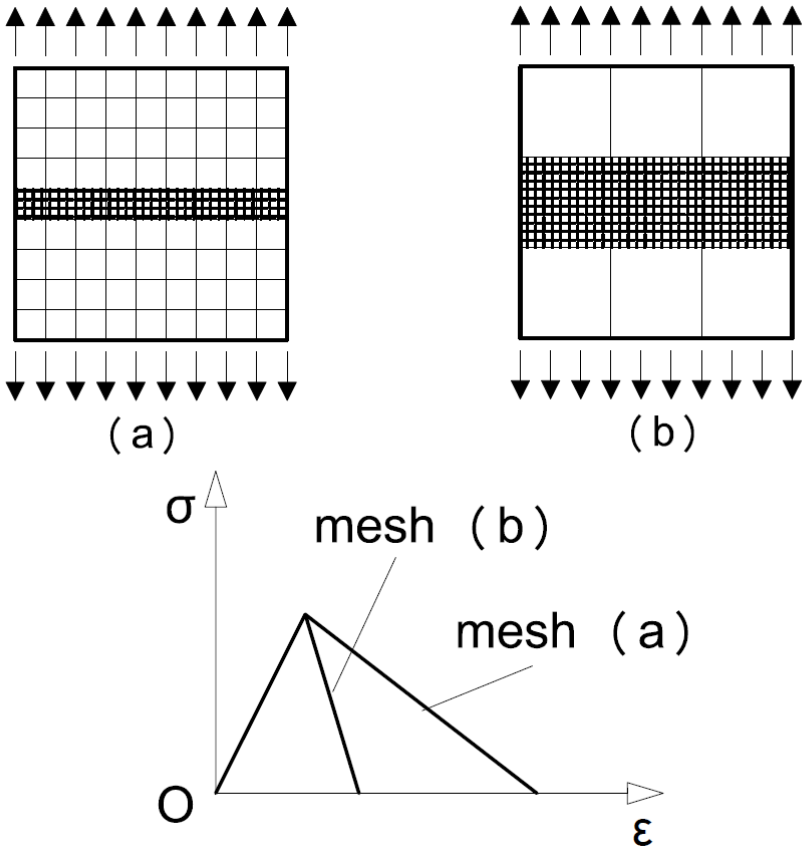

Figure 1.4: Softening branch adjusting in crack band approach

Alternatively, cracks are allowed to rotate together with the principal stress, which eliminates (or at least reduces) spurious shear stress development between the crack surfaces [66]. After fixing the shape of the softening branch, the crack band model is fully defined by three parameters: tensile strength, fracture energy and crack band width, which is approximately equal to $3\,d_a$, where d_a is the maximum aggregate size [17]. In principle, one would expect usage of finite elements of size equal to $3\,d_a$, but this is often impractical. In this case the element size can be increased, provided that the softening behavior is adjusted to preserve correct energy dissipation of the fracture process.

Fictitious crack models require that the domain is re-meshed in the case where cracking does not run along the edges of the mesh. Similarly, smeared-crack models exhibit mesh orientation bias on fracture. It is typically

impossible to avert bias generated by the user-defined mesh. Such bias can be avoided through the introduction of discontinuous strain fields along the element boundaries [95] or by introducing a nonlocal formulation of the method.

1.4 Nonlocal Theories

Nonlocal continua are material bodies whose behavior at any interior point depends not only on the state of that point, but also on the state of its neighborhood. Many works available in literature [80] [81] [50] show that nonlocality is suitable for the modeling of statistically homogeneous materials such as concrete, as it arises from micromechanical considerations. The nonlocal continuum also provides a more general solution to the problem of localization. The concept has been introduced in different forms, such as the averaging of strain over a neighborhood of the integration point [134] or the calculation of the first two spatial derivatives of the strain field in the constitutive relation [109]. In the early formulations, spatial averaging was applied on the total strain field, but that approach proved to be inconvenient from a computational standpoint. Newer versions of the theory [99] [20] [16] overcame this problem by considering the elastic strain as local (no averaging) and applying the nonlocal averaging to the softening part of the deformation, with the advantage that the continuum equation of equilibrium and boundary conditions remain the same as the local continuum ones. In terms of strains, it can be defined as follows:

$$\bar{\epsilon} = \frac{1}{V_r(\boldsymbol{x})} \int_V \alpha(\boldsymbol{s} - \boldsymbol{x}) \langle \epsilon(\boldsymbol{s}) \rangle dV = \int_V \alpha`(\boldsymbol{x} - \boldsymbol{s}) \langle \epsilon(\boldsymbol{s}) \rangle dV \tag{1.4}$$

in which

$$V_r(\boldsymbol{x}) = \int_V \alpha`(\boldsymbol{s} - \boldsymbol{x}) dV, \tag{1.5}$$

has approximately the same meaning of as the representative volume in statistical mechanics, V is the volume of the structure, $\boldsymbol{x}$ is the coordinate

vector, $\boldsymbol{s}$ is the adjacent point coordinate, α is the given weighting function of the $|\boldsymbol{s}-\boldsymbol{x}|$ distance, and $\langle\bullet\rangle = max\{\bullet, 0\}$ are the Macaulay brackets. The averaging function over a certain direction can be in principle of any shape, but it has been shown that a smooth function works well in computer programs. The Gauss function works well in principle, but it has the disadvantage of having non-null values over the entire domain. For this reason, it is convenient to use a polynomial bell function which goes to zero at a certain distance (see Fig. 1.5):

$$\begin{aligned} \alpha(\boldsymbol{s}-\boldsymbol{x}) &= \left(1-\frac{|\boldsymbol{s}-\boldsymbol{x}|}{kl}\right)^2, \quad \text{if} |\boldsymbol{s}-\boldsymbol{x}| < kl \\ \alpha(\boldsymbol{s}-\boldsymbol{x}) &= 0, \qquad\qquad\qquad\quad \text{otherwise} \end{aligned} \tag{1.6}$$

The simplest constitutive model is the one obtained by generalization of the crack band model to the nonlocal case, with or without crack rotation with the principal stress direction. Such a generalization typically does not suffer of mesh sensitivity, provided that finite elements of size less than the characteristic length are used (otherwise the method becomes formally identical to the local crack band method), and that the directional bias in the crack trajectories can be overcome by using finer meshes [16].

A remarkable example of this theory is given in [60]. The authors show how it is possible to estimate the FPZ width and the average and the dissipated energy density through lattice model simulations. They perform 3 sets of 100 random simulations each, based on the results of these tests, they show how it is possible to calibrate and validate a nonlocal continuum model.

1.5 Microplane Theories

Even if the previously described methods can realistically describe the global behavior of concrete members, they were formulated to model the material at a continuum macroscale, so that their ability to represent the effects of material structure at a lower scale is limited. Microplane models

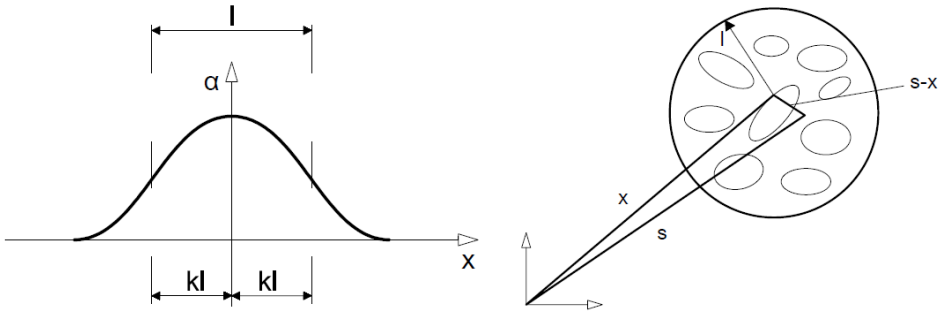

Figure 1.5: Weighting function α and graphical explanation of the nonlocal approach

take a step toward the meso-scale definition of material mechanical behavior. Such models rely on the formulation of stress-strain relationships on microplanes with different orientations, assuming either that the stresses on every plane are the components of the global stress tensor (static constraint), or that the strains on the planes are components of the global strain tensor (kinematic constraint) [122]. The global response is determined by an averaging of the various microplane responses, according to the principle of virtual work. The constitutive law involves scalar quantities, making the theory simple. The first applications to concrete were in a local form [18] and successful in simulating not only tensile tests, but also shear-dominant and other mixed-mode tests. Newer formulations of the method [97] use scalar damage theory relations to evaluate the different stress components (Volumetric, Deviatoric and Shear):

$$\sigma_V = C_V \epsilon_V,\ \sigma_D = C_D \epsilon_D,\ \sigma_T = C_T \epsilon_T \tag{1.7}$$

in which the secant stiffness moduli C_V, C_D, C_T are:

$$C_V = E_{V,0}(1-\omega),\ C_D = E_{D,0}(1-\omega),\ C_T = E_{T,0}(1-\omega), \tag{1.8}$$

with $E_{V,0}, E_{D,0}, E_{T,0}$ the initial values of the moduli. Transverse confining stress and the shear-induced expansion across cracks can also be taken into account. A nonlocal form of the microplane model has proven to be effective

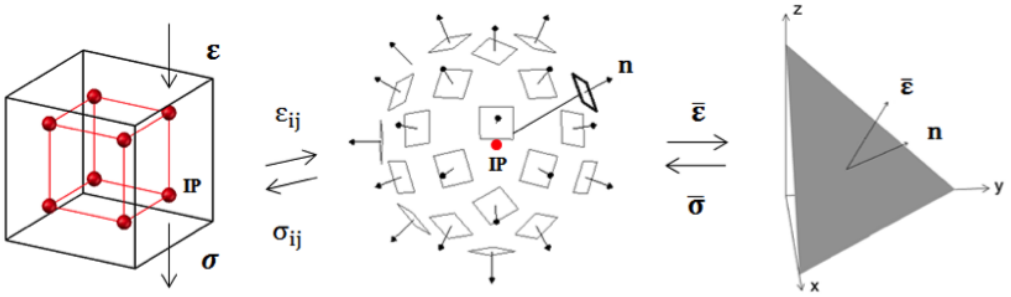

Figure 1.6: Schematic representation of the microplane model (courtesy of *S. Gambarelli*)

in modeling concrete behavior, including size effect [19]. A detailed historical perspective on these models can be found in [59].

1.6 Random Lattice Modeling

The above models, ranging from simple to sophisticated, rely on macroscopic definitions of the fields of interest (i.e. strain or stress) that provide limited insight into how structural behavior is affected by material composition and configuration, even if the models account for finer scale features. Relevant aspects of the material response may, in fact, be localized to a small region (of non-negligible dimension) depending on the statistical distribution of the matter in its neighborhood. In this sense, the direct representation of material structure is desirable. The first attempts to use this kind of approach for concrete [51] [105] [98] used the standard finite element method, subdividing each aggregate and the surrounding matrix into finite elements, with the possibility to model the weaker interface between those two phases.

With similar goals toward understanding the influence of material structure, Schlangen and van Mier proposed a model in which the continuum description was abandoned [108]. Their discontinuous, lattice representation of the material has its roots in the framework models of Hrennikoff [73]. Lattice models represent various materials, including concrete, as an assembly of simple two-node elements, such as truss, beam, or frame elements. By describ-

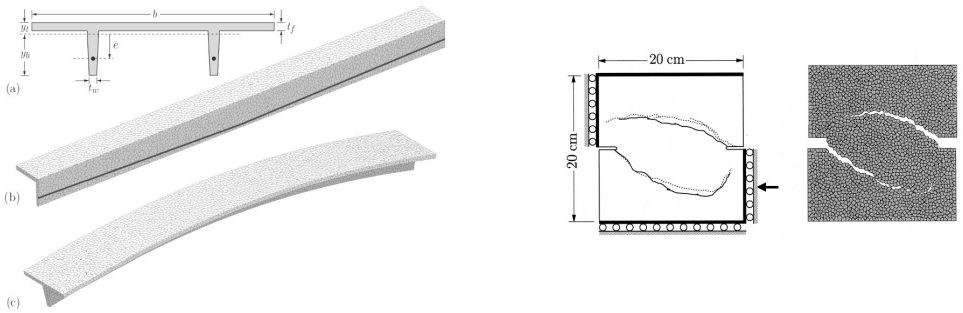

Figure 1.7: Two examples of modeled structures: (a) prestressed girder beam, (b) DEN specimen (from Yip and Bolander [87])

ing the interactions inside the domain by means of the forces arising in the two-node elements, this approach can be seen as deriving from corpuscular-molecular approaches such as Voigt's and Poincare's [126] [125] [29] [30].

In the work of Schlangen and Van Mier, a regular pattern of nodal sites was superimposed over images of the internal structure of concrete to assign different mechanical properties to the frame elements representing the different phases: aggregate, matrix, and aggregate-matrix interface. The solution process follows an event-by-event algorithm, in which a maximum of one element is broken per computational cycle, according to appropriate fracture criteria.

1.6.1 Voronoi-Based Lattice Models

This type of lattice models is based on the definition of the Voronoi tessellation of a 3-d medium. It is, in fact, the Voronoi cells that represent the geometrical arrangement of the domain. This approach is advantageous for at least three reasons: 1) the Voronoi partitioning of a 3-d domain is an efficient, well established technique, 2) these models prove efficient in the definition of non-convex media [26], 3) the average dimensions of the Voronoi cells can be of any size, making it possible to use this modeling technique in a very wide range of applications, from mesoscale ($\approx 10^{-3}$ m)

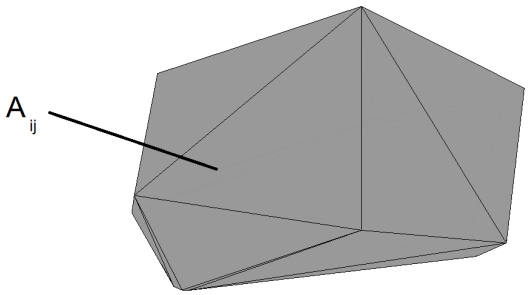

Figure 1.8: Voronoi facet common to nodes i and j

to structure-level scale ($\approx 10^2$ m). Fig. 3.5 shows a large prestressed girder beam of total length $> 10^2$ m and a double notched (DEN) specimen with dimension $\approx 10^{-1}$ m.

Although regular lattices have several attributes, including their elastic homogeneity under uniforms modes of straining, they tend to provide low energy pathways for element breaking and, therefore, can bias the cracking direction. This prompted the development and use of irregular lattices for modeling concrete fracture [26]. Bolander and coworkers [25] [74] [87] [23]construct irregular lattices by means of Delaunay/Voronoi tessellations of randomly placed nodes. The Delaunay tessellation defines the lattice topology; the dual Voronoi tessellation defines the geometrical properties of the elements. The element stiffness matrices are based on the rigid-body-spring concept of Kawai [78].

By doing so, every two adjacent cells connected by a 1-d strut (which is an edge of the Delaunay tetrahedralization) share axial and tangential forces. The stiffness of the spring inbetween the two elements is set to:

$$k_n = k_s = k_t = E\frac{A_{ij}}{h_{ij}} \tag{1.9}$$

in which k_a is the stiffness term in direction $a = n, s, t$, E is the Young's Modulus, A_{ij} and h_{ij} the area and the length of the connection, respectively. Under these hypotheses, it can be shown that the so built irregular lattice exhibits elastic homogeneity for basic modes of straining [87]. The main

disadvantage of such approach is that by imposing the same stiffness in the normal and tangential direction, the macroscopic Poisson's Ratio obtained is equal to zero. Recent works of Asahina et al. [8] overcome this disadvantage by calculating the stress and strain tensor in every node of the mesh and imposing a fictitious value of the strain that produces the Poisson effect, according to theory.

Also, by implementing a crack band approach within the lattice framework, this approach provides energy conserving, mesh insensitive simulations of concrete fracture [26].

1.6.2 Lattice Particle Models

In one notable form of lattice model, randomly placed nodes correspond to the aggregates. The distribution of aggregate size is based on the granulometric composition of concrete. This feature is appealing because with this choice, it is possible to simulate high volume fractions of inclusions while keeping the computational costs reasonable. The elements connecting the nodes represent the interactions of the aggregates together with the surrounding mortar matrix. Due to computational reasons, a threshold is chosen for the minimum size of aggregate to be modeled; any aggregate smaller than the threshold is considered to be part of the matrix. This approach is based on the general notion that a solid continuum can be represented by a collection of particles. Earlier models used such an approach for granular geotechnical materials [111] [36] and structural mechanics [78]. This approach was extensively developed through the work of Cundall et al. [37] [38] and denominated the Distinct Element Method. Zubelewicz and Bazant [137] and Bazant et al. [133] proposed a random 2D particle model composed of circular aggregates interconnected by uniaxial elements that resist only axial forces (truss elements). Whenever the circular influence zones of two aggregates intersect, they are connected by a truss element, whose area is set equal to the smallest of the two diameters of the overlap-

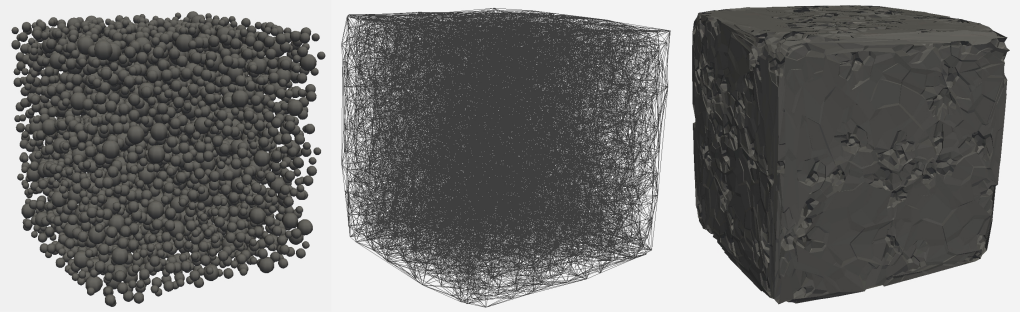

Figure 1.9: Steps required to build a lattice particle model: (a) random placement of nodal sites; (b) Delaunay triangulation of the set of points; (c) modified Voronoi diagram

ping circles. The uniaxial constitutive law exhibits strain softening, and the ultimate strain is calculated as a function of the strut length, in order to preserve the correct energy dissipation.

More recent models in this vein [58] [39] [57] [55] [56] extend the work to 3-dimensional domains, while enriching its geometrical description by using the randomly generated set of coordinates as the vertices of a Delaunay tessellation, which identifies the aggregates that share forces; the resisting and inertial properties derive from a modified Voronoi diagram for the same set of points (see Fig. 1.9). Details of how this dual complex of the Delaunay diagram is evaluated will be given in Chapter 3.

The kinematics of every aggregate (and its surrounding cell) is considered to be described by rigid body motion. Development of the constitutive relations was facilitated by the authors' experience with the microplane models [58]. There is an explicit axial-shear interaction, in order to model both the frictional and the cohesive behavior of concrete. The uniaxial response of the struts exhibits softening for tension and shear with tension/low compression cases, whereas it shows plastic hardening for compression and shear with high compression. Also, the post-peak behavior is dependent on the confining stress orthogonal to every connection, evaluated from the stress tensor, which is in turn calculated by imposing the principle of virtual work to every tetrahedron of the mesh. The principle advantages of this

technique are: the possibility to explicitly model the material meso-structure; the absence of a crack pattern directional bias (which plagues many other methods); the use of 1D elements (the lattice struts) that are characterized by simple constitutive laws, which are easy to calibrate. In particular, the unique features of this approach are represented by the capability of: 1) controlling the elastic Poisson's ratio, 2) enforcing the correct energy dissipation for mixed mode fracture processes (i.e. normal and shear interaction), 3) correctly capture compressive failure under different confinement levels. More recently, new distinctive features have been introduced [55] [56], among which the inclusion of volumetric effects in the constitutive law, a better definition of the meso-scale stresses acting on the connecting facets, improved constitutive relationship to model macroscopic behavior in compression in the presence of confinement effects, and the extension to cyclic loadings. Extensive validations have demonstrated this model's capability to represent a broad spectrum of concrete behaviors including tensile and compressive strength, cohesive fracture, size effect, and response to compression-shear and other multi-axial loads. The most recent papers in the field also proved these models to be effective for the numerical description of alkali-silica reaction (ASR) phenomena [6] and the dynamic behavior of ultra-high-performance concrete subject to projectile penetration [115].

1.7 Scope of the Work and Motivation

Considering the merits and limitations of the previously discussed modeling techniques, the present work aims to develop a lattice particle model software capable of simulating fracture within different composite materials. The main focus will be on plain concrete behavior. This is due to the fact that the correct representation of the RC behavior, which is the ultimate goal of the research, can not prescind from a reliable modeling of the plain material behavior. This modeling field is relatively new, since the first examples date back to the early 1980's, although the computational costs

were prohibitive at that time. This limitation, together with the fact that micro and mesoscale models are unusual to most engineers and researchers, hampered the widespread acceptance of such methods. For this reason, very few commercial codes include lattice modeling capabilities, making it difficult for the technique to spread among the scientific community. For all these reasons, a code has been developed in the Matlab [65] environment, making it possible to compare different approaches. In particular, two different possible modeling techniques will be presented:

- "Fully Dynamic" (FD) model: adjacent cells share not only axial forces, but also shear and bending moments. By adding shear stiffness to the constitutive law the aforementioned shortcomings can be overcome. In particular, it will be shown that by doing so it is possible to fully control the elastic properties of the material (in terms of Young's modulus and Poisson's ratio) and to simulate various multi-axial tests available in literature. Due to the choice of representing the cells displacement by means of rigid body motion, and considering the great number of particles (i.e. degrees of freedom), it is convenient to integrate the equation of motion by using an explicit integration scheme, such as the central difference method. This choice makes it possible to avoid building the system's stiffness matrix, but it requires the calculation of the inertial properties of the components, together with the mass matrix.

- "Spring Network" (SN) model: adjacent cells are connected by truss, and so they only share normal forces. This is the easiest approach in terms of constitutive representation of the material behavior, and it also requires less computational effort compared to the other two. This type of models is effective when modeling phenomena dominated by tension, but they are generally not capable of correctly representing softening post-peak behavior, nor mixed mode fracture dominated processes. An enriched constitutive law will be presented, trying to

overcome such limitations.

The results obtained with the three different approaches will be discussed and compared in Chapter 5.

Chapter 2

Concrete

Portland cement concrete is the most used construction material in construction all over the world [92]. This is due to the many appealing features it has: the economic and widespread availability of the constituents, the wide range of applications demonstrated by the many different kinds of structures it has been used for, and the relatively low maintenance required during service life. Its massive usage makes it a very important piece of modern society. Concrete is in fact the main constituents in most the structures and infrastructures we use daily to live our lives: buildings, roads, highways, railway cross-ties, piers, water pipes, dams, power stations and plants are just some of the concrete structures our everyday life relies on. To this end, it can be said that a big part of our society and civilization depends on concrete, just as the Roman Empire was relying on its forerunner.

Based on its importance in our life, it is crucial to know how concrete behaves in different situations and environments. The success of its application relies on a good understanding of its properties together with the supply of a good quality, uniform product. One important thing to keep in mind is that concrete is one of the few construction materials specifically designed for a particular project, and produced in-loco with the locally available materials. This means that the engineer has the control and the responsibility of the final result. It is common, in fact, that improper design (and production)

processes lead to poorly handled, cured and cast concrete structures, with consequent substandard performances. This means that it is necessary to put away the common idea that concrete design is an empirical science, and start analyzing the problem with the well-established mechanical and chemical principles available in literature.

Concrete is a composite material, composed of granular material (aggregate) embedded in a matrix (the cement paste). While aggregates are generally obtained from natural rock, cement can be formulated from many different chemicals. Even though cement is a generic word that applies to every kind of binders, the world is generally used to refer to *portland* cement since this variety constitutes more than the 90% of the total [90].

The possibility to cast concrete to any desired shape (e.g. arches, complex shells or massive dams) is an important characteristic that greatly influenced the advances in the technology, while on-site production helps keeping its cost down. Also, by fabricating the material on site it is possible to tailor its properties on the specific application; on the other hand the drawback of this is that the production must be carefully controlled during the construction period. Precast building elements popularity is growing a lot thanks to the higher quality control standards and easiness of construction. The main examples of precast elements are: prestressed beams and girders used for bridge construction, panels used in low-cost building systems and water pipes.

Good-quality concrete also shows excellent durability, needing limited maintenance during service time. The correct choice of aggregates, paste composition and proportions can give to the final result high physical (e.g. freeze cycles, abrasion) and chemical (e.g. dissolved sulfates or highly alkaline solutions) resistance. Its excellent fire resistance, also, makes it more suitable than other materials, such as steel, for structures that may be prone to this type of problems.

From the environmental standpoint, concrete is a good choice for most applications.In fact, it requires less energy consume than steel, mainly

because steel elements require high-temperature processes while only a relatively small part of the processes of the concrete production, the cement manufacturing, requires pyro-processing. Also, energy requirements can be decreased by incorporating supplementary cementing materials such as silica fume, slag or fly ash. Moreover, concrete buildings are usually energy efficient because of the good thermal properties of the material. Last, but not least, concrete gives designers remarkable aesthetic solutions expressed by the use of color, shape, texture making it possible to include structures in a great variety of different environments.

However, the material weaknesses must be carefully taken into account when designing structures: in particular the low tensile strength and the brittle behavior impose to reduce traction demand on the material together with the correct use of adequately anchored and designed reinforcing bars, while the low ductility involves a lower impact strength and toughness if compared to metals. Volume instability must also be allowed for in design. Irreversible shrinkage is, in fact, caused by moisture loss while the material also significantly creeps under normal service loads.

Being aware of the pros and limitations of the use of concrete permits to compensate with them by refining the design processes (i.e. the modeling of the mechanical behavior) and the production and casting technologies. A great research effort has been spent during the last years, leading to tremendous improvements in the field. The present work deals with modeling of fracture processes that may hamper the correct behavior of concrete structures.

2.1 Historical Perspective and Past Examples

The will to cement stones and rock together has always accompanied history of constructions. Builders always understood how cementing stones together would have provided them with greater flexibility and stability rather than using dry stone blocks. A very primal cementing material

was mud, as used in ancient Egypt to keep stones together. This type of material, though, only works in extremely dry environments, since it provides no resistance to water. Also Babylonians and Assyrians used naturally occurring bitumens to cement stones together.

Among all the different kinds of cements nowadays, only *hydraulic* cements will be treated, referring to them as the cements capable of hardening under water, since this type of matrices lies in the scope of the present work. These materials are based on compounds of lime (i.e. *calcareous* cements).

The first calcareous materials to be used as cement were gypsum and lime. In particular, gypsum was used by the Egyptians in the construction of the Cheops Pyramid around 3000 B.C. This material, when mixed with a little water, sets due to the recombination of calcined gypsum with the water taken off during the burning process.

Also lime mortars were used in Egypt and Greek peninsula ancient times; they are also known as *air mortars*, since the hardening happens naturally in air because of the evaporation of the mixing water. Also a carbonation reaction happens in a latter stage, solidifying the surface and preventing the carbon dioxide to penetrate. Even if this cement is insensitive to water, it does not harden in wet conditions, so it is not a hydraulic mortar. Vitruvius [100] well documented the usage of this type of cements in impressive structures, such as the Colosseum in Rome or the Pont du Gard in Nimes.

Both the Roman and Greek architects, though, knew how to make hydraulic cements, by calcining limestones containing clay. But they also knew that some volcanic deposit could be used to obtained stronger and waterproof mortars if carefully ground and mixed with lime and sand. While the Greek were using volcanic ashes from the Santorini island, Romans started using material found in the Naples Bay, in the village of Pozzuoli. For this reason, the material was called *pozzolana* and recognized for its excellent properties [100], so that it was used extensively in hydraulic infrastructures aqueducts, cisterns and piers. Architects of the time also knew how to

obtain hydraulic mortars by crushing burnt bricks. The very well known *opus caementicium*, considered as the first real concrete ever produced, was obtained with such cement, and the most impressive tribute to its quality is certainly the Pantheon. This structure, featuring a 44 m wide dome is considered the best preserved building of the ancient times [84] and is almost entirely made of concrete, poured into carefully designed ribbed sections to ensure it would properly harden.

After the fall of the Roman Empire, quality in mortars declined since the art of burning lime was almost lost. Good quality mortars appeared again around the 14^{th} century by reintroduction of pozzolanic materials, but it only was during the 18^{th} century that a rigorous study was conducted on the quality of cement. John Smeaton (who was also the first person to refer at himself as a *civil engineer*) carried out an extensive testing campaign by mixing different pozzolanes and limes, finding that high portion of clayey materials would provide better results [124].

After Smeaton's pioneering work, the whole filed saw rapid improvements. The first patent on natural hydraulic cement was issued to James Parker in 1796, while in 1824 a Leeds engineer, Joseph Aspdin, was issued to the patent for the *portland* cement. This name was given by Aspdin due to the similarity occurring between the hardened concrete and a natural limestone typical of the Isle of Portland. Even if the processing and manufacturing techniques were still to develop, this gave a strong impulse to the use of concrete, so that the use of portland mortars spread throughout Europe and North America. Soon followed advances in both the necessary equipment (with the introduction of rotary kilns by the first cement companies) and testing practices (tensile strength was tested by building a cantilever beam made of bricks held together by the mortar). It was not before the 20^{th} century that standards and Codes started to come out.

Even if the very first examples of Reinforced Concrete (RC) date back to the second half of 19^{th} century, its widespread use came much later, during the first half of 20^{th} century. The new technology determined the final boost

to the concrete technology, becoming the most used construction material worldwide.

2.2 Constituents

Portland cement concrete is composed of an organic mortar, aggregate particles, water and chemical admixtures. In order to obtain high-quality, resistant concrete proper measures must be taken in the manufacturing process. This procedure goes under the name of *Mix Design* (see Section2.4) and it is necessary to select the suitable components and to determine their relative quantities in order to obtain, as economically as possible, concrete of the appropriate mechanical properties.

Since the particle model proposed in this work focuses its attention on the aggregate pieces interacting through the cement paste, great attention will be devoted to these two constituents in the treatment. The microscopic and macroscopic chemical structure and mechanical behavior of hardened concrete will presented, highlighting the main features influencing the modeling technique presented.

2.2.1 Portland Cement

As already described in the previous paragraphs, there exists a wide variety of different cements which can greatly differ from the chemical point of view, but the great majority of concrete used today is made with portland cements. The name *portland* itself does not give information on the actual composition of the cement, since it applies to a whole family of cements that share similar properties and composition. To this end, different cements can be designed for different purposes and still go under the name of *portland cement*.

Manufacturing and Chemical Composition

In terms of principle, manufacturing portland cement is easy. A limestone and clay mixture is heated to $1400°C - 1600°C$, in order for the two materials to chemically interact forming calcium silicates. Limestone (or calcium carbonate) is the most common source of calcium oxide, but also chalk, shell deposits or calcareous muds can be used. In practice, seen the large amounts of materials to be processed, the actual location of the processing plant is generally determined by the availability of good quality limestone. In fact, the iron-bearing aluminosilicates (in the form of clays or silts) are invariably used as the main source of silica, and they can usually be obtained in good quantity withing close proximity.

After the two main constituents have been stored, manufacturers must ensure that the raw materials entering the kilns is of constant composition and in a ground, blended state. Depending on the mixing procedure and the amount of water used, one can distinguish between *dry*, *semi-wet* and *wet* processes. In any case, a properly blended and pulverized feed is obtained and made ready to enter the kiln. The heat treatment is called *clinkering*, to distinguish it from sintering (in which no melting occurs) and fusion (in which materials are completely melt). The *clinkering* partially melts the constituents, leaving approximately one-fourth of the mixture in liquid state in order to obtain the desired chemical reactions. For this reason the material obtained from the process is called *clinker*, and after the cooldown process it is one again grounded to the final powder state. Also, a small amount of gypsum is inter-ground with the clinker in order to control the early chemical reactions. The ground clinker together with gypsum forms the portland cement.

Table 2.1 shows the main chemical constituents of a typical portland cement. The total sum of the weight does not add up to 100% because impurities are taken into account. Shorthand notation is derived from an oxide notation generally used in ceramic chemistry. The calculation of the

Table 2.1: Typical composition of Portland cement

Chemical Name	Chemical Formula	Shorthand Notation	Weight Percent
Tricalcium Silicate	$3CaO \cdot SiO_2$	C_3S	55
Dicalcium Silicate	$2CaO \cdot SiO_2$	C_2S	18
Tricalcium Aluminate	$3CaO \cdot Al_2O_3$	C_3A	10
Tetracalcium aluminoferrite	$4CaO \cdot Al_2O_3 \cdot Fe_2O_3$	C_4AF	8
Calcium sulfate dihydrate (gypsum)	$3CaSO_4 \cdot 2H_2O$	$C\overline{S}H_2$	6

different phases percentages is also known as the *Bogue* calculation [24] and is still used by the main Codes worldwide.

Hydration of Portland Cement

Portland cement is a hydraulic mortar, this means that when mixed with water, its constituents undergo different chemical reactions leading to the final hardening. Any reaction in the presence of water is called *hydration* and the results of the process are referred to as *hydration products*. For what concerns cement hydration, it is useful to distinguish between the different feature the single components add to the final hydration product (see Table 2.2).

The hydration reactions happening in concrete all *exothermic*, meaning that heat is always released; thus, during hardening, concrete gets heated from the inside. The extent of temperature rise in a concrete member depends on how quickly the heat is liberated to the external air. This means that the actual rate of heat evolution is an important quantity. The hydration phase is critical and greatly affects the final properties of the material. Curing is the process in which the concrete is protected from loss of moisture and kept within a controlled temperature range. The result of this process is increased strength and decreased permeability. A good curing

Table 2.2: Hydration characteristics of the cement constituents

Compounds	Reaction Rate	Amount of Liberated Heat	*Contribution to Cement* Strength	Heat Liberation
C_3S	Moderate	Moderate	High	High
C_2S	Slow	Low	Initially low, High Later	Low
$C_3A + C\overline{S}H_2$	Fast	Very High	Low	Very High
$C_4AF + C\overline{S}H_2$	Moderate	Moderate	Low	Moderate

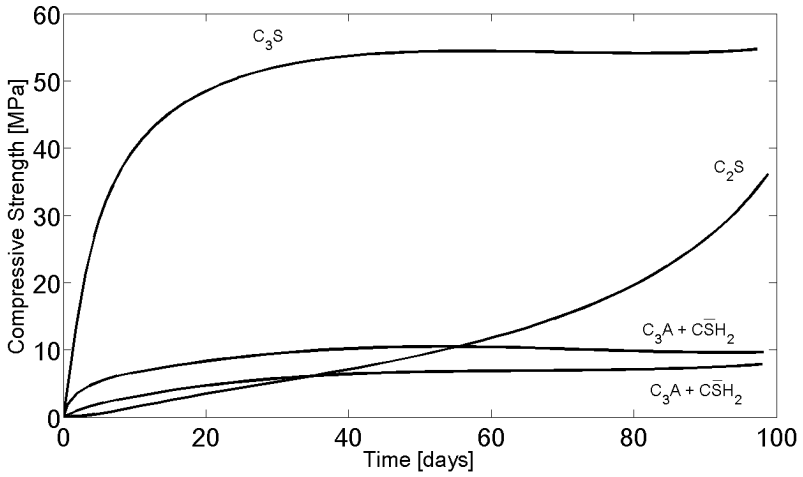

Figure 2.1: Compressive strength contribute of the different constituents

process also mitigates micro-cracks, which severely impacts durability by letting harmful substances penetrate the concrete.

Fig. 2.1 shows the development of compressive strength over time furnished by the different constituents.

Portland Cement Testing

Seen the many factors influencing the manufacturing process, portland cement production requires strict quality control procedures, coded by different National Standards [117] [31] [93]. It is worth noting that it is hard to compare the different kinds of tests described in the different Codes, since

they do not measure fundamental material properties but rather quantities that can be related to those, to choose if the material satisfy the standards.

Provisions on the chemical composition of the cement are generally extremely wide, because it has been demonstrated that different materials with very distant chemical compositions might work just as well. For this reason, physical and mechanical requirements are generally considered more reliable, and give more strict provisions. ASTM 150 [117] requires different sets of tests: fineness, setting time, expansion, strength.

Fineness is an important parameter to evaluate, since it affects the cement in different ways: increasing fineness requires greater amounts of gypsum, and it tends to increase the rate of hydration and water required, while decreasing bleeding and freeze cycles durability. To this end, the two control parameters to assess a cement fineness are the *specific surface* and *particles size distribution*. Specific surface is generally measured through Wagner Turbidimeter, using the Stoke's law to evaluate the particle size and surface area by assuming they are spherically-shaped.

For what concerns the time of setting, two different times are defined: *initial set* up to the point where the paste is no longer moldable, and the *final set* indicating the point at which the paste has hardened enough to sustain some load. The most common method to measure this quantities is by the Vicat needle: a $1\,mm$ large needle is pushed in a mold containing cement paste, the initial set is defined as the time at which the needle reaches a depth of $25\,mm$, whicle the final set occurs when the needle can not sink anymore. The usual values are generally $5\,h$ and $8\,h$ respectively.

Unsoundness may occur in the cement paste if it is subject to excessive volume change after setting. This is generally caused by the slow hydration of the MgO, which can happen months after the concrete is cast. For this reason, accelerated tests are performed in autoclave heating the specimens for $3\,h$ and checking the expansion against a threshold value.

Since cement is primarily used as a structural material, it is very important to evaluate its strength. The most important feature is obviously the

relationship between the cement and concrete strength. This property is extremely hard to define, since there are many factors that can influence the measurements, such as the water/cement and the sand/cement ratio, type and grading of sand, molding and mixing processes, curing conditions, size. To this end it is clear that any strength test must follow the defined procedure very carefully. The most common test is obviously the compressive one, provisions given in ASTM C 109 [118] require to cast $50\,mm$ cubes of mortar by using a $2.75:1$ sand/cement ratio and a water/cement ratio equal to 0.485. As an alternative to this test, it is possible to use the two portions obtained by performing a flexure test, which is getting growing attention and is often used as a measure of the bending tensile strength of the mortar.

2.2.2 Aggregates

Aggregates usually represent the $70 \sim 80\%$ of the total volume of concrete: this means they play an extremely important role in the final properties of the mix. They are generally granular materials derived from natural rock (as natural gravels or crushed stone) and sands, but different synthetic materials have been used with success in particular applications, such as expanded clay or shale in lightweight concrete or waste materials in the so called *recycled* concrete [89]. They are not generally classified based on their mineralogy, since almost every kind of rock is ad-operable in the concrete mix, but rather on the simple and useful distinction on the basis of the specific gravity. Aggregates are divided in: heavy-weight, normal-weight and light-weight. Normal-weight aggregates constitute the 90% of the total, and since this works will focus on the modeling of regular concrete, the attention will be devoted to this class.

Generally it can be said that aggregates should be hard and strong, free of undesirable impurities and chemically stable. The use of porous, soft rocks may induce low strength and wear resistance, together with the possibility of breakage during mixing and reduce the workability of the mixture due to

the increase in the amount of fines. Also, rocks with specific weak directions tend to fracture easily on those planes, limiting the mechanical properties of the concrete.

The main properties to be known are: (1) shape and texture, (2) size gradation, (3) moisture content, (4) specific gravity, (5) bulk unit weight. All these aspects will be discussed in the following Sections.

Shape and Texture

The shape of the aggregates used greatly affect the final quality of the concrete both in terms of workability and mechanical properties. Since a sufficient amount of cement paste is required in order to coat all the aggregate pieces and simultaneously lubricate the mixture to decrease friction among particles during the casting. From the workability standpoint, almost-spherical shaped aggregates with smooth surfaces are to be preferred, since they present the best surface-to-volume ratio; the majority of natural aggregates come close to this ideal. Crushed stones present irregularities and may also have rough surfaces. They also interfere greatly with each other, even when uniform in shape. The higher surface-to-volume ratio also means a greater amount of paste is needed to cover all the aggregate pieces. Highly irregular particles with sharp edges will lead to greater interaction during the mixing process. Very flat and elongated aggregates are generally avoided because of their high surface-to-volume ratio and the tendency of the obtained mixture to segregate during handling; also, the presence of oblong particles in crashed rock may be indicative of the presence of weak fracture planes. A very detailed description of the different classes is given by the British Standards [123] and reported in Table 2.3.

While the shape and texture of the fine aggregate affect workability only, the characteristic of the coarse aggregate play a significant role in the mechanical properties of concrete, since they affect mechanical bond. Their shape can increase strength (especially tensile resistance) by increasing

Table 2.3: Particles shape classification and surface texture of aggregates

Particle Shape Classification		
Classification	*Description*	*Examples*
Rounded	Fully water-worn or completely shaped by attrition	River or seashore gravel; seashore and windblown sand
Irregular	Normally irregular, or partly shaped by attrition and having rounded edges	Other gravels, sand or dug flint
Angular	Possessing well-defined edges formed at the intersection of roughly planar faces	Crushed rocks of all types; talus, crushed slag
Flaky	Particles of which the thickness is small compared to the other two dimensions	Laminated rock
Elongated	Material, usually angular, in which the length is considerably larger than the other dimensions	-
Flaky and Elongated	Material having the length considerably larger than the width, and the width considerably larger than the thickness	-

Surface Texture of Aggregates			
Group	*Surface Texture*	*Characteristics*	*Examples*
1	Glassy	Conchoidal fracture	Black flint, obsidian, vitreous slag
2	Smooth	Water-worn, or smooth due to the fracture of laminated or fine-grained rock	Gravels, chert, slate, marble, some rhyolites
3	Granular	Fracture showing more or less uniform rounded grains	Sandstone, oolite
4	Rough	Rough fracture or fine or medium-grained rock containing no easily visible crystalline constituents	Basalt, felxite, porphyry, limestone
5	Crystalline	Containing easily visible crystalline constituents	Granite, gabbro, gneiss
6	Honeycombed	With visible pores and cavities	Brick, pumice, foamed slag, clinker

the amount of available surface area for bonding with the paste, given a certain aggregate content. It is, though, important not to exaggerate the aggregate content to avoid internal stress concentrations, leading to fragile and low-strength behavior. Generally, rough and textured surfaces improve mechanical bond with the paste, since they can accentuate interlocking and frictional behavior. This can lead to a higher strength concrete that exhibits a more ductile post-peak behavior. Various authors [79] [5] also show how the mineralogical composition of the aggregate may influence the strength of the aggregate-paste bond, based on the idea that the interface zone resistance depends on the chemical interaction between matrix and inclusions.

Size Gradation

The different particle sizes distribution, or *gradation*, is very important in the mix design of a concrete. In fact, it determines the paste requirement for the chosen workability. Since the cement is the most expensive component in concrete, it is highly desirable to minimize its needed quantity while retaining the desired workability, strength and durability in the final product. To this end, considering concrete as a compacted assembly of aggregate pieces kept together by the cement paste, where the matrix itself fills the voids between particles. This means that the required amount of paste greatly depends on the amount of void space to be filled and the total surface area that must be coated by the cement matrix. It is clear that by using a uniform size, it is impossible to cover the given domain, so it is necessary to use different sizes of particles; by doing so the smaller sized aggregate will fill the voids left by the bigger one, see Fig. 2.2

The grading of the aggregate is determined by *sieve analysis*; based on its results the granulometric composition of the aggregate is evaluated. It is convenient to distinguish between *coarse aggregate*, which is everything retained on the $4.75\,mm$ sieve, and the *fine aggregate*, which is obviously

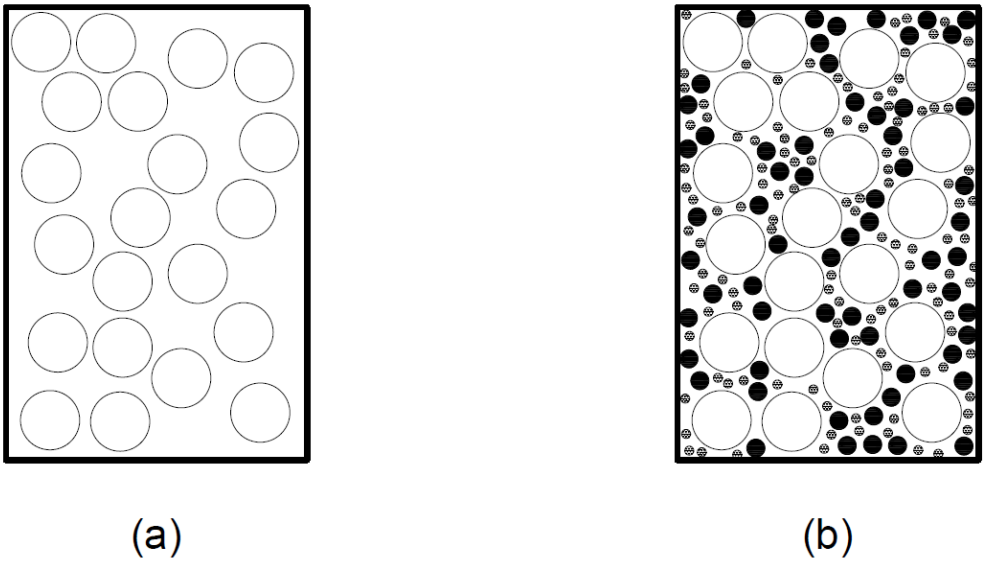

Figure 2.2: Different size gradations: (a) uniform size and (b) graded size

everything else. Even though every National Code gives different provisions about the sieves and distributions to use, this distinction is generally accepted.

The ideal granulometric curve was determined by Fuller and Thompson [54]:

$$P_t = \left(\frac{d}{D}\right)^{1/2} \tag{2.1}$$

where P_t is the passing amount (%) at a given sieve, and D is the maximum particle size. This curve is a special case of a more general equation who was first introduced by Andreasson [7]:

$$P_t = \left(\frac{d}{D}\right)^{q} \tag{2.2}$$

with $0 < q < 1$. It can be shown that, in line of principle, if all the aggregate sizes below D were present in the mix, the unfilled volume would only depend on q, and in particularly decreasing as q decreases. Even if values of $1/3 < q < 1/2$ have been used, in most applications the lowest practical value is $1/2$, leading back to the Fuller curve. The reason is that minimizing void content (in order to get an economic concrete using

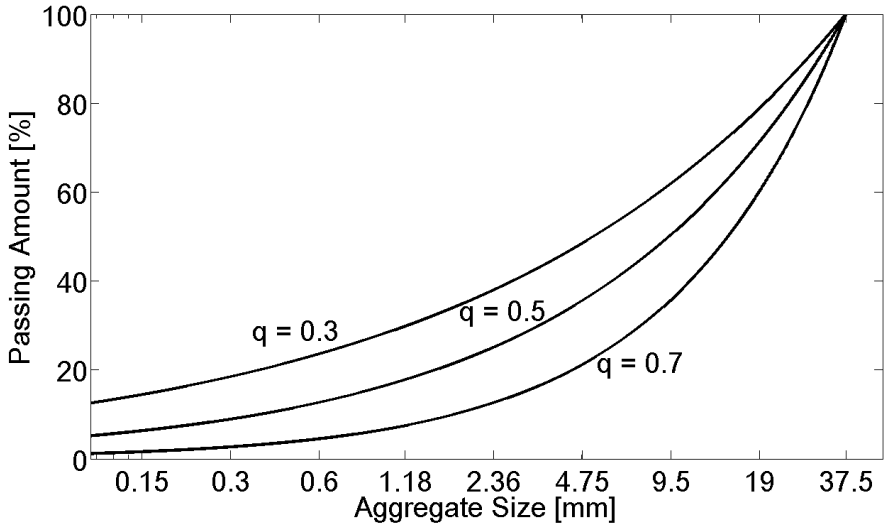

Figure 2.3: Different theoretical Andreasson curve for a given $D_{max} = 37.5\,mm$

minimum amount of cement), results in poor workability.

The results shown in Fig. 2.3 are obtained theoretically, but the actual aggregate used in construction cannot be represented by a smooth function. The actual granulometric distribution, in fact, is necessarily discrete, because the passing amount are measured at certain points of the curve (i.e. the different sieves dimensions). To this end, Shilstone [114] developed an empirical procedure that allows to optimize the concrete workability, strength and economy by combining different aggregate gradation.

Fig. 2.4 shows the combining of the different granulometric phases. The authors distinguish between three different classes: (1) Quality aggregate Q, with size greater or equal than 9.5 mm, (2) Intermediate particles I, with size between 2.36 and 9.5 mm, (3) Workability aggregate W, with size smaller than 2.36 mm. The optimum gradation can be evaluated by means of a relationship between the *workability factor*:

$$P_{2.36\,mm} = \frac{W}{(Q + I + W)} \tag{2.3}$$

and a *coarseness factor*:

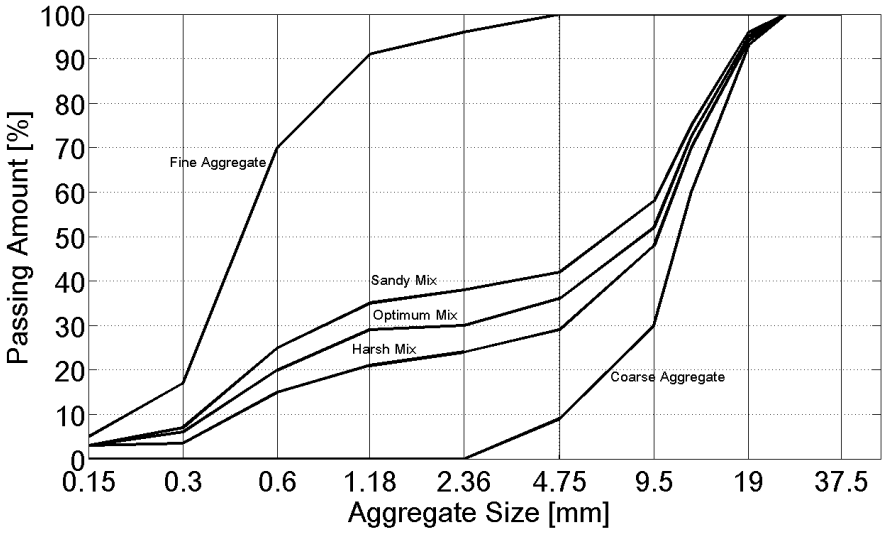

Figure 2.4: Combined aggregate gradations

$$\frac{P_{9.5\,mm}}{P_{2.36\,mm}} = \frac{Q}{(Q+I)} \tag{2.4}$$

Not only the aggregate size gradation influences the final concrete, but also maximum size plays an important role, since it influences the required paste amount and the mechanical properties of the mix. ASTM 125 [9] suggests that the maximum size of the aggregate is the smallest sieve opening through which the entire sample passes. In the practice, though, a small amount of retained aggregate will not affect the properties of concrete; for this reason it is usual to use a *nominal* maximum aggregate size, meaning that a certain percentage of the total aggregate is still permitted to be bigger than the threshold value.

The choice of the maximum nominal size is important, because if the particles are too large the final material at some points (i.e. cross sections, joints) may not be representative of the mix because of the presence of a big aggregate piece. It is a common rule not to use aggregate diameter greater than one-fifth of the smallest dimension of any form used to cast the concrete (i.e. the smallest dimension of the structure to be cast). Also, large particles may be obstructed be narrow bars spacing causing segregation during the

casting process. To avoid this, the nominal maximum size should be lower than three-fourths of the minimum clear spacing between reinforcing bars.

The higher the maximum size, the lower will be the required paste content. For a set workability and cement content, the final strength tends to increase, since it is possible to lower the w/c ratio. But it must be also kept in mind that the larger particles will induce higher internal stresses that may lower the concrete strength. This effect is particularly evident in high-performance concrete [4], for which the maximum aggregate size is usually lower than $10\,mm$. For what concerns durability, an increase in the maximum aggregate size generally improves performances because of the diminution of the amount of paste potentially prone to chemical-physical attacks. However, in cold environments it is always suggested to use smaller sizes because of the tendency of the aggregate to suffer freeze-that damage.

Moisture Content

Every aggregate piece presents porosity on the surface, making it capable of absorbing water into its body, or retain it on the surface as a moisture film. For this reason, stockpiled aggregates present different moisture contents. Knowing this quantity is crucial because if the aggregates have the tendency of absorbing water, this will be removed from the mix, lowering the effective w/c ratio, and with it the workability. On the contrary, if water is present in the aggregates, the effective w/c will be higher than desired.

It is possible to define four moisture states: (1) Oven-dry (OD) aggregates present no water after being heated in oven at $105°C$; (2) Air-dry (AD) aggregates present no water on the surface, but the internal pores are partially full; (3) Saturated-surface-dry (SSD) particles have filled pores but no water film on their surface; (4) Wet (W) aggregates are completely saturated with a film on the surface.

To calculate the amount of water that the aggregates will be exchanging with the paste, one can define the following three quantities. Absorption

capacity

$$A = \frac{W_{SSD} - W_{OD}}{W_{OD}} \cdot 100 \tag{2.5}$$

where W_{SSD} and W_{OD} represent the weight of the aggregate sample in SSD and OD state, respectively. The value of A represents the maximum amount of water the aggregate can absorb, and its usual values range from 1% to 2%.

The effective absorption

$$EA = \frac{W_{SSD} - W_{AD}}{W_{SSD}} \cdot 100 \tag{2.6}$$

This value represents the quantity of water needed to bring the aggregate from AD to SSD state. The weight of water absorbed to bring AD aggregate to SSD state can be expressed as:

$$W_{abs} = \frac{EA\, W_{agg}}{100} \tag{2.7}$$

where W_{agg} is the weight of SSD aggregate in the mix. The surface moisture

$$SM = \frac{W_{wet} - W_{SSD}}{W_{SSD}} \cdot 100 \tag{2.8}$$

represents the water in excess of the SSD state and it is used to calculate the amount of additional water added to the concrete with the aggregate:

$$W_{add} = \frac{SM\, W_{agg}}{100} \tag{2.9}$$

To generalize the previous expression one can define the moisture content

$$MC = \frac{W_{stock} - W_{SSD}}{W_{SSD}} \cdot 100 \tag{2.10}$$

where W_{stock} is the weight of the stocked aggregate. If the MC value is positive, it is surface moisture, otherwise effective absorption. Thus:

$$W_{MC} = \frac{MC\, W_{agg}}{100} \tag{2.11}$$

where W_{MC} is the total moisture of the aggregate, being positive if the moisture is added and negative if it is absorded.

Specific Gravity

Density of the aggregate is an important parameter in the mix design to evaluate weight-volume ratio. The specific gravity

$$SG = \frac{\rho_s}{\rho_w} \tag{2.12}$$

where ρ_s and ρ_w are the density of solid and water respectively, whiled ensities are determined by displacement in water techniques.

Taking pores into account, one can distinguish between the Apparent Specific Gravity (ASG), which only refers to the effective solid material excluding the pores, or the Bulk Specific Gravity (BSG), taking into account the pores in the total volume.

$$ASG = \frac{W_{solid}}{V_{solid}} \cdot \frac{1}{\rho_{water}} \tag{2.13}$$

$$\begin{aligned} BSG &= \frac{W_{solid+pores}}{V_{solid+pores}} \cdot \frac{1}{\rho_{water}} \\ &= \frac{W_{solid+pores}}{W_{displaced\,water}} \end{aligned} \tag{2.14}$$

It is clear that the BSG value is more realistic since it takes into account the effective volume that the aggregates occupy. The contribution of the pores to its value depends on the pore contribution medium to the aggregate weight; if the pores are saturated there is a contribution, which is absent in the case of dry pores. It follows that

$$ASG > BSG_{SSD} > BSG_{OD} \tag{2.15}$$

However, since the porosity of the rock used in concrete rarely exceeds 2%, the three values are generally extremely close to each other.

Bulk Unit Weight

Unit Weight (UW) is the ratio between the weight of the aggregate and the occupied volume. By means of its value it is possible to measure the volume that the graded aggregate will occupy. As suggested by ASTM C 29 [10], the unit weight can be measure by simply filling a container of a given volume with aggregate and weighting it. Since this operation is greatly influenced by the compaction grade, the same Standard suggests to use rodding. Also, the total weight will depend on the moisture content, so oven-dry aggregate should be used.

That space occupied by voids will be filled by the mortar in the concrete mix, this quantity can be evaluate by using the unit weight. For every m^3 of concrete:

$$V_{tot} = V_a + V_v = 1\,m^3 \tag{2.16}$$

so

$$V_v = (1 - V_a)m^3 \tag{2.17}$$

where V_a and V_v are the volume of aggregate and voids respectively. Since

$$V_a = \frac{W_a}{BSG \cdot \rho_w} m^3 \tag{2.18}$$

it follows

$$V_v = 1 - \frac{W_a}{BSG \cdot \rho_w} m^3 \tag{2.19}$$

or

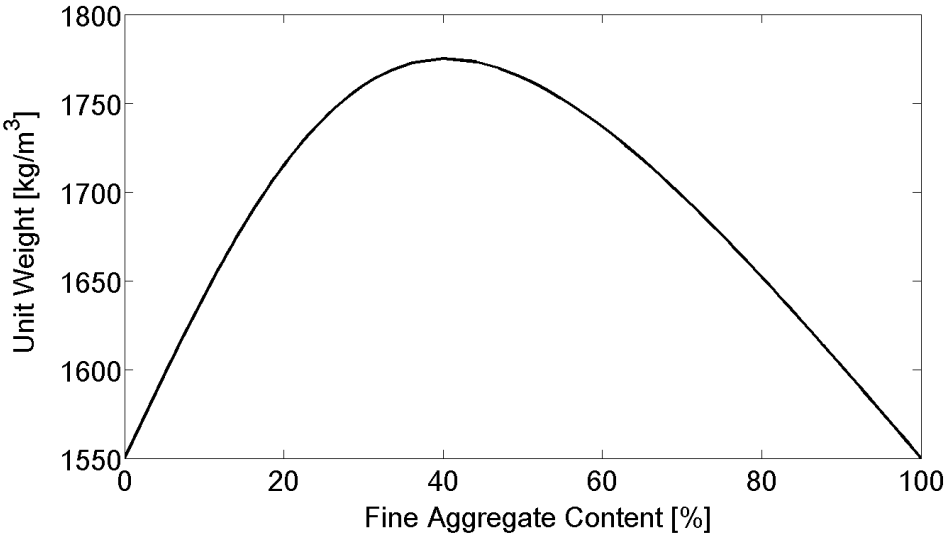

Figure 2.5: Unit weight variation for different values of fine aggregate content

$$V_v[\%] = \frac{BSG \cdot \rho_w - UW}{BSG \cdot \rho_w} \cdot 100 \tag{2.20}$$

The usual value of the UW for normal-weight aggregates are usually in the range $1450 - 1750\, kg/m^3$. It has already been discussed how aggregate containing smaller fractions are more suitable to fill the entire domain, so it easy to understand how the granulometric composition will also affect the value of the bulk weight. Fig. 2.5 displays the variation of the calculate UW for different percentages of fine aggregate.

2.2.3 Water

Since water is a key constituent of the concrete, and its quality may greatly influence the final properties of the composite, it has to be regarded as a constituent material. Understanding its properties helps understanding its effects on the final product: even if it is part of the Water chemical composition, and in particular the hydrogen bonds, are the reason for its high heat of fusion and vaporization, as well as specific heat.

2.2.4 Admixtures

The definition of an admixture is given in ASTM C 125 [9] as a "material other than water, aggregates, hydraulic cement and fiber reinforcement that is used as an ingredient of concrete or mortar and is added to the batch immediately before or during its mixing".

Different admixtures are nowadays regularly used in the concrete technology [90]. The use of this materials generally provides some particular characteristics to the behavior of either fresh or hardened concrete. Based on their origin, admixtures can be divided in: *Mineral Admixtures* (MA) and *Chemical Admixtures* (CM).

Mineral Admixtures

Mineral admixtures are ground solid materials added to concrete. This practice is well-established in the modern concrete technology, and it is used to obtain concrete with particular characteristics, such as improved workability or durability. MA can be divided into three main categories:

1. Pozzolanic materials
2. Cementitious materials
3. Non-reactive materials

The so called *blended cements*, extremely common in Europe, are obtained by adding a material from the first two categories to the cement. The results is that the admixture chemically interacts with the hydrating portland cement, leading to a modified concrete microstructure. The use of these materials improves the concrete performance in many ways (e.g. improving durability), but many companies use fly ash just because it is cheaper than cement, on an economical base. Anyways, mineral admixtures are environmentally friendly not only because their usage involves the recycling of waste products, but also because the energy consumption and the CO_2 emissions from their production is lower than the one of the regular concrete.

For what concerns the non-reactive materials, they are generally finely divided materials, such as limestone, hydrated lime, silica flour. They are mixed to portland cement to obtain improved-workability masonry cement or water-retaining materials. Since the workability improvement is their main usage, they are also referred to as *workability aids*. Even if they are classified as non-reactive, some minor chemical interaction may still occur under particular conditions.

Chemical Admixtures

By chemical admixtures, one usually refers to water-soluble additives that are poured during the mixing process. Even though there exist many different chemical admixtures at present, they all fall into the following three categories:

1. *Air-entraining*, used to improve the concrete freezing and thawing resistance.
2. *Set-controlling*, used to control the setting or to induce early hardening.
3. *Plasticizers*, used to enhance the mix workability.

The enormous number of different chemicals that can be used in concrete manufacturing is due to the many desirable characteristic that designers want to confer to the final product, seen the many different applications concrete has nowadays. Table 2.4 shows the different effects of the most commonly used chemical admixtures on the concrete.

2.3 Hardening and Microscopical Composition

The behavior of the hardened cement paste is crucial for the definition of the global response of the concrete.To this end, it is clear that one must understand how the different hydration products fit together to form the cementing matrix. As the hydration proceeds, the water dividing different

Table 2.4: Effects of chemical admixtures on concrete properties

Property	*Admixture Type*
Workability	Water-Reducing Admixtures
	Plasticizers
	Air-entraining admixtures
	Pumping aids
	Anti-washout admixtures
Set Control	Set-accelerating admixtures
	Set-retarding admixtures
	Extended-set admixtures
Strength	Water-reducing admixtures
Durability	Air-entraining admixtures
	Water-reducing admixtures
	Corrosion inhibitors

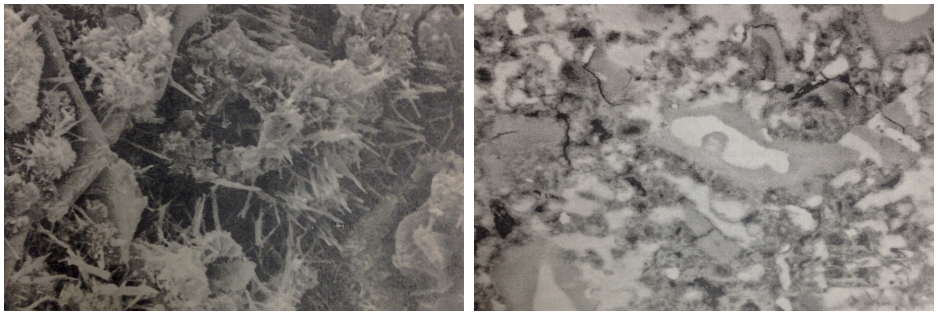

Figure 2.6: Microstructure of fresh (left) and 28-day-old (right) concrete

cement grains is replaced by solid products to form a continuous matrix and bind the other grains together.

The mechanical properties of hardened concrete are influenced by the internal structural and the chemical bonds between molecules. Like every composite material, the interaction between the different phases (i.e. mortar and aggregates) plays a fundamental role and so it is worth of deep investigations. The chemical reactions happening in the cement paste during its hydration process form new molecules, and they are responsible of the formation of a zone of at the next to the particles surface.

Each of the four main cement minerals (C_3S,C_2S,C_3A,C_4AF, see Ta-

ble 2.1) reacts at a different rate and tends to form different solid phases during the hydration process. It should be noted that during the actual cement hydration process all the minerals dissolve into the same pore solution, and thus the solid hydration products are associated with the pore solution as a whole rather than a particular cement mineral. However, the individual reactions provide a good approximation of the overall hydration behavior of cement.

Fig. 2.6 shows the different micro-structural composition of a very young concrete (left) and a polished section of a fully hydrated sample (right). While in the first ettringite ($C_6AS_3H_{32}$, a mineral forming from the reaction of C_3A and gypsum) needles are growing into pores submerged by water, in the second hydrated cores surrounding larger grains are evident. The presence of aggregates greatly affects the hydration process, so that the final micro-structure of concrete is extremely different from the paste. In particular, in the proximity of an aggregate piece, the hydration processes are highly modified. This portion of the volume goes under the name of *Interface Transition Zone* (ITZ) and it can generally be identified by the concentration of oriented calcium hydroxide crystals. The ITZ shows characteristics that may greatly differ from the structure of the material, in particular the greater porosity and reduction of unreacted cement close to the aggregate surface. The main reason for these differences lies in the so called *wall effect*, consisting in the inability of the cement grains to efficiently coat the inclusions, leading to a local raise of the w/c ratio (which can be further increased by bleeding effects). Fig. 2.7 shows two profiles of the ITZ compositions from which it is deduced that this zone extends for $\approx 30 - 40\mu m$.

The effective structure of the ITZ can be complex and variable, since it may show different thickness values or be absent at some parts of the surface. For this reason, it can be regarded as a statistical quantity, depending on the aggregate size and shape, w/c ratio, mix procedures. Within the free space close to the aggregate particle, calcium hydroxide crystals and ettringite can

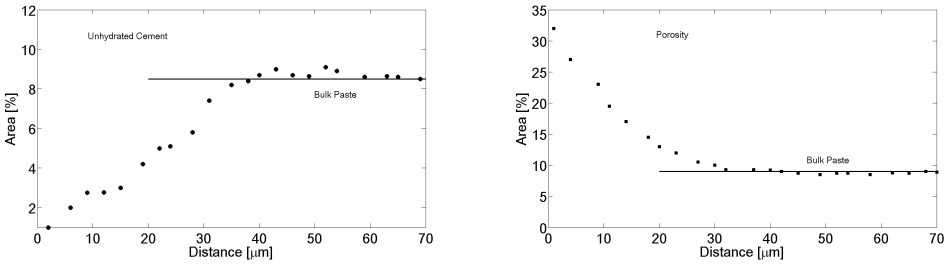

Figure 2.7: Volume fraction and porosity variation with respect to the distance to aggregate pieces

easily form, even though calcium components generally prevail because of their capability to form larger crystals.

It is recognized that the ITZ has a great influence on the properties of concrete [94] [110]. For example, the interfacial porosity is interconnected, strongly influencing the concrete permeability. Moreover it is established [4] that in order to obtain high-performance concrete (especially in tension) it is necessary to reduce the ITZ thickness as much as possible, since it limits the strength of the matrix-aggregate bond.

The hydration process (and particularly its rate) has a strong influence on the workability of concrete. When cast, the material lies in a semi-fluid state and then it hardens due to hydration. Different kinds of usage of concrete require different consistencies of the material: the measure of the consistency of fresh concrete is called *slump*, and it takes its name from the test used to evaluate such property.

2.4 Technology & Mix Design

Knowing all the different properties that each constituent furnishes to the final mix and their macro and microscopic arrangement in the hardened concrete, helps understanding the better practices to use in order to obtain the desired strength, workability and durability, while keeping costs reasonable. The procedure is called *mix design* and it is used to evaluate the most appropriate materials to use (cement, aggregate, water, admixtures) and

to proportion them. Even if many theoretical studies are available nowadays [42] [33], mix design is still an empirical procedure. This explains why, even if there are many properties that could in principle be governed during the mix design, the general procedure aims to achieve a certain compressive strength at some given workability and age.

Design-wide, compressive strength is probably the most important property in the hardened concrete, since it is directly used in the structural design and also because other mechanical properties (e.g. the tensile stress) can be evaluated from empirical regressions laws. According to Abrams [2] the water to cement ratio is the only parameter that affects the strength of concrete:

$$\sigma_c = \frac{A}{C^{3/2(w/c)}} \tag{2.21}$$

in which σ_c is the compressive strength, A is a constant usually taken to be equal to $96.5\,MPa$ and B depends on the cement used (≈ 4). Even if different equations were proposed in literature [102], the main idea remains that the compressive strength is inversely proportional to the w/c ratio. This is mainly due to the fact that the ratio determines the porosity of the paste [101], and so it greatly affects durability as well.

2.4.1 Mix Design Procedure

There exist many different methods of mix design. Even if they are not directly comparable to each other, they do give approximately the same proportions between constituents. The most common method used in the North America is given in ACI Standard Practice 211.1 [116], while in Europe the UNI EN 206-1 [34] gives provisions on the required criteria both the fresh and hardened concrete must satisfy.

The mix design procedure can be summarized as follows:

1. *Information Gathering*: prior to the design, it is important to gather all the information about the raw materials available and the structure

to be built.

2. *Slump*: workability of fresh concrete is generally specified for the job, in the case it is not, it should be selected as the lowest value to guarantee a correct placement.

3. *Maximum Aggregate Size*: based on the dimensions of the elements to be cast, the maximum aggregate diameter is chosen as an opportune fraction of the smallest dimension of the element or the minimum bar spacing.

4. *Mixing Water and Air Content*: the water to be used, together with the entrapped air (per m^3 of material) are estimated. In the case plasticizing admixtures are used, it is necessary to reduce the amount of water by the estimated amount.

5. *Water/Cement Ratio*: based on the estimate of the mixing water and the required compressive strength, the w/c ratio can be evaluated, so that the total amount of cement per m^3 is known.

6. *Aggregate Gradation*: since the volume of all the components is known at this point, the total volume of aggregates is calculated, and based on the maximum size chosen, the full gradation curve can be obtained by means of Eq. 2.2.

7. *Moisture Adjustment*: the designer must ensure the water absorbed or added to the mixture by the aggregate. After evaluating the moisture content by means of Eq. 2.11, it is possible to adjust the water content in order to leave the effective proportions unchanged.

2.5 Mechanical Behavior

The highly heterogeneous structure of concrete results in a complex mechanical behavior, since the global response depends on the interaction

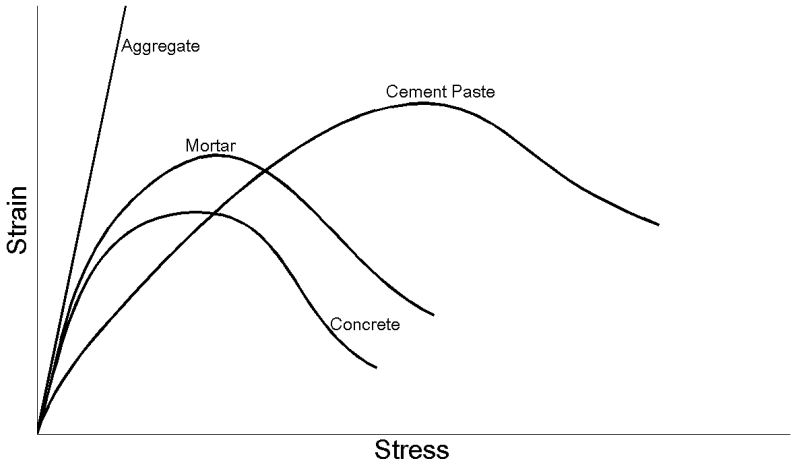

Figure 2.8: Stress-strain response in compression for aggregate, cement paste, mortar, concrete

among them. Any multiphase material, in fact, shows different properties from the constituents. This effect is explained in Fig. 2.8, in which the stress-strain response of the different constituents is shown separately.

According to Zaitsev and Wittman [135] and Cusatis et al. [57], there exist six different observation scales in the internal structure of concrete: (1) macroscale, (2) mesoscale, (3) miniscale, (4) microscale, (5) nanoscale, (6) atomistic scale.

At the macroscopic level, concrete can be seen as homogeneous material which shows extremely different behavior in tension and compression; at the mesoscale level it is composed of coarse aggregate embedded in a mortar of cement paste and finer aggregate; the miniscale in which there is mortar (consisting of fine aggregate embedded in the cement matrix) and the distinction between bulk paste and Interface Transition Zone is expressely taken into account; at the microscale the hydrated cement paste is composed of amorphous $C-S-H$ and calcium hydroxide, containing an extensive network of dry or saturated capillary pores, plus grains of unhydrated cement and grains of calcium sulfoaluminate (also, at this scale, even the aggregate pieces are heterogeneous composites of different minerals); at the nanoscale

the main constituent is the hardened cement portland cement gel containing nano-pores filled partly or fully by water; atomistic scale is characterized by the structure of micro-crystalline particles of hydrated portland cement.

The choice of the observation scale is extremely important because the smaller it is chosen, the more detailed the model will be, with growing computational cost and mechanical description effort. The homogeneous continuum approach is currently the most widely used one, while the present work will focus on the definition of a mesoscale lattice model approach.

2.5.1 Stiffness

Concrete is a nonlinear material in both tension and compression, with nonlinearities arising even before the peak stress. This means that the Young's modulus definition requires some further considerations, since it can only be defined as a measure of the stiffness of the material at a chosen point of the stress-strain history. To these means, the closest approximation to a modulus of elasticity derived from a truly elastic response is the *initial tangent modulus*. This value is only applicable for small stresses and strains, so its use is impractical for design purposes. A more commonly used measure of the stiffness of concrete is the *secant modulus*, evaluated as the ratio between stress and strain at a particular point on the curve.

The initial and secant moduli are not always easy to determine, due to the measurement errors typical of the first part of the tests or preexisting cracks that close under a certain load. For this reason, the *chord modulus* [119] is usually used: the first point of the chord corresponds at a strain of 0.00005, at which the initial tangent modulus is also evaluated. So, at any point of the stress-strain curve the chord modulus can be evaluated by tracing a line for the point corresponding to strain equal to 0.00005, while the secant is obtained by simply evaluating the ratio between stress and strain. In general, the two values are very close in the zone around 40% of the compressive strength of the material. The chord modulus is more conservative and easier

to evaluate experimentally, but it underestimates the strain for stresses greater than 40% of the compressive strength.

Since the stiffness of the concrete depends on the stiffness of its constituents, describing it as a combination of the phases elastic moduli helps understanding the response of the material. For this reason, composite models are usually used to the determine the relevance of each component in the overall behavior. This approach models the concrete as a bi-phase material composed of bulk paste and aggregate, or a tri-phase material by also taking into account ITZ.

To fully describe the response of a system with a dispersed phase embedded in a matrix, it would be necessary to know in advance the geometry of the inclusion (i.e. size, shape, orientation). Since this is impossible for the case of concrete, different equivalent models have been proposed (see Fig. 2.9).

Therefore it is convenient to consider the two extreme cases of Parallel and Series models. The first represents the upper-bound solution for the stiffness, while the latter represents the lower-bound. Neither model is correct, though, since the two components (matrix and aggregate) are not subject to uniform strain nor uniform stress. A refined model was given by Hirsch [72], which combines the two previous models to estimate the elastic stiffness value. Both the Series and the Hirsch models suffer the shortcoming of predicting a null value of the modulus if a null modulus is chosen for any of the constituents. Therefore, another model was proposed by Cunto [35]. The description of the different methods is given in Table 2.5, while the graphical interpretation is given in Fig. 2.10.

Such difference in the stiffness of the main constituents (i.e. aggregate and mortar) creates many bond cracks at the Interfacial Transition Zone even before external loads are applied. During the hydration processes, in fact, the difference in elastic moduli creates stress concentrations under the differential volume changes induced by the chemical reactions. Since the strength of the ITZ is lower than the strength of the other constituents,

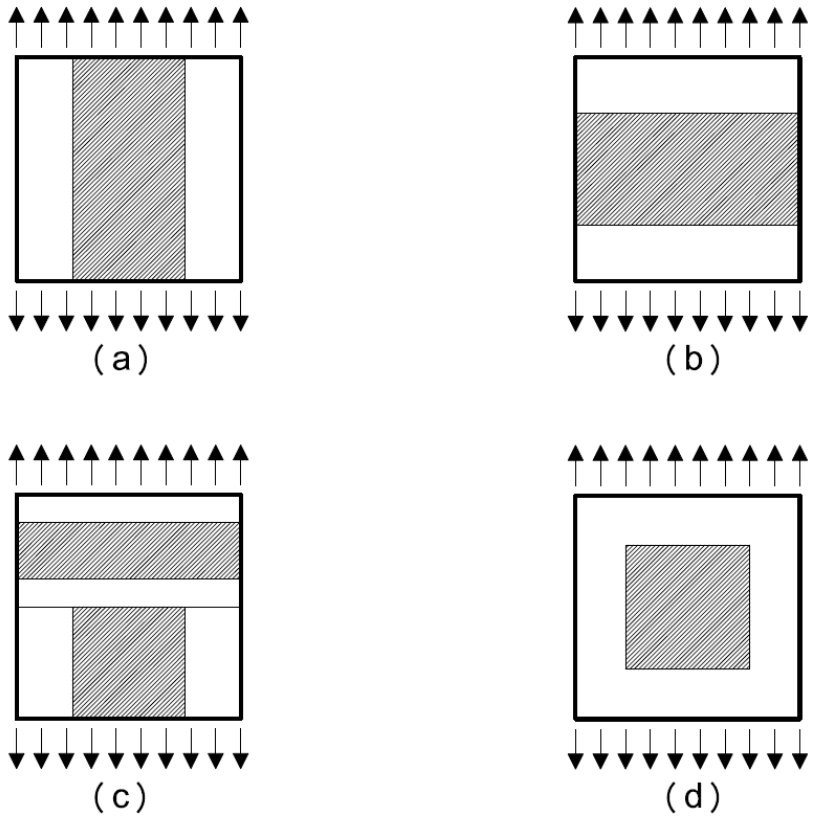

Figure 2.9: Different models for the evaluation of the modulus of elasticity of concrete: (a) Voigt's (Parallel) model; (b) Reuss' (Series) model; (c) Hirsch's model; (d) Counto's model

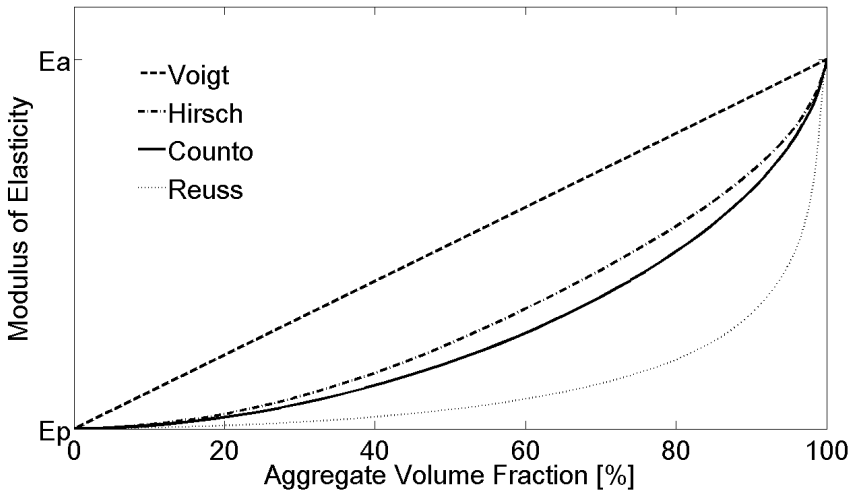

Figure 2.10: Relations between the modulus of elasticity of concrete and the aggregate volume fraction

Table 2.5: Elastic Modulus Evaluation for a Two-Phase Composite

Parallel (Voigt) Model
$E_c = V_p E_p + V_a E_a$
Series (Reuss) Model
$\frac{1}{E_c} = \frac{V_p}{E_p} + \frac{V_a}{E_a}$
Hirsch Model
$\frac{1}{E_c} = x\frac{1}{(V_p E_p + V_a E_a)} + (1-x)(\frac{V_p}{E_p} + \frac{V_a}{E_a})$
Counto Model
$\frac{1}{E_c} = \frac{1-\sqrt{V_a}}{E_p} + \frac{\sqrt{V_a}}{(1-sqrtV_a)E_p + \sqrt{V_a}E_a}$

cracks will form in this region.

The so obtained values only serve to estimate the behavior of the material, while in the practice empirical laws based on very big databases regression are used. ACI Building Code [28] gives the following:

$$E_c = 4730\sqrt{f'_c} \quad GPa \tag{2.22}$$

where where E_c is the secant modulus at 45% of the compressive strength of the material f'_c, evaluated from a standard $150X300$mm cylinder test. Eurocode 2 [45] gives the following formula:

$$E_{cm} = 22(f_{cm}/10)^{0.3} \tag{2.23}$$

where E_{cm} is the secant modulus and f_{cm} the mean cylindrical compressive strength (in MPa).

These empirical rules demonstrate that the modulus of elasticity is mainly related to the compressive strength, so that factors influencing strength will have a strong influence on the stiffness of the material. The dominant factor

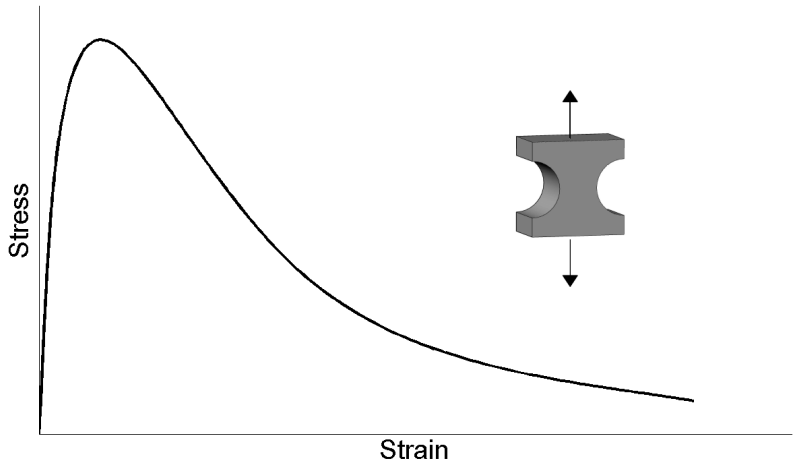

Figure 2.11: Typical stress-strain curve obtained from tensile tests performed on dog-bone specimens

is the porosity, which depends on the w/c ratio, meaning that the modulus will decrease as w/c increases. It is also important to notice that by changing the w/c ratio only the paste is affected, so that the change in stiffness is mainly related to change in the matrix.

2.5.2 Tension

The tensile strength of concrete is much lower than the compression strength, and it also represents the main weakness in the material. Cracks, in fact, can easily propagate under tensile loads. Tensile strength can be evaluated directly by means of dog-bone shaped specimens, or indirectly by the so called splitting (or Brazilian) test.

The typical response is shown in Fig. 2.11. The tensile strength of the concrete is usually 10 times lower than the compressive one. A linear behavior takes place up to $\approx 60\%$ of the strength. The micro-cracks are approximately orthogonal to the applied load and they merge into macro-cracks close to the peak of the curve. A sharp *strain softening* branch is then triggered, with the stress decreasing as the strain is increased during the test. The material undergoes dilatancy only.

2.5.3 Compression

Since the compressive strength is much greater than the tensile one, it is considered the most important property of concrete. The typical uniaxial compression response of concrete is shown in Fig. 2.12. The material is elastic up to $\approx 30\%$ of the compressive strength, then the preexisting bond cracks (see Sec. 2.5.1) start increasing, leading to a nonlinear response. At $\approx 70\%$ of the compressive strength cracks begin to propagate through the mortar, bridging bond cracks. In the post-peak part of the curve cracks start to be visible to unaided eye. Such diffuse cracking is also responsible of the volumetric response reported in Fig. 2.12. The Poisson's ration remains constant $\approx 0.18 - 0.22$ and the volume decreases linearly (Point P of the curve). When bigger macrocracks start to propagate (Point M), the apparent volume starts increasing, due to separation in the internal structure of the material, so that negative values are reached. This phenomenon is known as *dilatancy*.

During compressive load histories, localized stress and strain fields can be evaluated by means of photoelastic coatings. Due to the differences in mechanical properties between the constituents, stress concentrations can may be more than twice as high as the average stress. This aspect must be taken into account in mesoscale analyses, in which the interaction between aggregate and mortar is explicitly taken into account, and will be discussed in Sec. 3.3.2.

2.5.4 Biaxial and Triaxial Behavior

Concrete behavior under multiaxial stress states has been experimentally studied by many different authors. The classic study from Kupfer et al. [82] is certainly one of the best available, and its results are shown in Fig. 2.13. Biaxial tension, tension-compression, and biaxial compression stress states have been applied to concrete prisms in order to evaluate their response. As shown in the picture, biaxial compression results in an increase of the peak

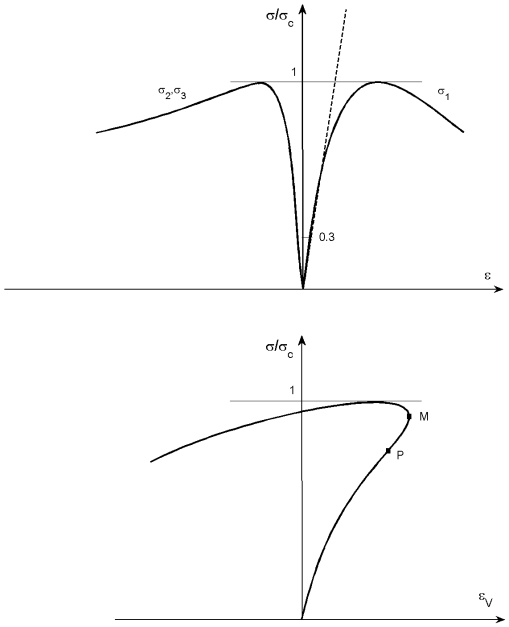

Figure 2.12: Typical stress-strain curve and volumetric response under uniaxial compression

stress, and the highest increase is obtained for a σ_1/σ_2 ratio equal to 0.52. Tension-compression states, peak stress and strain decrease as the ratio of the tensile stress to compressive stress increases. Under biaxial tension the tensile strength and corresponding strain are unaffected by the biaxial stress state.

While Kupfer et al. [82] investigated the biaxial behavior of concrete on prismatic specimen, it is rather common to have triaxial compressive tests on cylinder, due to the relative easiness in applying a radial, constant confining pressure. The typical result is shown in Fig. 2.14.

2.5.5 Cyclic Behavior

The cyclic behavior of concrete has been studied by many authors. This type of response is extremely important when modeling the seismic behavior of concrete structures, since the structure will undergo several cycles and the area under those cycles represents the total amount of dissipated energy.

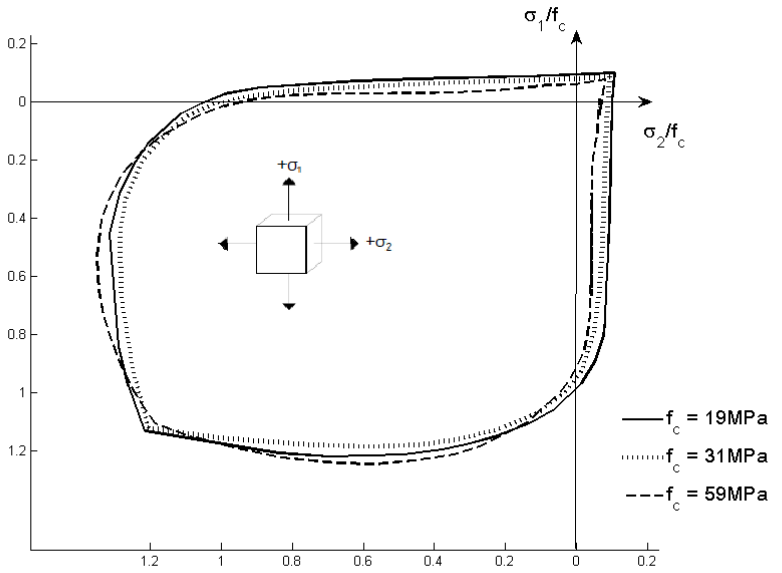

Figure 2.13: Biaxial stress interaction diagram for concrete. From Kupfer et al. [82]

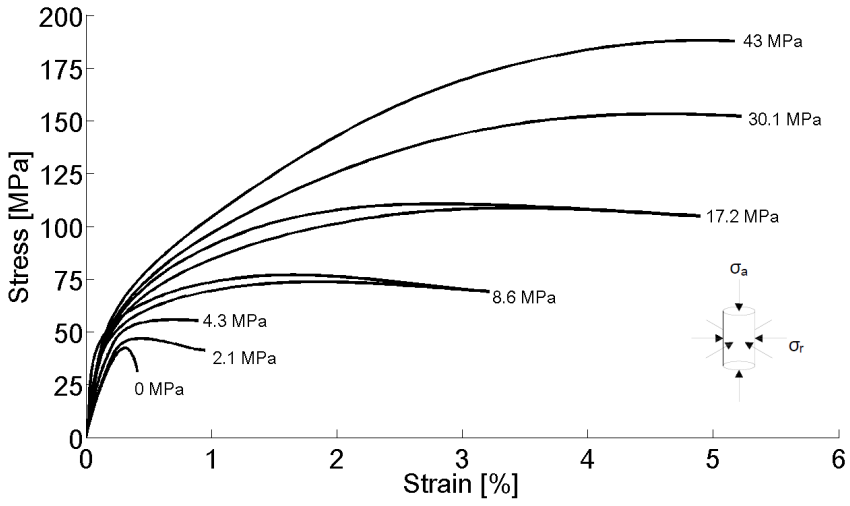

Figure 2.14: Stress-strain curves for different values of the confining pressure

Fig. 2.15 shows the cyclic response of concrete to compressive, tensile and bending actions. It is generally accepted that the cyclic behavior of concrete is that of an envelope curve, which provides a bound between the upper and lower limit for the stress-strain curve [11]. The envelope curve follows the monotonic response of the material.

The reported figures show the existence of residual (plastic) strains, which are inversely proportional to the slope of the unloading-reloading branch.

Such behavior is due to the presence of micro and macroscopical cracks propagating in the medium. When reloading occurs such cracks represent weak points in the material, leading to stiffness degradation. To this end, it must be noted that such damage is irreversible and cracks can only be closed by compressive forces acting orthogonally to them. This means that damage is concrete is *history dependent*, meaning that the strain history in every point of the material influences its response to external loads. This aspect will be discussed in Sec. 3.3.2.

2.5.6 Size Effect

Brittle and quasi-brittle materials like concrete exhibit differences when geometrically similar structures of different sizes are tested. The dependence of the peak strength on the dimension of the specimens is called *size effect*. This kind of effect can not be described by any theory that accounts failure by any type of stress-based criterion. Also, concrete ductility is a parameter strongly influenced by size effect. Geometrically similar structures of different sizes typical yield post-peak behavior characterized by early failures as the size increases. This effect can be predicted by fracture mechanics theories, and it is due to the fact that in a larger structure more strain energy is available to drive the propagation of the failure zone.

The size effect model [21] describes this effect by the two parameters: fracture energy G_f and the critical effective crack length c_f at peak load for an infinitely large test specimen. These parameters can be determined by

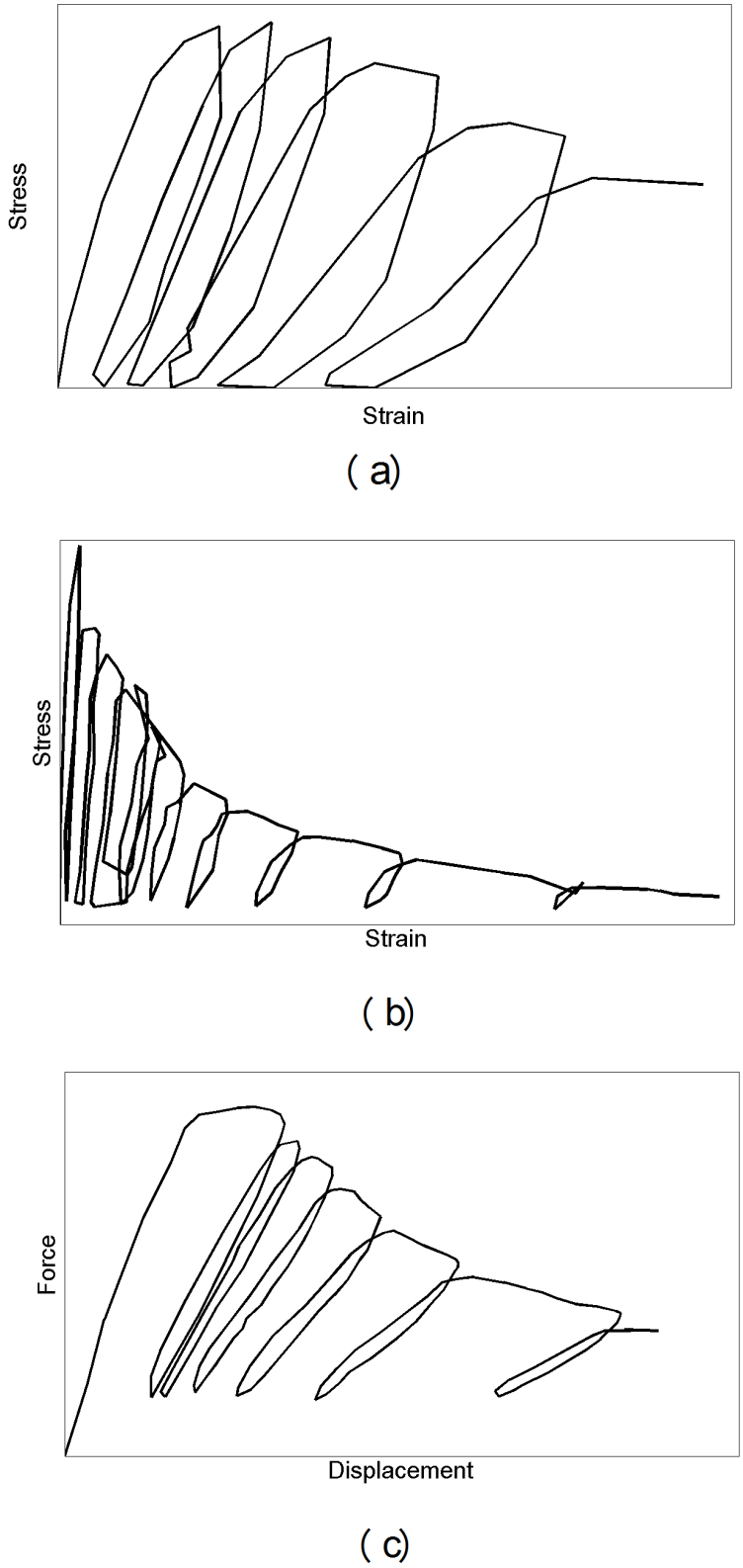

Figure 2.15: Cyclic response for different loads conditions: (a) compression, (b) tension, (c) bending

means of geometrically similar notched specimens of different sizes.

This effect has always been explained by means of the randomness of the strength value across the structure. The general example is that of a chain: the whole structure will fail when the weaker link reaches its failure load, so that the smaller the structure the more unlikely it is to encounter a weak element. This theory goes under the name of *Weibull's theory*, and according to it the probability of a structure to fail under a load P are:

$$Prob(P) = 1 - exp\left(- \int_V \left[\frac{\sigma(P, \boldsymbol{x})}{\sigma_0}\right]^m \frac{dV(\boldsymbol{x})}{V_r} \right) \tag{2.24}$$

$$\bar{\sigma}_N = \frac{\bar{P}}{bd} = \frac{1}{bd} \int_0^\infty (1 - Prob(P)) dP \tag{2.25}$$

in which $\bar{P}$ is the mean load, $\boldsymbol{x}$ is the coordinate vector, V volume of the structure, V_r the representative volume, m the Weibull modulus of the material and σ_0 a scale parameter.

The key point of this theory is the function $\sigma(P, \boldsymbol{x})$, which represents the stress acting at point $\boldsymbol{x}$. According to Weibull's theory, failure of the entire system occurs at crack initiation. Even if this concept is applicable to some structures, it is not the case in concrete elements. In fact, this theory can not take into account softening with consequent large micro-cracked zones ahead of the tip of a macrocrack. The pronounced inelastic deformation occurring and the macroscopic crack growth prior to collapse should be taken into account by a different stress distribution $\sigma(P, \boldsymbol{x})$. The principal problem in Weibull-type statistical explanations is that the size effect caused by nonlinear stress redistribution can not be taken into account. To do so, a fracture mechanics type of size effect theory must be adopted.

The energy-based size effect can be explained by considering a uniformly stressed panel with a crack of initial length $a = a_0$ (see Fig. 2.16). The existence of the crack of thickness h reduces the strain energy density $\sigma_N^2/2E$ to zero. When the crack band extends, there is an additional release of strain energy caused by the cross-hatched strip of horizontal dimension Δa.

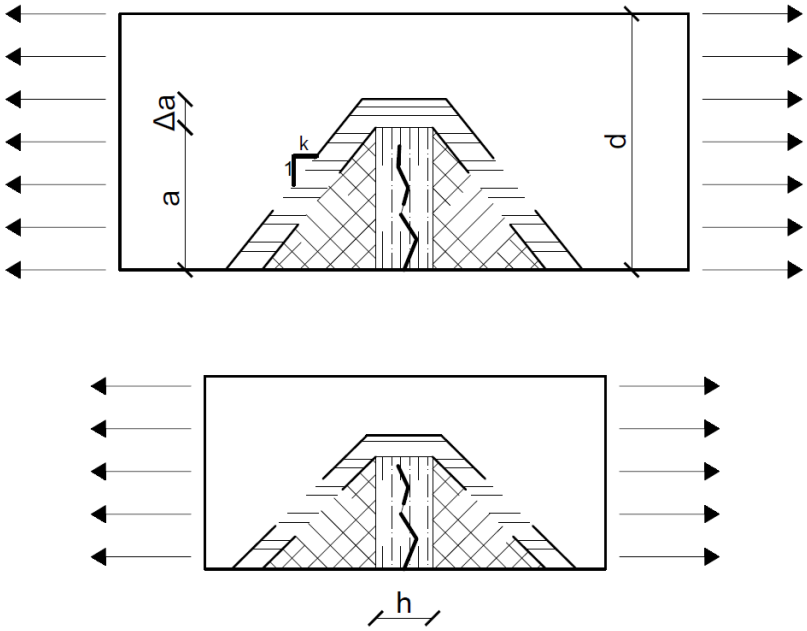

Figure 2.16: Schematic explanation of the size effect in concrete (from Bazant et al. [21])

This means that two geometrically similar panels will have different size of the ultimate crack band. This example illustrates how larger structures release more energy by means of the same extension of the crack. The energy released is $-\delta\Pi/\delta a = G_f b$ and:

$$\frac{1}{\Delta a}(h\Delta a + 2ka\Delta a)\frac{\sigma_N^2}{2E} = G_f b \tag{2.26}$$

where Π is the potential energy of the structure, b its thickness and G_f the fracture energy. The value of G_f is approximately constant and therefor it can be considered as a material parameter. Solving Eq. 2.25 for the nominal stress:

$$\sigma_N = \sqrt{\frac{(2G_f Eb/h)}{(1 + d/d_0)}} \tag{2.27}$$

where $d_0 = (h/2k)(d/a)$ is the reference size, h width of the crack band front. Eq. 2.27 is the size effect law proposed by Bazant [21]. Empirical evidences show that $d_0 \simeq nd_a$ where d_a is the maximum aggregate size and

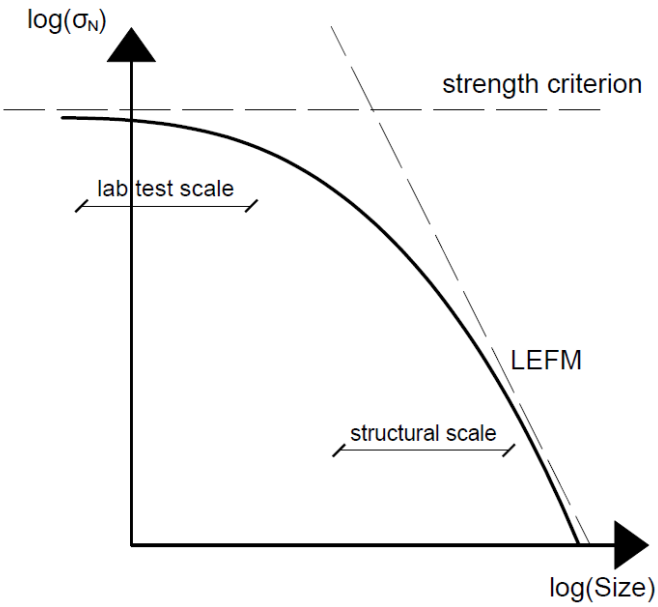

Figure 2.17: Size effect: nominal strength vs structural size

n is a parameter depending on the structure geometry.

Many tests have been carried out on this topic, taking into account different failure modes. Good agreement of Eq. 2.27 with the test results has been demonstrated for different failure modes. A graphical representation of the dependence of the nominal strength on the structural size dimension is given in Fig. 2.17.

Chapter 3

Theoretical Approach

This chapter will deal with the definition of the model, highlighting the peculiarities and unique feature of the random particle lattice model proposed.

First the generation of the model will be presented, highlighting the geometrical tools used to define the position of the particles, the connections between them and the technique to retrieve their inertial properties.

After the geometry of the model is defined, it is necessary to define the mechanical behavior of the connections. Two different approaches will be presented: a fully dynamic model that explicitly takes into account the normal-shear stress interaction among adjacent cells, and simplified static approach in which axial springs are used to generate the lattice.

Two different constitutive laws will be presented, highlighting the main characteristics. The technique to integrate the equations of motion, both in static and dynamic regime, will be presented, with a particular focus on the parallelization of the code. Since lattice models are generally demanding in terms of computing resources, techniques like parallel computing prove extremely useful.

Having defined the mechanical behavior of the elements and the integration methods, post-processing tools are described in order to visualize the so obtained results. Particular attention will be devoted to the graphical

representation of the crack patterns, being this one of the most appealing feature of the proposed particle lattice model approach.

3.1 Model Building - Geometrical Tools

The random particle lattice model is composed of a set of nodal sites, which represent the center of the simulated coarse aggregates, connected by uniaxial elements which inherit stiffness and inertial properties from a 3-dimensional tessellation of the domain. The generation of the model requires the use of different computational geometry tools. Three main steps are required:

1. Definition of the randomly placed particles
2. Triangulation of the previously defined set of points
3. Tessellation of the domain by means of a graph dual of the triangulation

The first step is required to define the spatial arrangement of the spherical particles simulating the coarse aggregate; the second one aims to the evaluation of the connection between them, while the third evaluates the contact areas on which the constitutive law is . The computational tools used are object of the next Sections.

3.1.1 Random Placement of Nodal Sites

The first step involves the definition of the nodal sites. According to the actual composition of the material, the nodes (considered as the centers of spherically-shaped inclusions) are placed in the domain by means of a pseudo-random coordinate generation technique.

The particle generation is performed into 3 steps:

1. Evaluation of the number of particles
2. Choose of the minimum modeled diameter

3. Random Generation of the Coordinates and Domain Filling

The three steps will be discussed in the following sections.

Number of Particles

With reference to the Mix Design procedure (see Sec. 2.4), the number of particles of each granulometric class are calculated as follows:

1. Calculate the total Volume of aggregate V_a in the sample:

$$V_a = V_t - V_w - V_c - V_{air} \tag{3.1}$$

where V_t is the total volume, V_w is the known water content, $V_c = (V_w\gamma_w)/(w/c\gamma_c)$ is the cement volume (γ_w and γ_c the volume weight of of water and cement, respectively, w/c the water to cement ratio), and V_{air} the trapped air volume.

2. Based on the given maximum aggregate diameter d_{max} and q exponent of the Andreasson curve (see Eq. 2.2), it is possible to evaluate the passing amount (%) for every granulometric class chosen (generally chosen equal to the nominal sieve sizes used in practice). Knowing the passing amount for every class, the retained percent is simply calculated as the difference between the adjacent classes' passing:

$$P_i = \left(\frac{D_i}{D_{max}}\right)^q \quad i = 1, .., n \tag{3.2}$$

$$R_i = P_{i+1} - P_i \quad i = 1, .., n \tag{3.3}$$

where R_i and P_i are the retained and passing percent amounts at sieve i, d_i the diameter of class i and n is the total number of sieves (ascending order).

3. Knowing the retained percent of every class, the total volume of the class is evaluated as:

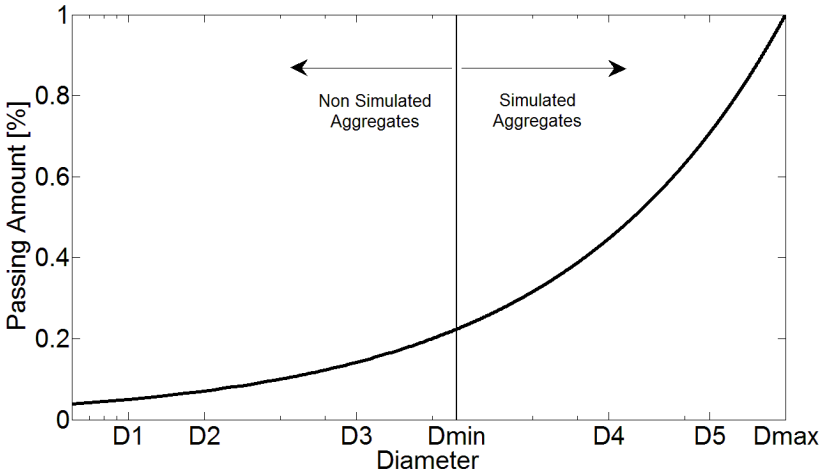

Figure 3.1: Real granulometric curve and chosen threshold for the minimum diameter of the particles

$$V_i = R_i \cdot V_a \qquad i = 1, .., n \tag{3.4}$$

from which the total number of particles in every class, n_i is calculated:

$$n_i = INT\left(\frac{V_i}{\left(\frac{\pi d_i^3}{6}\right)}\right) \qquad i = 1, .., n \tag{3.5}$$

with INT(x) defined as the integer part of x.

Minimum Diameter

In terms of principle, the mechanical parameters assigned to the connection should actually change based on the selected minimum aggregate size. That is because the facet response represent the behavior of finer scale phenomena associated with a particle size that is smaller than the chosen threshold [56]. With reference to Fig. 3.1, this means that the aggregate fraction representing the curve to the right of the chosen threshold is explicitly modeled by means of the generate particle distribution, while the remaining portion has to be lumped in the connections' constitutive law. However, in the lab tests used to validate the presented model (see Chapter 5), the granulometric curve and maximum diameter used for the concrete casting

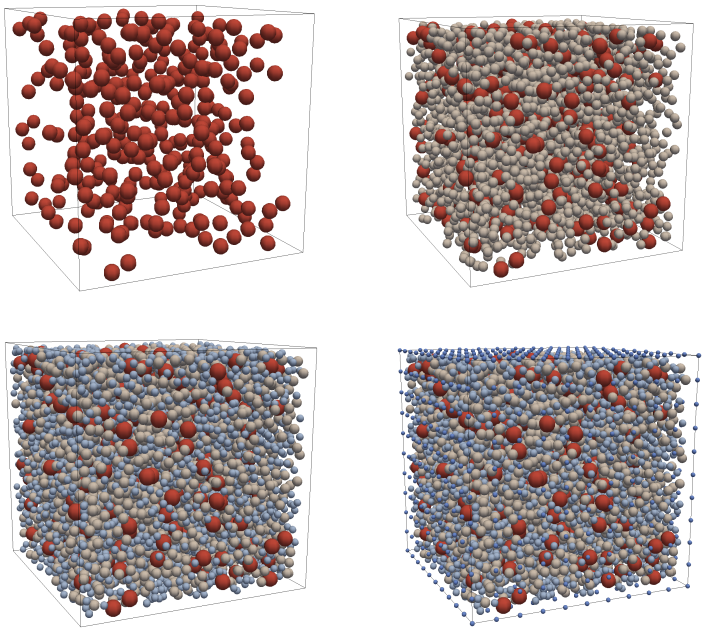

Figure 3.2: Insertion of the particles in the domain for three different granulometric sizes simulated and the external nodes

lie in a limited range. The minimum diameter chosen for the simulations is equal to 4.35 mm, which is generally considered as the limit value between coarse and fine aggregate. This choice aims to the use of the lowest feasible value while keeping computational costs reasonable. In every numerically generated specimen, however, at least 30% of the total aggregate volume was simulated. Such value is still extremely high when compared to continuum meso-scale approach examples.

Definition of the Particle Position

When the number of particles of every granulometric class is known, aggregate pieces are put in the domain from biggest to smallest. Called n_p the total number of particle this operation is performed through the following steps and repeated until all the aggregate pieces are successfully placed in the domain:

1. Random generation of the trial coordinate vector of the i-th particle

2. Insertion of the particle in the domain

3. Check to prevent any possible overlap with previously place particles

4. If the trial particle does not intersect any other aggregate piece in the domain, the trial coordinate is accepted and the counter of correctly placed particles is refreshed

The trial coordinates are generated by means of a pseudo-random number generator. The three components of the coordinate vector are generated by assuming a uniformly distributed probability function in the given interval.

The distance check is performed by taking into account the different diameters of the various particles, so that, for every new trial particle the following measures are calculated:

$$d_i = |\boldsymbol{x}_{trial} - \boldsymbol{x}_{prev,i}| \quad i = 1, .., n_{ins} \tag{3.6}$$

$$d_{test,i} = \eta_0 \cdot (r_{trial} + r_{prev,i}) \quad i = 1, .., n_{ins} \tag{3.7}$$

where d_i is the i-th distance among particles, $\boldsymbol{x}_{trial}$ the trial coordinate vector, $\boldsymbol{x}_{prev,i}$ the i-th previously placed particle of radius r_{trial} and $r_{prev,i}$ respectively, n_{ins} the number of correctly inserted particle up to that time. The parameter η_0 amplifies the test distance, in order to avoid particles to be too close, and the consequent formation of skinny tetrahedrons; since this parameter represents a constraint on the particle placement, the higher its value the longer the runtime required. Numerical investigations suggest that a value ≈ 1.15 can be used without slowing the generation process significantly

. The test is performed on the trial coordinate vector in the following way: if every d_i calculated is greater than the test distance $d_{test,i}$ the particle is accepted and added to the model, otherwise an overlap with a previously inserted sphere is occurring and the trial coordinate vector is discarded. The first particle is added without performing the test.

Table 3.1: Number of simulated particles

D_i	n_i	V_{f_i}
10	348	9%
6.35	2898	19%
4.75	3670	10%
Total	6916	38%

As shown in [87], if the trial coordinate is checked against every other previously inserted particle, the algorithm has a $O(n^2)$ complexity. It has been shown [87] that by using a Grid Search Algorithm [61] the complexity is reduced to $O(n)$. This algorithm, in fact, only checks every particle against the ones lying in its 3D Moore neighborhood [132]. Such neighborhood is composed of a box of chosen dimension containing the trial particle and all the boxes that share a face, edge or vertex with the central box.

After all the particles have been succesfully place, fictitious zero-diameter particles are added to the set in order to correctly simulate the surface and edges of the specimen. These external nodes can be randomly or regularly spaced on the surface and edges of the specimen. They are inserted by respecting a minimum distance criterion, in order to have lattice connection of approximately same size as in the interior part of the specimen.

Fig. 3.2 shows the steps taken to build a 150 mm cube. The size and number of particles of each granulometric phase is given in Table 3.1, together with their volume fraction.

3.1.2 Delaunay Triangulation

After the nodes have been successfully placed, it is necessary to define their connectivity (i.e. to evaluate which aggregate pieces share forces).

One efficient way to do this is to perform a triangulation (in 2D) or a tetrahedralization (in 3D) of the previously generated set of points. This operation is called *Delaunay Triangulation* (or *tetrahedralization*) of the

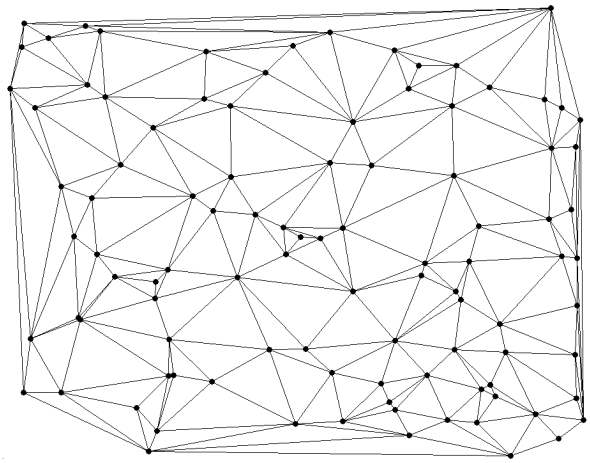

Figure 3.3: Delaunay triangulation for a set of 100 randomly distributed points on a plane

domain after Boris Delaunay [43].

A Delaunay Triangulation for a given set of points **P** in a plane is a trangulation DT(**P**) such that no point in **P** lies inside the circumcirle of any triangle in DT(**P**). The appealing characteristic of Delaunay Triangulation is that they maximize the minimum angle of all the angles of the triangles, meaning that it avoids skinny (badly shaped) triangles. The triangulation takes its name from Boris Delaunay [43]. Fig. 3.3 shows an example of a Delaunay Triangulation performed on a set of 100 randomly placed points.

For a set of points on the same line the Delaunay Triangulation does not exist, while for four or more points on the same circle the triangulation is not unique since different triangles combinations meet the requirement that the circumcircles have empty interiors.

By considering circumscribed spheres, the notion of Delaunay Triangulation extends to three dimensions. The three-dimensional version of the triangulation is rather called *Tetrahedralization*, since it involves the use of tetrahedrons instead of triangles.

Algorithms

Different algorithms are used nowadays to compute Delaunay Triangulations.

- *Flip algorithms*: if a triangle violates the Delaunay Triangulation, it is possible to flip one of its edges. By using this concept, this algorithm constructs any triangulation of the points and then flips edges until every triangle is an admissible one. This algorithm only works for 2-dimensional problems and has complexity $O(n^2)$

- *Incremental*: the most straightforward way of efficiently computing the Delaunay triangulation is to repeatedly add one vertex at a time, re-triangulating the affected parts of the graph. When a new point is added, the triangle containing it is split into three parts, and then the flip algorithm is applied. Over all the vertices this algorithm takes $O(n\,logn)$ time. While the technique extends to higher dimension [48], the runtime can be exponential in the dimension even if the final Delaunay triangulation is small.

- *Divide and Conquer*: in this algorithm, one recursively draws a line to split the vertices into two sets. The Delaunay triangulation is computed for each set, and then the two sets are merged along the splitting line. Using some computational artifice, the merge operation can be done in time $O(n)$, so the total running time is $O(n\,logn)$ [83]. This algorithm has been shown to be the fastest Delaunay Triangulation Technique [120].

Delaunay Triangulations are used in many different applications nowadays, among which the most important ones are:

- digital terrain modeling, by triangulating the cloud of points evaluated by radar or satellite technologies;

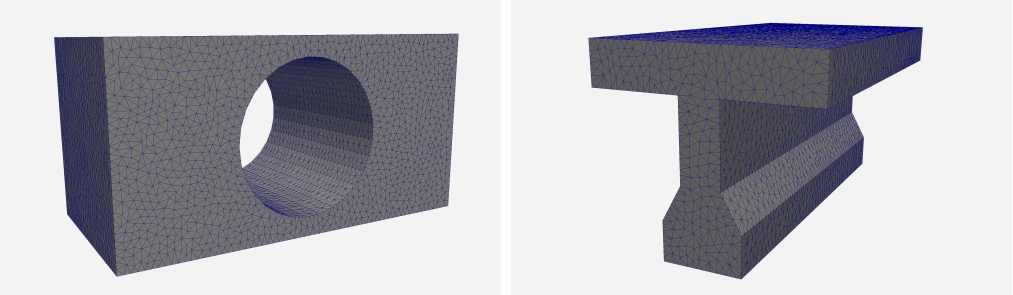

Figure 3.4: Constrained Delaunay triangulations

- density or intensity of point samplings measures by means of the so called Delaunay Triangulation Field Estimator (DTFE) [107];
- automatic mesh algorithms.

Delaunay triangulations are often used to build meshes for space-discretized solvers such as the finite element method and the finite volume method of physics simulation, because of the angle guarantee and because fast triangulation algorithms have been developed. Typically, the domain to be meshed is specified as a coarse simplicial complex; for the mesh to be numerically stable, it must be refined, for instance by using Ruppert's algorithm [106].

The increasing popularity of finite element method and boundary element method techniques increases the incentive to improve automatic meshing algorithms. However, all of these algorithms can create distorted and even unusable grid elements. Fortunately, several techniques exist which can take an existing mesh and improve its quality. For example, smoothing (also referred to as mesh refinement) is one such method, which repositions nodal locations so as to minimize element distortion. The stretched grid method allows the generation of pseudo-regular meshes that meet the Delaunay criteria easily and quickly in a one-step solution.

3.1.3 Non-Convex Domain Meshing

The collection of all the tetrahedrons in the Delaunay Triangulation constitutes the *convex hull* [76] of the given set of points. This means that

it is not possible to build non-convex polygons with a regular triangulation of its points.

In order to mesh non-convex objects, it is necessary to enforce that the tetrahedrons in the triangulation do not cross the bounding surfaces in the domain. By doing so, a *Constrained Delaunay Triangulation* [32] is obtained: it is a generalization of the Delaunay triangulation that forces certain required segments and surfaces into the triangulation, in order to obtain a given shape. Since the Delaunay Triangulation is usually unique, the enforced new edges usually do not satisfy the Delaunay condition, so that the constrained Triangulation often is not a Delaunay Triangulation itself. This drawback, anyways, does not hamper the applicability of such Tetrahedralization in the proposed lattice modeling approach, since the so calculated tetrahedrons still represent the particles connection, and the used tessellation is dual to it.

Algorithms

Constrained Delaunay Triangulation algorithms can be divided in the same way as Delaunay Triangulation ones:

- *Flip algorithms*: the domain is divided into two sub-areas by means of an imaginary sweep-line, leaving one side of the domain triangulated while the other is not. Each step adds a new triangle by connecting a new point to the boundary [53] [113].

- *Incremental*: this group represents the most popular and easy to implement algorithms; the triangulation is built gradually by adding vertices or edges [64] [136]. This group can be divided in *incremental search* and *incremental insertion* algorithms.

- *Divide and Conquer*: the input set is split into smaller parts, by using different approaches such as ribbons or areas, the triangulation is performed on the smaller sets that are merged together. Even if

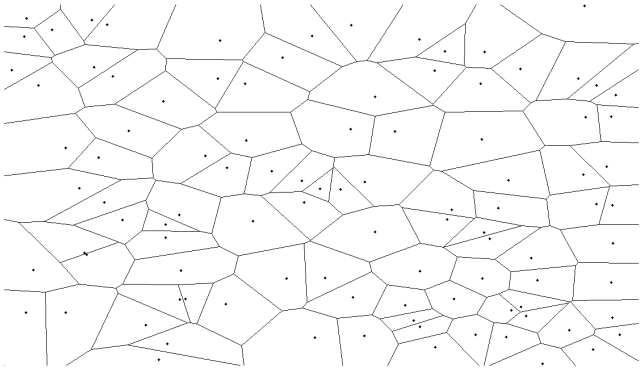

Figure 3.5: Voronoi Diagram of 100 Randomly Generated Points on a Plane

this last step is demanding, this type of algorithms is particularly convenient for parallel processing [32].

3.1.4 Modified Voronoi Diagram

When the particles have been placed in the domain and the connecting between them have been retrieved by means of the Delaunay Triangulation, it is necessary to tessellate the domain by means of a dual graph of the Triangulation used. This operation is required in order to define the cross sectional areas of every strut in the mesh.

A *tessellation* of a flat surface is the tiling of a plane using one or more geometric shapes, called tiles, with no overlaps and no gaps. The bi-dimensional tessellation can be generalized to higher dimensions and a variety of geometries. By *dual graph* of a given graph G, one refers to a graph that has a vertex for every face of G, an edge whenever two faces of G are separated by an edge. Thus, each edge of G has a corresponding dual edge, connecting the two faces the original edge divides.

The straightforward choice for the tessellation technique to use for the generated lattice would be the *Voronoi Diagram* [46]. It is a partitioning of a plane into regions based on the distance to points. The set of points is specified beforehand, and for each one a corresponding region is built

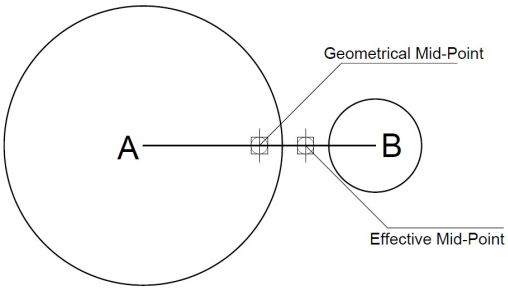

Figure 3.6: Effective and geometrical midpoints of an edge

consisting of all points closer to that than to any other. The regions are called *Voronoi Cells*. The Voronoi Diagram is dual to the Delaunay Triangulation.

Let $\mathbf{X}$ be a metric space with a distance function d. The Voronoi Cell R_k associated with the node P_k:

$$R_k = \{x \in \mathbf{X} | d(x, P_k) \leq d(x, P_j) \text{ for all } j \neq k\} \tag{3.8}$$

In the case of a finite-dimensional Euclidean space, each site is a point, there are finitely many points and all of them are different, then the Voronoi cells are *convex polytopes* and they can be represented in a combinatorial way using their vertices, sides, 2-dimensional faces, etc. Sometimes the induced combinatorial structure is referred to as the Voronoi diagram. However, in general the Voronoi cells may not be convex or even connected. In the three-dimensional Euclidean space, each Voronoi Polygon R_k is associated with its generator point P_k. Then, all locations in the Voronoi Polygon are closer to the generator point of that polygon than any other generator point in the Voronoi Diagram.

Fig. 3.5 shows the Voronoi diagram and Delaunay triangulation for 100 randomly generated point on a plane.

Even if the Voronoi Diagram would be the straightforward choice, it is not desirable in particle simulations, since it would select areas that may intersect the aggregate. This issue is described in Fig. 3.6, for the selection of the effective midpoint on the six edges of each tetrahedron. The surface

of the cells constructed by the tessellation must be contained in the matrix surrounding the particles, since the paste is the location of possible failures. The particles have different diameters, so that the geometrical midpoint on a strut connecting their centers may lie inside one of the aggregates. The same concept applies for the triangular faces and tetrahedrons center of mass. For this reason a different three-dimensional tessellation is used [57], as defined in the following section.

Geometrical and Effective Midpoints Calculation

In order to be able to define the contact area of the connections, the chosen tessellation must: (a) select cells contact area that lie inside the potential crack propagation zone (i.e. the mortar), (b) be dual to the Delaunay Triangulation used to retrieve the particles connectivity. This is performed by means of a *Modified Voronoi Diagram*, originally conceived by Bazant et al. [58]. The dual graph of the already generated Delaunay triangulation is obtained by defining 12 triangular facets per tetrahedron, so that the resisting area of every connection is built as an assemblage of all the facets pertaining to that edge. The basic concept is to build such triangular areas by connecting the effective center of mass of the 1-D (edges), 2-D (triangular faces) and 3-D (tetrahedrons) in the Triangulation (green parts in Fig. 3.7) in such a way that the resulting graph is still dual to the Delaunay Triangulation. The calculation of such points and the construction of the tessellation will be presented in the next paragraphs.

By *effective center of mass* it is intended the center of mass of the element calculated by subtracting the aggregate counterpart. These points will be referenced to as: (1) G_{ij} the effective center of mass of edge ij, G_{ijk} the effective center of mass of area ijk, and G_{ijkl} the effective center of mass of the tetrahedron $ijkl$ (see Fig. 3.7).

The effective center of mass of the 1-D edges, with reference to Fig. 3.6, is calculated as follows:

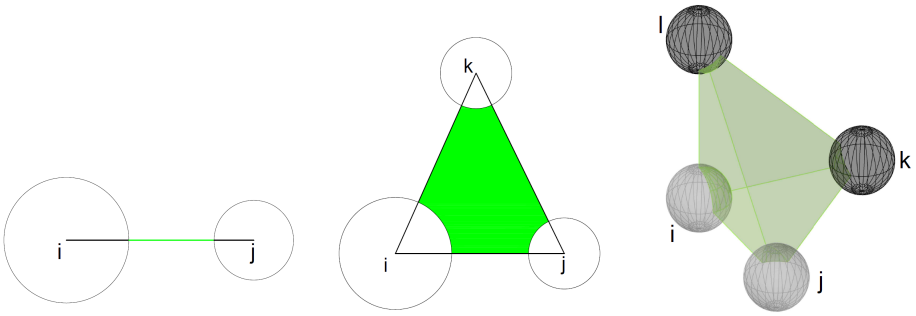

Figure 3.7: Effective length, area and volume

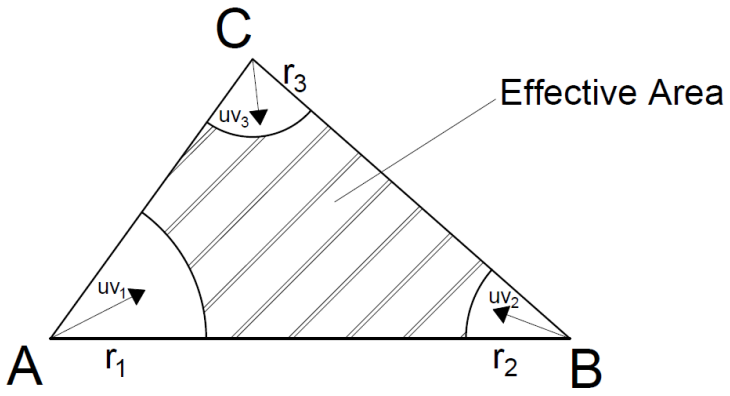

Figure 3.8: Effective and geometrical center of mass of the triangular areas

$$\boldsymbol{G}_{ij} = \boldsymbol{x}_i + \boldsymbol{uv}_{ij}(r_i + l_m/2) \tag{3.9}$$

where $\boldsymbol{x}_i$ is the coordinate vector of node i, $\boldsymbol{uv}_{ij}$ is the unit vector for the ij direction, r_i the radius of particle i and $l_m = l - (r_i + r_j)$ the length of the matrix part of the edge.

In order to evaluate the 2-D effective center of mass it is necessary to calculate the area and center of mass of the intersection between the triangle and the circles. With reference to Fig. 3.8:

$$A_{agg,i} = \frac{r_i^2 \cdot \beta_i}{2} \tag{3.10}$$

$$\mathbf{x_{tri,i}} = \mathbf{x_i} + \mathbf{uv}_i \cdot \frac{2}{3} r_i \frac{[sin(\beta_i/2)]}{\beta_i/2} \qquad i = 1, 2, 3 \tag{3.11}$$

where β_i is the i-th angle and $\mathbf{uv}_i$ the unit vector for its bisector. Knowing the values of the area and the center of mass for every arc of the circle, the

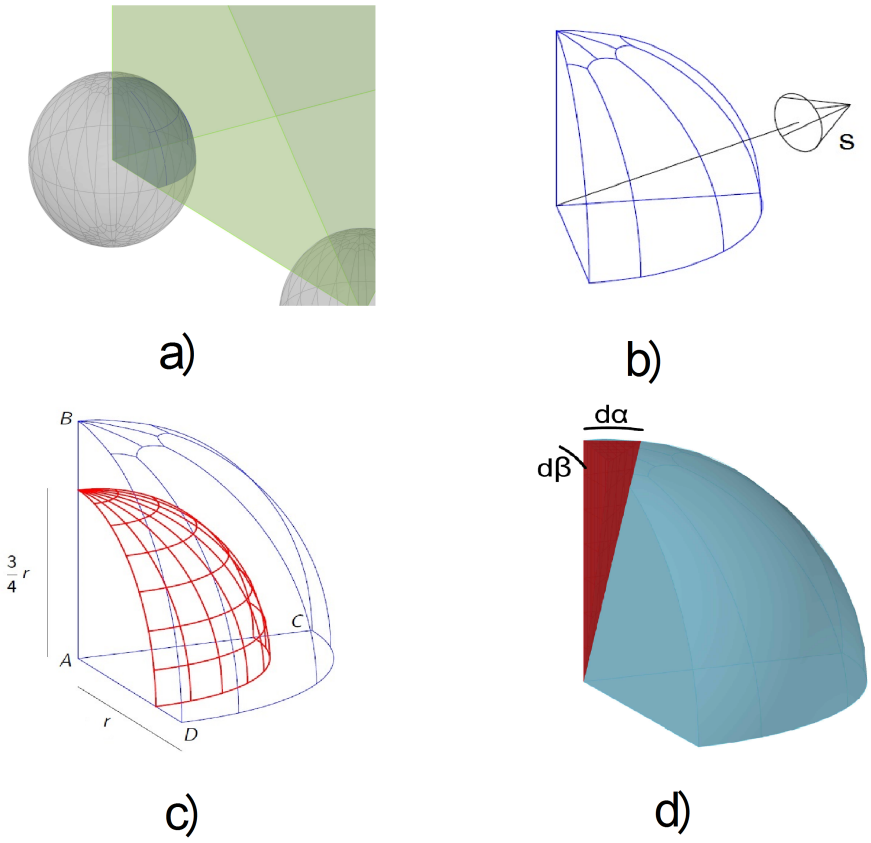

Figure 3.9: Effective volume and center of mass of the tetrahedrons: (a) 3-D view of the intersection, (b) curvilinear abscissa s, (c) spherical triangle center of mass, (d) double integration

effective center of the triangle is calculated as:

$$A_{eff} = A_{tri,ijk} - \sum_{i=1}^{3} A_{agg,i} \tag{3.12}$$

$$\mathbf{G}_{ijk} = \frac{A_{tri,ijk} \cdot \mathbf{x}_{g,tri} - \sum_{i=1}^{3} A_{agg,i} \cdot \mathbf{x_{tri,i}}}{A_{eff}} \tag{3.13}$$

where $A_{tri,ijk}$ is the total area of the ijk triangle and $\mathbf{x}_{g,tri}$ its center of mass coordinates.

The intersection between the tetrahedron and the inclusion is a solid region composed of a spherical triangle and 3 circular sectors. To calculate the volume, it is useful to use the following procedure. Since the area of the spherical triangle is given by:

$$A = E \cdot r^2 \tag{3.14}$$

where the spherical excess $E = \pi - \beta_1 - \beta_2 - \beta_3$ and r is the radius of the sphere, it is convenient to write the area as a function of the curvilinear abscissa $\mathbf{s}$ (see Fig. 3.9). The volume is then calculated as:

$$\begin{aligned} V_{agg,i} &= \int_0^r A(s)\, ds = \\ &= \int_0^r E_i \cdot s^2\, ds = \frac{1}{3} E_i \cdot r_i^3 \end{aligned} \tag{3.15}$$

In order to calculate the center of mass of the intersection, it is noticed that every $d\alpha$ and $d\beta$ increments in the two azimutal directions generate a tetrahedron (see Fig. 3.9), whose center of mass is calculated as $\mathbf{x_g} = \frac{3}{4} r \cdot \mathbf{s}$. So, to calculate the center of mass of the original 3D figure, it is sufficient to calculate the one of the 2D red surface in figure. This yields:

$$\mathbf{x}_{tet,i} = \mathbf{A} + \left(\frac{3}{4}\frac{r_i}{2E_i}\right)\left[\frac{\mathbf{b}\times\mathbf{c}}{|\mathbf{b}\times\mathbf{c}|} B\hat{A}C + \frac{\mathbf{b}\times\mathbf{d}}{|\mathbf{b}\times\mathbf{d}|} B\hat{A}D + \frac{\mathbf{c}\times\mathbf{d}}{|\mathbf{c}\times\mathbf{d}|} C\hat{A}D\right] \tag{3.16}$$

Having calculated the values of the volume and center of mass of all the aggregate counterparts, the effective center of mass of the tetrahedron is evaluated as:

$$V_{eff} = V_{tet,ijkl} - \sum_{i=1}^{4} V_{agg,i} \tag{3.17}$$

$$\mathbf{G}_{ijkl} = \frac{V_{tet,ijkl} \cdot \mathbf{x}_{g,tet} - \sum_{i=1}^{4} V_{agg,i} \cdot \mathbf{x_{tet,i}}}{V_{eff}} \tag{3.18}$$

where $V_{tet,ijkl}$ is the volume of the $ijkl$ tetrahedron and $\mathbf{x}_{g,tet}$ its center of mass coordinates.

Fig. 3.10 shows the twelve triangles (two for each of the six edges) evaluated for every tetrahedron in the Triangulation. The connectivity of these facets is given in Table 3.2.

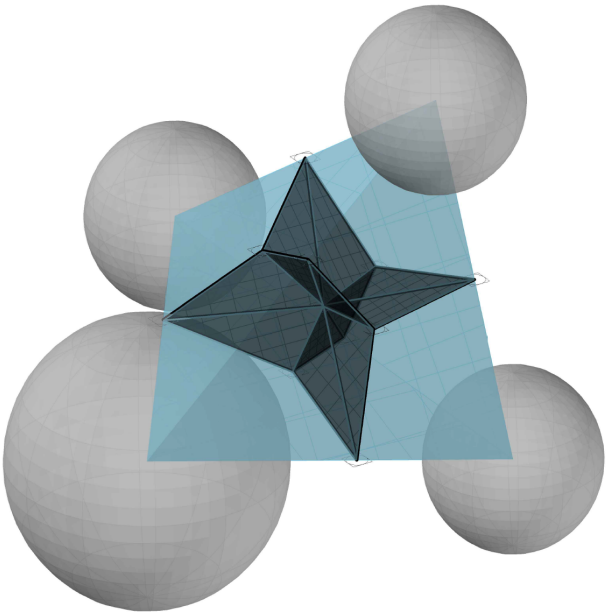

Figure 3.10: 3-D view of the twelve facets of the Modified Voronoi Diagram

Table 3.2: List of facets

Facet	Node 1	Node 2	Node 3	Edge
1	G_{AB}	G_{ABC}	G_{ABCD}	AB
2	G_{AB}	G_{ABD}	G_{ABCD}	AB
3	G_{AC}	G_{ABC}	G_{ABCD}	AC
4	G_{AC}	G_{ACD}	G_{ABCD}	AC
5	G_{AD}	G_{ABD}	G_{ABCD}	AD
6	G_{AD}	G_{ACD}	G_{ABCD}	AD
7	G_{BC}	G_{ABC}	G_{ABCD}	BC
8	G_{BC}	G_{BCD}	G_{ABCD}	BC
9	G_{BD}	G_{ABD}	G_{ABCD}	BD
10	G_{BD}	G_{BCD}	G_{ABCD}	BD
11	G_{CD}	G_{ACD}	G_{ABCD}	CD
12	G_{CD}	G_{BCD}	G_{ABCD}	CD

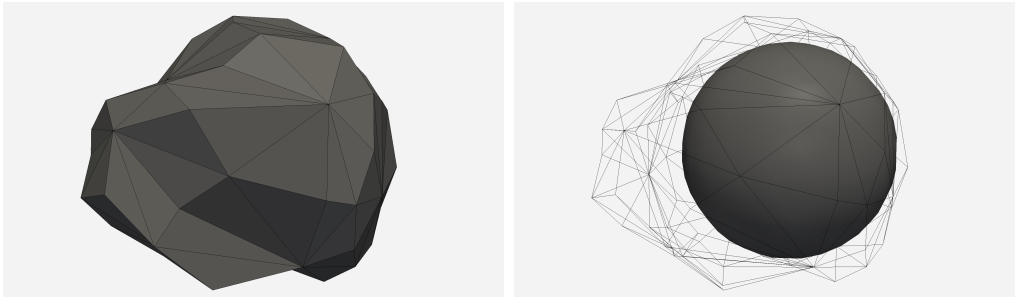

Figure 3.11: Two different views of one typical cell

3.1.5 Single Cell Representation

The so defined tessellation procedure has the following appealing features:

1. it is dual to the Delaunay Triangulation;
2. it only selects contact areas that lie inside the cement paste, which is the location of possible damage;
3. it shares with the Voronoi Diagram the duality with the Delaunay Triangulation and the subsequent capability of defining the contact areas between particles, even if the cells do not represent the collection of points that have the same distance to the generator point.

The collection of all the facets pertaining to the edges emanating from a point represents the point's cell (see Fig. 3.11) and it can be seen as its influence volume. Every particle will share forces with neighbors over the different surfaces of the cell. By exploiting the duality between the Triangulation and the Tessellation used, every aggregate connected by a Delaunay edge will also share a contact area on their respective cells.

3.1.6 Projection of the Facets and Local Axes

Fig. 3.12 shows two adjacent cells and their contact area. This area is composed a variable number of triangles, depending on how many tetrahedrons contain that particular edge (the total number of triangles will be equal to two times the number of tetrahedrons containing the connection).

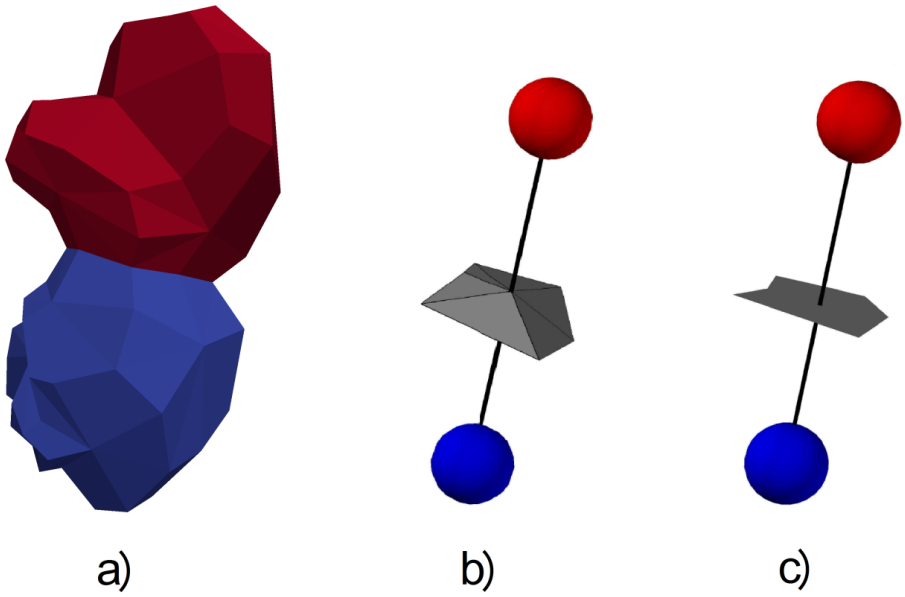

Figure 3.12: Adjacent cells and schematic representation of the contact area

The constitutive law is imposed on the projection of such triangles (Fig. 3.12) on a plane orthogonal to the connection. Such plane is identified by the effective mid-point of the edge G_{ij} and the $\mathbf{n}$ unit vector (see Fig. 3.13). This choice is due to the asymmetric behavior of concrete in tension and compression. If the constitutive law was imposed on the original facets, in fact, a simple shear in the connection, generated by a relative displacement vector orthogonal to the edge, would also imply tension or compression, leading to different results for the shear response, depending on its direction. This phenomenon is clearly non-physical, therefore the choice of considering the projected contact area is adopted.

3.2 Different Modeling Approaches

Having defined the model by means of the aforementioned computational geometry tools, the model must be completed with the displacement compatibility and mechanical behavior of the particles. Being a 3-dimensional model, the straightforward choice is to adopt a rigid-body motion scheme for the

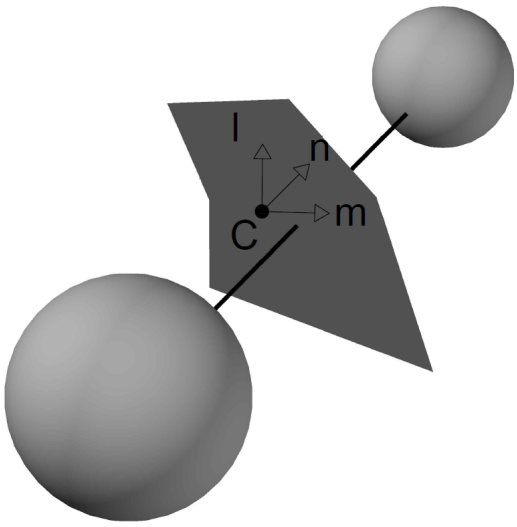

Figure 3.13: Connection center and definition of the element local axes

single cells and build the kinematics of the model based on this assumption. This choice leads to the definition of a "full model", in which the particles (and the surrounding cells) have 6 degrees of freedom (3 translations and 3 rotations).

After having defined the *fully dynamic model*, a simplified *spring network* model is proposed. Based on the findings of the complete model, the simplified one aims to reproduce the principal characteristics of the concrete behavior by only taking into account the normal forces shared between the cells, and so neglecting rotation of the particles.

The two models will be presented in the following Sections. A comparison between the obtained results will be given in Chapter 5.

3.3 Fully Dynamic Model

The *full model* will be described in the next Sections. In it, the interaction among adjacent cells is thought of as composed of both normal and shear forces. No bending moment forces are defined on the surface, as the bending

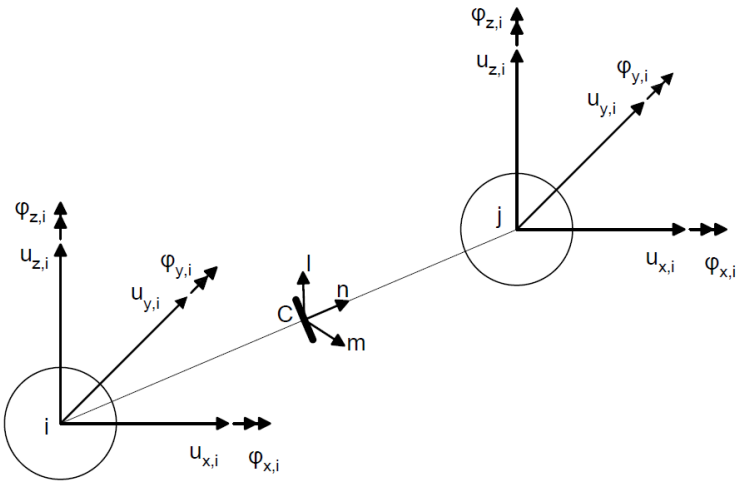

Figure 3.14: Particles degrees of freedom and connection local axes

mechanism is not proper of the meso-structure of the material [58]. The displacement of every point of the cell is described by means of rigid body motion, which center is the center of the spherical inclusions (i.e. the particle) generating the cell. The strain vector in the strut is evaluated as the displacement jump calculated in the geometric center of the connected area (see Fig. 3.13), divided by the length of the element. The constitutive law is capable of representing the elastic behavior of the material, as well as the fracturing (tension, tension and shear) and frictional (compression, compression and shear) nonlinear response. Computations are carried out by means of an explicit integration scheme (see Sec. 3.3.3).

3.3.1 Kinematics

Each cell is considered to be rigid, so that the displacement of any point can be calculated as:

$$\mathbf{u}(\mathbf{x}) = \mathbf{u}_i + \theta_i \times (\mathbf{x} - \mathbf{x}_i) = \mathbf{A}_i(\mathbf{x})\mathbf{U}_i \tag{3.19}$$

where $\mathbf{A}_i$ is:

$$\mathbf{A}_i(\mathbf{x}) = \begin{bmatrix} 1 & 0 & 0 & 0 & z - z_i & y_i - y \\ 0 & 1 & 0 & z_i - z & 0 & x - x_i \\ 0 & 0 & 1 & y - y_i & x_i - x & 0 \end{bmatrix} \tag{3.20}$$

The vector $\mathbf{U}_i = [\mathbf{u}_i \, \theta_i]^T$ collects the displacement and rotations of node i. By calculating the displacement of node C (see Fig. 3.14) thought of as belonging to the two adjacent cells of nodes i and j respectively, it is possible to define the relative displacement arising in the connection midpoint as:

$$[|\mathbf{u}_C|] = \mathbf{u}_{C,j} - \mathbf{u}_{C,i} \tag{3.21}$$

The strain components are obtained by dividing the displacement jump by the edge length:

$$\epsilon_N = \frac{\mathbf{n}^T[|\mathbf{u}_c|]}{l^e}, \; \epsilon_M = \frac{\mathbf{m}^T[|\mathbf{u}_c|]}{l^e}, \; \epsilon_L = \frac{\mathbf{l}^T[|\mathbf{u}_c|]}{l^e} \tag{3.22}$$

where $\mathbf{n}$, $\mathbf{l}$, $\mathbf{m}$ are the local axes of the strut (see Fig. 3.14). By using this definition it is possible to write:

$$\epsilon = \begin{bmatrix} \epsilon_N \\ \epsilon_L \\ \epsilon_M \end{bmatrix} = \mathbf{B}^{(e)}\mathbf{U}^{(e)} \tag{3.23}$$

where $\mathbf{U}^{(e)} = [\mathbf{U}_i \mathbf{U}_j]^T$ is the element displacement vector and $\mathbf{B}^{(e)}$ is the compatibility matrix:

$$\mathbf{B}^{(e)} = \frac{1}{l^e} \begin{bmatrix} -\mathbf{n}^T\mathbf{A}_1 & \mathbf{n}^T\mathbf{A}_2 \\ -\mathbf{l}^T\mathbf{A}_1 & \mathbf{l}^T\mathbf{A}_2 \\ -\mathbf{m}^T\mathbf{A}_1 & \mathbf{m}^T\mathbf{A}_2 \end{bmatrix} \tag{3.24}$$

3.3.2 Constitutive Law

The constitutive law at the mesoscopic level must be able to simulate the different behavior of concrete in tension, compression and shear. For

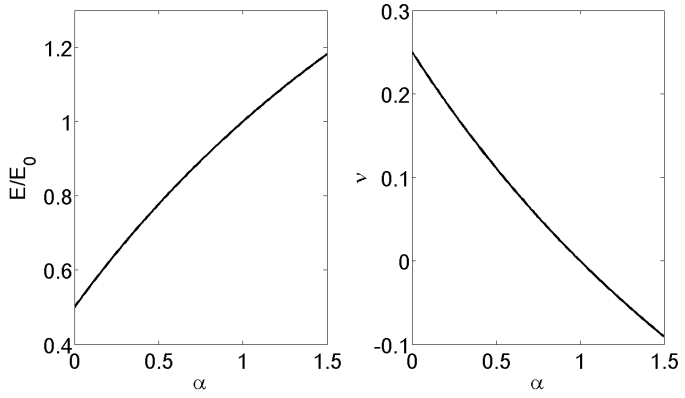

Figure 3.15: Evaluation of the macroscopic mechanical properties

this reason it is necessary to define the following:

$$\text{Elastic Behavior} - \begin{cases} \text{Macroscopic Young's Modulus} \\ \text{Macroscopic Poisson's Ratio} \end{cases}$$

$$\text{Fracturing Behavior} - \begin{cases} \text{Tension-Shear Interaction (Failure Surface)} \\ \text{Irreversible Damage Measure} \\ \text{Fracture Energy Regularization} \end{cases}$$

$$\text{Frictional Behavior} - \begin{cases} \text{Compression-Shear Interaction (Failure Surface)} \\ \text{Volumetric-Deviatoric Split for Compressive Stress States} \\ \text{Pore Collapse and Rehardening} \end{cases}$$

The *Elastic Behavior* is assumed to be following the rules:

$$\begin{aligned} \sigma_N &= E_N \epsilon_N \\ \sigma_T &= E_T \epsilon_T = \alpha E_N \epsilon_T \end{aligned} \tag{3.25}$$

where $\sigma_T = (\sigma_L^2 + \sigma_M^2)^{1/2}$, $\epsilon_T = (\epsilon_L^2 + \epsilon_M^2)^{1/2}$, E_N is the Young's Modulus in the normal direction and α represents the E_T/E_N ratio. By analogy with

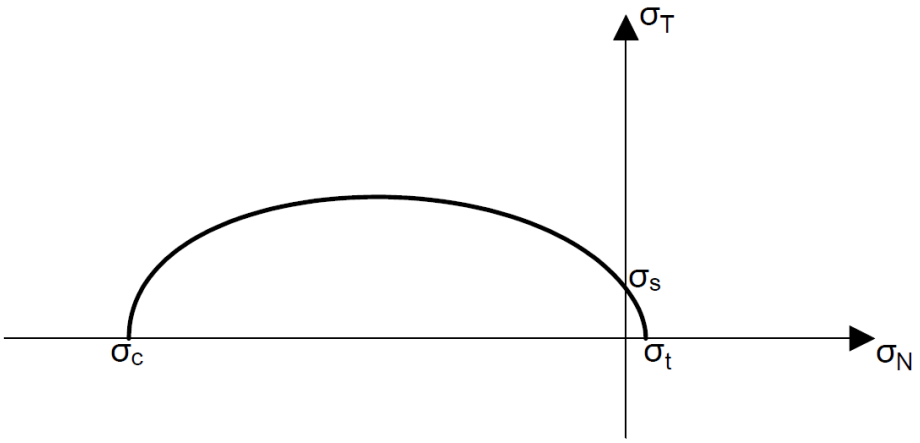

Figure 3.16: Stress boundary in the $\sigma_N - \sigma_T$ space

the *microplane formulation* with kinematic constraint and no deviatoric/volumetric split, the following rules can be obtained to evaluate the macroscopic material parameters [55]:

$$\begin{aligned} E_0 = \frac{1}{1-2\nu}E \iff E = \frac{2+3\alpha}{4+\alpha}E_0 \\ \alpha = \frac{1-4\nu}{1+\nu} \iff \nu = \frac{1-\alpha}{4+\alpha} \end{aligned} \tag{3.26}$$

The *Fracturing Behavior* is characterized by $\epsilon_N > 0$. Tensile and shear fracture is irreversible, so that the damage controlling parameter must be history-dependent. To this end, the evaluation of damage must be performed on the maximum value of the deformation attained by the element during the load history.

The interaction between the normal and tangential behavior of the struts is controlled through a stress boundary, which is defined as an ellipse in the $\sigma_N - \sigma_T$ space (see Fig. 3.16), defined by the σ_t, σ_c and σ_s values:

$$\sigma_N(\sigma_N - \sigma_c - \sigma_t) - \frac{\sigma_c\sigma_t}{\sigma_s^2}\sigma_T^2 = -\sigma_c\sigma_t \tag{3.27}$$

It is useful to introduce the *effective stress and strain* [58], defined as:

$$\epsilon = \sqrt{\epsilon_N^2 + \alpha\epsilon_T^2}\,, \quad \sigma = \sqrt{\sigma_N^2 + \frac{\sigma_T^2}{\alpha}} \tag{3.28}$$

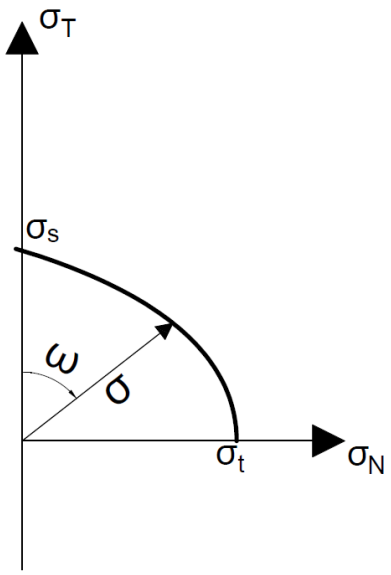

Figure 3.17: Geometrical representation of the effective stress and coupling strain

and the *coupling strain*:

$$tan\,\omega = \frac{\epsilon_N}{\sqrt{\alpha}\epsilon_T} = \frac{\sigma_N\sqrt{\alpha}}{\sigma_T} \Rightarrow \begin{cases} \sigma_N & = \sigma\, sin\omega \\ \sigma_T & = \sqrt{\alpha}\,\sigma\, cos\,\omega \end{cases} \tag{3.29}$$

By substituting the expressions for σ_N and σ_T in the stress boundary (Eq. 3.27) it is possible to reduced the problem to a 1-D scalar equation in which σ is the only unknown. It follows:

$$\sigma(\omega) = \frac{sin\omega\,(\sigma_C + \sigma_T) + \sqrt{sin^2\omega\,(\sigma_c + \sigma_t)^2 - 4\sigma_c\sigma_t(sin^2\omega - cos^2\omega\,\alpha\sigma_c\sigma_t/\sigma_s^2)}}{2(sin^2\omega - cos^2\omega\,\alpha\sigma_c\sigma_t/\sigma_s)} \tag{3.30}$$

so that ω represents the angle that the stress state line creates with the positive side of the σ_T axis, while $\sigma(\omega)$ the distance from the origin to the stress boundary for that direction. A graphical interpretation is given in Fig. 3.17

The fracturing mesoscale behavior of concrete exhibits softening for both normal and tangential strain histories. This phenomenon is modeled by imposing that the evolution of the stress boundary follows the exponential rule:

$$\sigma_b(\omega) = \sigma_0 \, e^{-\frac{H}{\sigma_0}(<\epsilon_1 - \epsilon_0>)} \tag{3.31}$$

where ϵ_0 represents the yielding strain associated with the current value of ω, and ϵ_1 is a history-dependent measure of the maximum damage achieved by the element:

$$\begin{aligned} \epsilon_1 &= \sqrt{\epsilon_{N,max}^2 + \alpha \epsilon_{T,max}^2} \\ \epsilon_0 &= \sigma(\omega)/E \end{aligned} \tag{3.32}$$

One of the main advantages in using a lattice approach is the possibility to enforce the correct energy dissipation under basic fracturing modes on the 1-dimensional elements composing the domain. By using scalar relationships between stresses and strain it is possible to scale the constitutive law to impose that every connection dissipates the desired energy during fracture processes. This procedure is needed since damage localizes also at the mesolevel [58].

The fracture energies for pure tension G_t and pure shear G_s are thought of as material properties [21] and therefore it is constant. Based on these values it is possible to evaluate the H parameter to be used in Eq. 3.31 to obtain a value of the fracture energy density in the element to satisfy $G_f = l \int_0^\infty \sigma d\epsilon$ (see Eq. 1.2). After having calculated the values of H for the two basic modes of fracture:

$$\begin{cases} H(\omega = 0) = H_s = \frac{2\alpha E_0}{(2\alpha E_0 G_S)/(\sigma_s^2 l) - 1} & \text{pure shear} \\ \\ H(\omega = \pi/2) = H_t = \frac{2E_0}{(2E_0 G_T)/(\sigma_t^2 l) - 1} & \text{pure tension} \end{cases} \tag{3.33}$$

the transition between pure shear ($\omega = 0$) and pure tension ($\omega = \pi/2$) is supposed to be smooth and governed by the following exponential equation.

$$H(\omega) = H_s + (H_t - H_s) \left(\frac{2\omega}{\pi} \right)^{n_t} \tag{3.34}$$

Eq. 3.34 shows that the exponent n_t influences the shape of the function. Fig. 3.18(f) shows different curves obtained by varying the value of the parameter; it is shown how higher values of n_t correspond to a more ductile response at the mesolevel.

The definition of the fracturing behavior is then completed by the loading-unloading rules. When unloading occurs, the element releases stresses elastically (with stiffness equal to E_N) until its value gets to 0. At that point the stress remains null while the deformation diminishes. While reloading, the same elastic modulus is used, and the stress boundary value σ_b defined in Eq. 3.31 is enforced, so that the stress can never exceed the threshold value obtained at the maximum strain achieved by the strut during the loading history. A graphical interpretation of this behavior is given in Fig. 3.18, where the cyclic behavior of the struts is presented.

The *Frictional Behavior* ($\epsilon_N <= 0$) at the mesoscale must be able to reproduce the frictional effects that lead to an increase in the shear strength and ductility, together with triaxial hardening and pore collapse for volumetric compression. The interaction between the normal and tangential behavior of the struts is supposed to be controlled by the ellipse in the $\sigma_N - \sigma_T$ space defined in Eq. 3.27.

Compressive stress states ($\epsilon_N < 0$) are highly dependent on the volumetric effects [55]. In order to take this aspect into account, negative normal strain is decomposed in the volumetric and deviatoric part:

$$\epsilon_v = \epsilon_N + \epsilon_D \tag{3.35}$$

Fig. 3.19 shows the typical arrangement of the resisting area of one connection in the model. The different colors of the facets represent the different tetrahedrons in which they are contained, so that every couple of triangular areas forming the cross section of the element experiences a different level of volumetric strain. The value of ϵ_v to be used in Eq. 3.35 is calculated as:

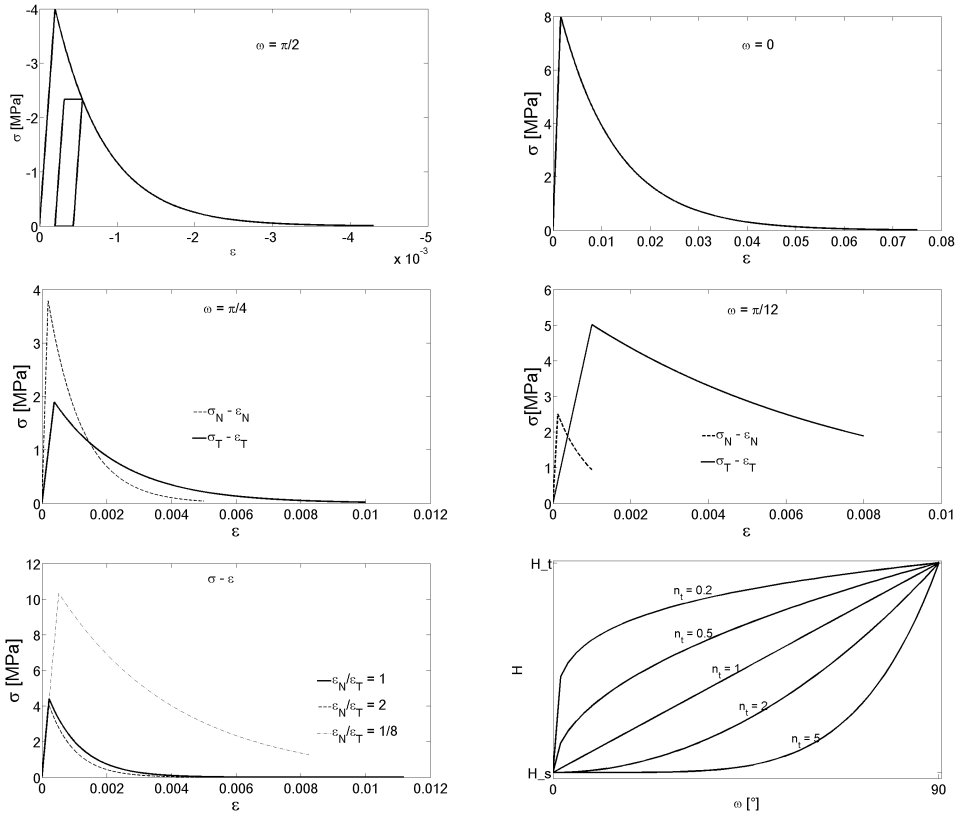

Figure 3.18: Fracturing behavior of the struts: (a) cyclic tension, (b) shear, (c) tension with low shear, (d) tension with high shear, (e) effective stress for different load paths, (f) softening modulus as a function of ω

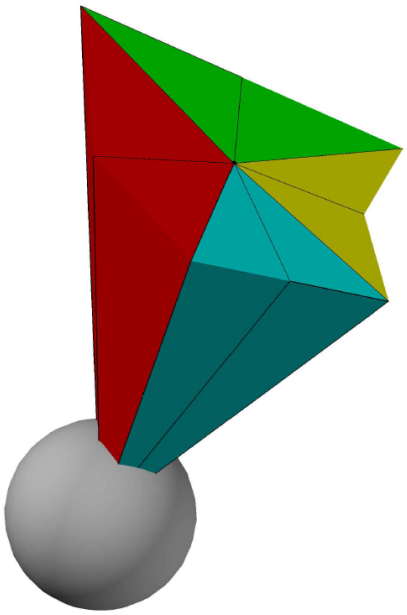

Figure 3.19: Graphical representation of the facets composing the resisting area of one element; different colors represent the different tetrahedrons generating the facets, each one experiencing a different level of volumetric strain

$$\epsilon_v = \sum_{i=1}^{n_f} \epsilon_{v,i} \frac{A_{f,i}}{A_t} \tag{3.36}$$

where he volumetric strain in every tetrahedron is calculated by means of Eq. 3.37, in which the particle rotations are neglected.

$$\epsilon_V = (V - V_0)/V_0 \tag{3.37}$$

The information on the average volumetric deformation acting in the connection is used to the define the compressive stress boundary. It is well known that the post-peak compressive behavior is strongly influenced by volumetric effects, to model this phenomenon the stress boundary in compression is dependent on ϵ_v as follows:

$$\sigma_b = \begin{cases} \sigma_c & \text{if} \epsilon_v \geqslant 0 \\ \sigma_c e^{H/\sigma_c(-\epsilon_v - \epsilon_c)} & \text{if} \epsilon_v < 0 \end{cases} \tag{3.38}$$

Eq. 3.38 shows that the post-peak compressive behavior must be able to reproduce the hardening response induced by the pore collapse under high volumetric deformations, while a perfectly plastic behavior is assumed in case of positive volumetric deformation.

Also, the hardening modulus H is thought to be dependent on the volumetric and deviatoric deformation acting in the element:

$$H = H_c/(1 + k_2 < r_{dv} - k_1 >) \tag{3.39}$$

where r_{dv} is the deviatoric to volumetric strain ratio, and k_1,k_2 are two material parameters.

The loading-unloading rules in compression follow the same rule used for the cohesive behavior: the element unloads elastically to zero stress, and then σ_N remains null up to zero deformation. The difference with the tension side of the stress-strain response lies in the fact that there is no damage due to compressive actions, meaning that the reloading branch will always merge with the virgin load curve.

A graphical interpretation of the compressive behavior of the struts is given in Fig. 3.20, in which the cyclic response for both positive and negative volumetric deformation are reported.

The description of the frictional behavior of the lattice struts is then completed by defining the shear response under compression. It is supposed to be dependent on the same ellipse in the $\sigma_N - \sigma_T$ plane. The evolution of the boundary is governed by the exponential law:

$$\sigma_b = \sigma_{T,0}\, e^{-\frac{H}{\sigma_{T,0}}<\epsilon_T - \epsilon_{T,0}>} \tag{3.40}$$

where $\sigma_{T,0} = \sigma(\omega)\, cos\omega\, \sqrt{\alpha}$ (see Eq. 3.29). The shear post-peak behavior, similarly to the fracturing behavior case already described, is defined by imposing the two values of the softening modulus H:

$$\begin{cases} H(\omega = 0) = H_s = \frac{2\alpha E_0}{(2\alpha E_0 G_S)/(\sigma_s^2 l) - 1} & \text{pure shear} \\ \\ H(\omega = -\pi/2) = H_c = 0 & \text{pure compression} \end{cases} \tag{3.41}$$

so that the shear response smoothly from tension to compression. A fictitious perfectly plastic behavior is supposed for the case of pure compression in order to define the following variation rule for the parameter H as a function of ω:

$$H = H_s - H_s \left(\frac{-2\omega}{\pi} \right)^{n_c} \tag{3.42}$$

Similarly to the tensile normal strain case, the parameter n_c controls the shape of the function. In this case, lower values of n_c will provide a more ductile response (see Fig. 3.20).

A graphical interpretation of the shear response of the lattice elements is given in Fig. 3.20, where the shear response is shown for different levels of axial strain.

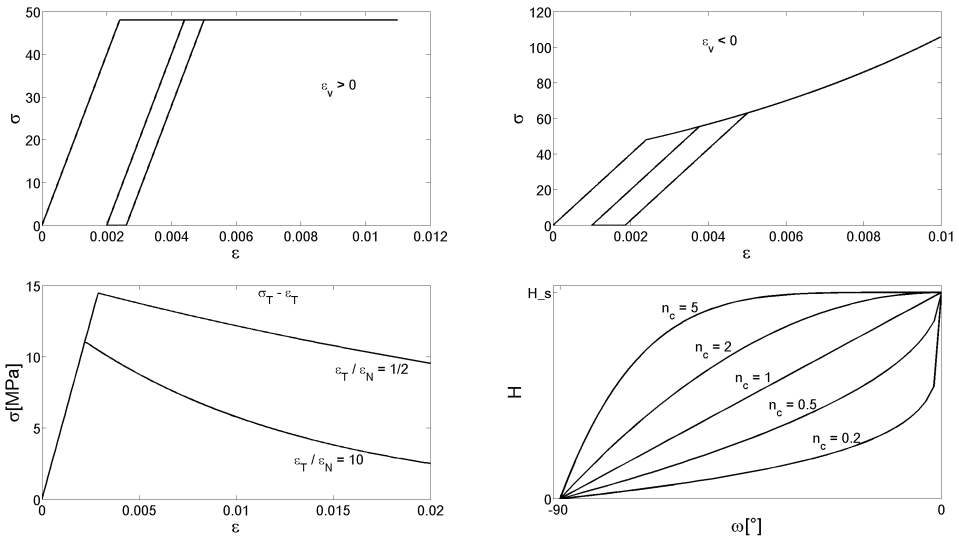

Figure 3.20: Frictional behavior of the struts: (a) positive volumetric compression, (b) negative volumetric compression, (c) shear-compression interaction, (d) shear softening modulus variation as a function of ω

3.3.3 Central Difference Scheme for the Dynamic Integration of the Equations of Motion

The equations of motion of the lattice are solved by means of an explicit dynamic solver. This choice is due to the efficiency of the method when dealing with several thousands of degrees of freedom [96]. In fact, the assembly of the global stiffness matrix is not needed, and this dramatically reduces the amount of physical memory required to solve the problem.

The equilibrium equation:

$$\mathbf{M}\ddot{\mathbf{U}} + \mathbf{C}\dot{\mathbf{U}} + \mathbf{K}\mathbf{U} = \mathbf{R} \tag{3.43}$$

where **M**,**C** and **K** are the mass, damping and stiffness matrices respectively, **R** the externally applied loads vector, and **U** the displacement vector. The central difference scheme is a *direct integration* method, meaning that no transformation of the equation is performed before the system is solved, and among these methods it lies in the *explicit integration scheme* methods,

meaning that the solution at time $t + \Delta t$ is evaluated by the equilibrium conditions at time t.

This particular version of the finite difference method optimizes the approximation for the differential operator in the central node of the considered time interval, from which the name *central difference* method. With this assumption it is possible to evaluate the acceleration as an approximation of the displacement:

$$\ddot{\mathbf{U}}^{\mathbf{t}} = \frac{1}{\Delta t^2}(\mathbf{U}^{t-\Delta t} - 2\mathbf{U}^{t} + \mathbf{U}^{t+\Delta t}) \tag{3.44}$$

The error of the approximation is of order (Δt^2), so to have the same error in the velocity:

$$\dot{\mathbf{U}}^{\mathbf{t}} = \frac{1}{2\Delta t}(-\mathbf{U}^{t-\Delta t} + \mathbf{U}^{t+\Delta t}) \tag{3.45}$$

By substituting the obtained expression in Eq. 3.43 at time t:

$$\left(\frac{1}{\Delta t^2}\mathbf{M} + \frac{1}{2\Delta t}\mathbf{C}\right)\mathbf{U}^{t+\Delta t} = \mathbf{R}^{t} - \left(\mathbf{K} - \frac{2}{\Delta t}\mathbf{M}\right)\mathbf{U}^{t} - \left(\frac{1}{\Delta t^2}\mathbf{M} - \frac{1}{2\Delta t}\mathbf{C}\right)\mathbf{U}^{t-\Delta t} \tag{3.46}$$

This method is extremely efficient when a diagonalized (lumped) mass matrix $\mathbf{M}$ is considered and when velocity-dependent damping is neglected. Since no damping is used in the simulations (to avoid forcing the mechanical response) and the mass matrix is calculated as shown in 3.3.3 and diagonalized, it is a good choice for the solution of the equations of motions of the lattice. In fact, by imposing:

$$\hat{\mathbf{R}}^{t} = \mathbf{R}^{t} - \left(\mathbf{K} - \frac{2}{\Delta t^2}\mathbf{M}\right)\mathbf{U}^{t} - \left(\frac{1}{\Delta t^2}\mathbf{M}\right)\mathbf{U}^{t-\Delta t} \tag{3.47}$$

Eq. 3.46 simply reduces to:

$$\left(\frac{1}{\Delta t^2}\mathbf{M}\right)\mathbf{U}^{t+\Delta t} = \hat{\mathbf{R}}^{t} \tag{3.48}$$

This means that, if the mass matrix is diagonal, Eq. 3.48 does not need any factorization to be solved, leading to a system of scalar equations:

$$U_i^{t+\Delta t} = \hat{R}_i^t \left(\frac{\Delta t^2}{m_{ii}} \right) \tag{3.49}$$

where $i = 1, 2, \ldots, n_{dof}$ is the i-th degree of freedom and $m_{ii} > 0$ is the corresponding diagonal element.

Also, the $\mathbf{K}$ matrix in Eq. 3.47 does not need to be evaluated since:

$$\mathbf{K}\mathbf{U}^t = \sum_i \mathbf{K}^{(i)}\mathbf{U}^t = \sum_i \mathbf{F}^{(i),t} \tag{3.50}$$

where $\mathbf{F}$ is the internal forces vector, $x^{(i)}$ denotes quantities pertaining to the i-th element. This means that the $\hat{\mathbf{R}}^t$ term in Eq. 3.47 can be simply evaluated as:

$$\hat{\mathbf{R}}^t = \mathbf{R}^t - \sum_i \mathbf{F}^{(i),t} - \frac{1}{\Delta t^2}\mathbf{M}\left(\mathbf{U}^{t-\Delta t} - 2\mathbf{U}^t\right) \tag{3.51}$$

This means that the global stiffness matrix is not needed in order to solve the system of equations, and the solution is carried out on the element level, so that very large systems can be solved efficiently.

Stability Check

However, the effectiveness of the central difference integration relies on the efficiency of the single increment, since a very small time step is usually needed. The absence of iterations to achieve convergence, in fact, comes at the cost of the necessity to use a Δt smaller than a critical value Δt_{crit}. This value is evaluated as:

$$\Delta t \leq \Delta t_{crit} = \frac{2}{\omega_{max}} \tag{3.52}$$

where ω_{max} is the maximum frequency of the assemblage. Integration schemes that require the use of time step Δt smaller than a given critical

value are said to be *conditionally stable*. This means that the solution is stable only if the integration is carried out by selecting a proper Δt.

It can be shown [13] that $\omega_{max} < \max(\omega_I)$, where ω_I are the frequencies of the unrestrained items composing the system.

The stable time step is calculated by evaluating the natural frequencies of all the tetrahedrons in the Triangulation. The frequencies are evaluated by solving the eigenvalue problem:

$$\det\left(\mathbf{K} - \omega^2\mathbf{M}\right) = 0 \tag{3.53}$$

where $\mathbf{K}$ and $\mathbf{M}$ are the stiffness and mass matrix of the tetrahedron, respectively. The stiffness matrix is evaluated by assembling the contributions of the 12 facets (see Table 3.2):

$$\mathbf{K} = \sum_{f=1}^{12} \mathbf{K}^{(f)} = \sum_{f=1}^{12} \begin{bmatrix} \mathbf{K}_{ii}^{(f)} & \mathbf{K}_{ij}^{(f)} \\ \mathbf{K}_{ji}^{(f)} & \mathbf{K}_{jj}^{(f)} \end{bmatrix} \tag{3.54}$$

where $\sum$ is used to identify the assemblage operation, i and j are the two nodes associated with the current facet. The different terms $\mathbf{K}^{(f)}$ are evaluated as:

$$\mathbf{K}^{(f)} = \mathbf{B}^{(f)\intercal}\mathbf{C}_e\mathbf{B}^{(f)} \tag{3.55}$$

where the compliance matrix:

$$\mathbf{C}_e = \begin{bmatrix} E_0 & 0 & 0 \\ 0 & \alpha\, E_0 & 0 \\ 0 & 0 & \alpha\, E_0 \end{bmatrix} \tag{3.56}$$

Similarly to the stiffness matrix, the mass matrix $\mathbf{M}$ is evaluated by summing the different facets contributions:

$$\mathbf{M} = \sum_{f=1}^{12} \mathbf{M}^{(f)} = \sum_{f=1}^{12} \begin{bmatrix} \mathbf{M}_i^{(f)} & 0 \\ 0 & \mathbf{K}_j^{(f)} \end{bmatrix} \tag{3.57}$$

where the different terms $\mathbf{M}^{(f)}$ are calculated as:

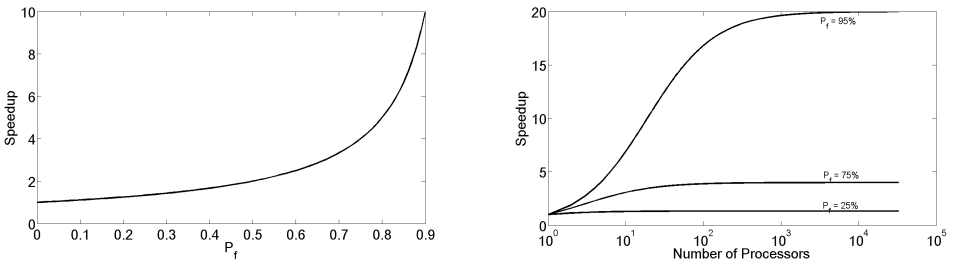

Figure 3.21: Theoretical and effective computation speedup

$$\mathbf{M}^{(f)} = \rho \begin{bmatrix} V_f & 0 & 0 & 0 & I_f^z & I_f^y \\ 0 & V_f & 0 & -I_f^z & 0 & I_f^x \\ 0 & 0 & V_f & I_f^y & -I_f^x & 0 \\ 0 & -I_f^z & I_f^y & L_f^y + L_f^z & -L_f^{xy} & -L_f^{xz} \\ I_f^z & 0 & -I_f^x & -L_f^{xy} & L_f^x + L_f^z & -L_f^{yz} \\ -I_f^y & I_f^x & 0 & -L_f^{xz} & -L_f^{yz} & L_f^x + L_f^y \end{bmatrix} \tag{3.58}$$

where ρ is the material volume mass, I and L represent the first and second order moments of the volume V. The diagonalized mass is simply obtained by discarding the terms out of the diagonal.

3.3.4 Parallel Computing

The explicit integration scheme adopted is not only advantageous because it is not necessary to build the global stiffness matrix (consequently lowering the physical memory requirements), but also because the diagonalized system is easily parallelized to speed the calculations up.

The scalar equations needed to solve the problem, in fact, can be evaluated simultaneously by different processors, and the global solution can be assembled at a second time.

Amdahl's Law [69] states that the potential program speedup is defined by the fraction of code P_f that can be parallelized:

$$\text{speedup} = \frac{1}{1 - F} \tag{3.59}$$

meaning that the theoretical total speedup is zero if there is no parallelized code, and infinite if the whole code is parallelized. By introducing the actual number of available processor in the equation:

$$\text{speedup} = \frac{1}{\frac{P_f}{N_c} + S_f} \tag{3.60}$$

it is possible to estimate the effective speedup obtained. As shown in Fig. 3.21, high percentage of parallelized code together with a big number of processors is needed to speedup the calculations consistently.

The central difference integration scheme used, together with the adoption of the parallel computing tools, allowed to run all the simulations reported in this work on a quad-core i7 personal computer within reasonable time. The percentage of parallelized code is $\approx 50\%$, and the estimate on the speedup by using Eq. 3.60 is of about 1.88. By performing the same simulation on a 50mm cube sample with and without parallelizing the calculations, a value of ≈ 1.65 has been estimated.

3.4 Spring Network Model

The *spring network* model will be discussed in the next Sections. This model is obtained as a simplification of the fully dynamic model discussed in the previous section. The interaction among adjacent cells is only composed of normal forces. This approach was used in the first models proposed in literature [133]. The proposed model exploits the full model characteristics, trying to reproduce its results by a simplified approach. The motion of the cells is still expressed by rigid body motions (see Sec. 3.3.1), while the normal strain component is still evaluated on the geometric center of the area of the connection, as the displacement jump smeared over the length of the element. The constitutive law in tension exhibits history-dependent strain softening, while the compressive response is elastic-perfectly plastic for positive volumetric states and hardening for negative ones. Shearing effects are indirectly taken into account by means of a dependence of the

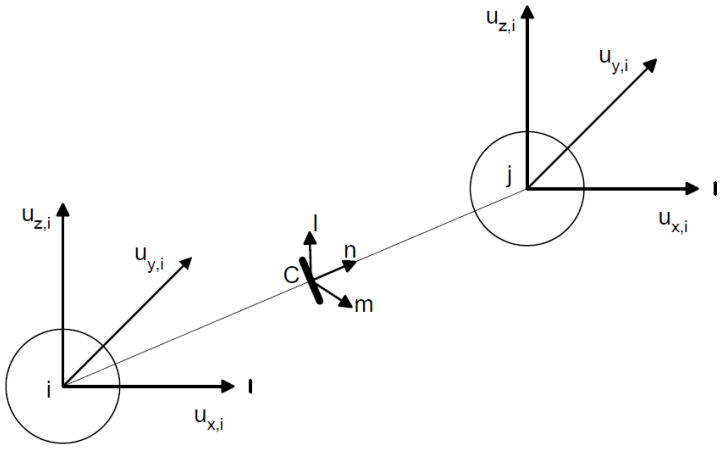

Figure 3.22: Particles degrees of freedom and connection local axes for the spring network model

axial strength on the relative transversal displacement experienced by the center of the connection. The system of equations is solved by means of a static integrator.

3.4.1 Kinematics

The kinematics of the cells is still defined by rigid body motion (see Eqs. 3.19 to 3.22). The difference lies in the fact that only normal stresses and strain are computed at the center of the connection (see Fig. 3.22). The strain in every connection is then a scalar quantity:

$$\epsilon = \frac{\mathbf{n}_f^T[|\mathbf{u}_c|]}{l^e} \tag{3.61}$$

so that the compatibility condition:

$$\epsilon = \left[\epsilon_N\right] = \mathbf{B}^{(e)}\mathbf{U}^{(e)} \tag{3.62}$$

can be written in the same form as in the case of the full model. The strain vector is now a scalar quantity so that the compatibility matrix reduces to the form:

$$\mathbf{B}^{(e)} = \frac{1}{l^e}\begin{bmatrix} -\mathbf{n}^T\mathbf{A}_1 & \mathbf{n}^T\mathbf{A}_2 \end{bmatrix} \tag{3.63}$$

3.4.2 Constitutive Law

The constitutive law used in the spring model is derived by the complete constitutive model. Since adjacent cells only share normal forces, the frictional and volumetric effects must be taken into account indirectly. The elastic, fracturing and frictional behavior of the so built lattice will be discussed.

The elastic behavior of the lattice follows the rule:

$$\sigma_N = E_0 \epsilon_N \tag{3.64}$$

The macroscopic properties can be evaluated using the same procedure used for the full model, by imposing $\alpha = 0$, so that:

$$\begin{aligned} E &= \frac{1}{2}E_0 \\ \nu &= \frac{1}{4} \end{aligned} \tag{3.65}$$

Eq. 3.65 shows how in the spring network model the value of the macroscopic Young's modulus obtained from the lattice simulation is equal to 50% of the mesoscale one, while the Poisson's ratio value is bound to be equal to 0.25, which is close to the usual values obtained in lab tests. It is worth noticing that the incapability of axial spring network to reproduce a chosen macroscopic Poisson's effect is in accordance with findings from different authors who studied Voigt's molecular models in elasticity [126] [29].

The fracturing behavior due to tensile stresses is supposed to be following the same exponential rule used in the full model:

$$\sigma_b = \sigma_0 \, e^{-\frac{H}{\sigma_0}(<\epsilon_1 - \epsilon_0>)} \tag{3.66}$$

Similarly to the full model, in the spring model the compressive behavior is dependent on the average volumetric deformation of the contact area:

$$\epsilon_v = \sum_{i=1}^{n_f} \epsilon_{v,i} \frac{A_{f,i}}{A_t} \tag{3.67}$$

so that the evolution of the stress boundary in compression is given by:

$$\sigma_b = \begin{cases} \sigma_c & \text{if} \epsilon_v \geqslant 0 \\ \sigma_c e^{\frac{H}{\sigma_c}(-\epsilon_v - \epsilon_c)} & \text{if} \epsilon_v < 0 \end{cases} \tag{3.68}$$

The dependence of the hardening modulus on the volumetric deformation follows the rule:

$$H = H_c/(1 + k_2 < r_{dv} - k_1 >) \tag{3.69}$$

where r_{dv} is the deviatoric to volumetric strain ratio, and k_1,k_2 are two material parameters.

Differently from the full model, the spring network model is suitable for the static integration of the equation of motion, since the number of degrees of freedom are one half of the previously defined approach (i.e. rotations are neglected). To this end, the stiffness matrix of the whole system must be assembled and updated during the analysis. The initial tangent stiffness is built as:

$$\mathbf{K}_0 = \sum_{i=1}^{n_{el}} \mathbf{K}_{i,0}^{(e)} \tag{3.70}$$

where n_{el} is the number of elements in the mesh, and the element stiffness matrix:

$$\mathbf{K}_0^{(e)} = \mathbf{B}^{(e)T} C_e \mathbf{B}^{(e)} \tag{3.71}$$

where the compliance matrix C_e is equal to the scalar value of the normal Young's modulus.

The nonlinear behavior is handled through a Newton-Raphson [112] method. The secant stiffness global matrix is evaluated ad the beginning of every step; this choice is due to the fact that the secant matrix always non-negative and this method has proven to be effective in handling strain softening behavior.

The secant stiffness matrix of every element at time $t = i$ is simply evaluated as:

$$\mathbf{K}_{t=i}^{(e)} = D\mathbf{K}_0^{(e)} \tag{3.72}$$

where D is the damage parameter, simply defined as the ratio between the current value of the secant Young's modulus and the initial one:

$$D = \frac{E_s}{E_0} \tag{3.73}$$

3.4.3 Displacement Control Strategy

The chosen model is integrated statically. The solving system of equations:

$$\mathbf{KU} = \mathbf{R} \tag{3.74}$$

is solved by inverting the secant stiffness matrix $\mathbf{K}$. To correctly capture the softening behavior of concrete, lab tests are conducted under displacement control. To this end, the presented simulations will

The degrees of freedom of the system are divided into free (denoted by subscript 1) and prescribed displacement (subscript 2), so that the system of equation can be written as follows [77]:

$$\begin{bmatrix} \mathbf{K}_{11}\mathbf{K}_{12} \\ \mathbf{K}_{21}\mathbf{K}_{22} \end{bmatrix} \begin{bmatrix} \mathbf{U}_1 \\ \mathbf{U}_2 \end{bmatrix} = \begin{bmatrix} \mathbf{R}_1 \\ \mathbf{R}_2 \end{bmatrix} \tag{3.75}$$

From the first row:

$$\mathbf{K}_{11}\mathbf{U}_1 + \mathbf{K}_{12}\mathbf{U}_2 = \mathbf{R}_1 \tag{3.76}$$

Since the prescribed displacement field $\mathbf{U}_2$ is known in advance, one can write for the i-th time step:

$$\mathbf{K}_{11}\mathbf{U}_1 = \mathbf{R}_1 - \mathbf{K}_{12}\mathbf{U}_2 \tag{3.77}$$

At the beginning of any step, the stiffness matrix is updated, the prescribed displacement vector $\mathbf{U}_2$ is constructed so that the the forces $\mathbf{F}_{12} = \mathbf{K}_{12}\mathbf{U}_2$, which represent the forces arising in the free degrees of freedom due to the displacement imposed on the prescribed ones. The displacement field of the free nodes is then evaluated as:

$$\mathbf{U}_1 = \mathbf{K}_{11}^{-1}\left(\mathbf{R}_1 - \mathbf{K}_{12}\mathbf{U}_2\right) \tag{3.78}$$

The so evaluated $\mathbf{U}_1$ does not generally satisfy static equilibrium, so that the Newton-Raphson iterations are performed by re-applying the out of balance forces $P = R - F$ on the free degrees of freedom to evaluate the displacement correction:

$$\delta\mathbf{U}_1 = \mathbf{K}_{11}^{-1}\left(\mathbf{P}_1\right) \tag{3.79}$$

Eq. 3.79 is solved until the convergence criterion is satisfied.

Tolerance Check

Static integration methods require that a tolerance check is performed to establish when convergence has been achieved during iterations. The basic idea is that a certain measure r, dependent on the evaluated response of the system, is checked against a threshold value e, defined as the tolerance level. Different measures can be used to assess the distance between the calculated solution and the correct one. The different possibilities involve:

1. Norm of the unbalanced forces

$$r = ||\mathbf{P}_1|| \tag{3.80}$$

2. Norm of the displacement increment

$$r = ||\delta\mathbf{U}_1|| \tag{3.81}$$

3. Norm of the energy increment

$$r = \delta\mathbf{U}_1\mathbf{P}_1 \tag{3.82}$$

At the end of every step, the integrator checks if $r < e$, in which case the result of the current step is stored and the system advances to next step; otherwise a new iteration is performed.

3.5 Post-Processing and Crack Opening Calculations

The post-processing of the results is performed by means of ParaView [3], an open source software specifically built for large data structures visualization. It allows for the definition of bi- and tri-dimensional shapes, the representation of scalar and vectorial quantities (e.g. stress, strain, crack openings, displacement) over time together with the possibility to plot measures over zones or points of the mesh. All the post-processing capabilities of the software are handled by means of "Filters", which are basic operations that can be performed on the visualized entities [68].

Fig. 3.23 shows two possible choices for the visualization of the particle lattice model: (a) the "particle" view, (b) the "facet" view. In the first, the spherical-shaped aggregate pieces are rendered according to their diameter distribution. In the latter, every facet obtained from the Modified Voronoi Tessellation is represented, so that all the rigid cells can be visualized and

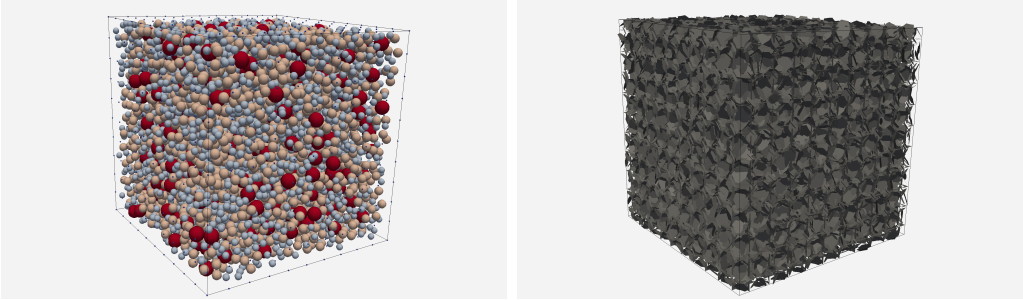

Figure 3.23: *Particle* and *Facet* view of a 150mm cube

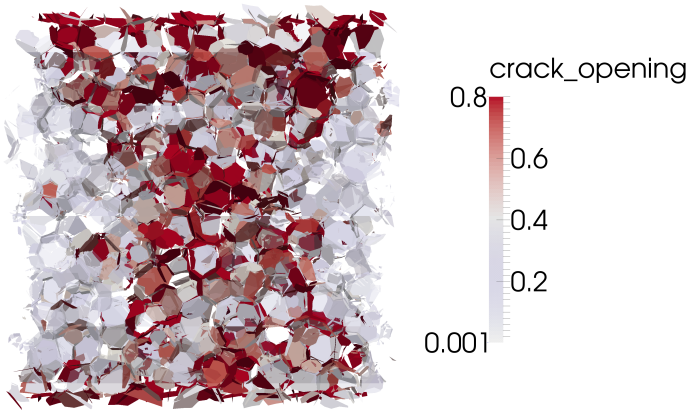

Figure 3.24: Post-Processing representation of the crack openings for a uniaxial compression test performed on a 150mm cube

the mechanical relevant quantities (i.e. stresses and strains) fields can be plotted over the triangular facets.

By applying the "Displacement" filter it is also possible to plot the deformed shape and to follow the displacement history during the simulation by loading the results of the different time steps.

3.5.1 Crack Openings Representation

One unique feature of the random particle lattice model is the explicit representation of crack openings in-between two adjacent cells. As already described, the random placement of the particles creates randomly shaped

rigid cells, the separation between them deriving from tensile and shear deformation can represent tortuous crack paths.

The representation of the crack patterns is then performed on the "facet" view of the model. The crack opening w is calculated as:

$$w = \begin{cases} \sqrt{(w_n^2 + w_l^2 + w_m^2)} & \text{if } \sigma_n > 0 \\ 0 & \text{otherwise} \end{cases} \tag{3.83}$$

with

$$w_i = l(\epsilon_i - \sigma_i / E_i), \qquad i = n, l, m \tag{3.84}$$

Fig. 3.24 shows the numerically evaluated crack openings for a 100 mm cube under uniaxial compression, showing the typical hourglass shape. The results of the simulation will be discussed in detail in Sec. 5.

Chapter 4

Experimental Tests

4.1 Definition of the Campaign

This Chapter will present the multiscale experimental campaign performed on different types of concrete specimens. The basic idea is that, by characterizing the mechanical properties of concrete at mesoscale, it is possible to predict its macroscopic behavior by means of the here proposed lattice particle modeling approach. This approach is particularly advantageous because the dimensions of the specimens can be kept small and the testing procedures can be easily standardized and reproduced without the need of expensive testing systems.

To this end, a *mesoscale concrete* has been cast in cylindrical elements with the dimensions of the typical struts in the lattice (see Sec. 4.2.1) and tested in tension, shear and compression. The so obtained information have been used in the definition of the lattice elements, and the proposed model has been checked against the results obtained on the macroscale lab tests, performed on concrete elements of the usual dimensions used in experiments, cast to have a correspondence with the mesoscale specimens in terms of granulometric composition and materials used.

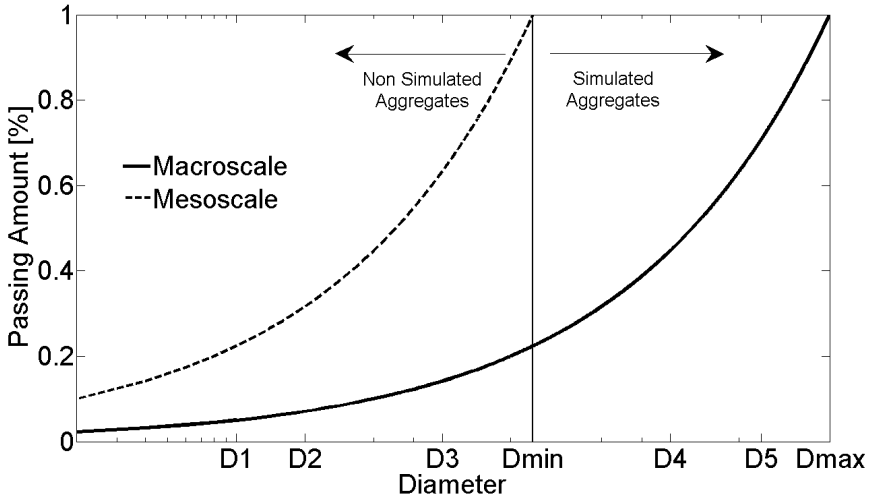

Figure 4.1: Multiscale granulometric curves used in the experiments

4.2 Multiscale Experimental Tests

The proposed lattice particle model explicitly takes into account the mechanical behavior and spatial arrangement of the coarse aggregate inclusions. The aggregate mechanical behavior is defined as indefinitely elastic, so that the location of possible damage is the bulk paste composed of cement and the smaller aggregate fraction. As already discussed in Chapter 3, based on the chosen value of D_{min}, the constitutive law parameters need to be scaled since the non-modeled aggregate fraction will modify the mechanical behavior.

In most of the simulation proposed in this work (see Chapter 5) the minimum diameter D_{min} has been set equal to 4.75 mm, which is generally considered as the threshold between the coarse and the fine aggregate. This allows to obtain high inclusion volume fractions (at least 30% in all the numerical investigations) while keeping the computational cost reasonable.

The "mesoscale" concrete has so been cast by using aggregate size $D \leq 4.75$ mm (see Fig. 4.1), and it has been tested in shear, tension and compression to evaluate the principal mechanical properties. A "macroscale" set of tests on regular concrete specimens of the usual sizes commonly used in lab tests has been carried out. Results of both campaigns are reported in

Figure 4.2: Mesoscale specimens casting and dimensions

the next Sections.

4.2.1 Mesoscale Tests

The first step in the definition of the campaign involved the evaluation of the characteristic dimensions of the mesoscale concrete to be used. Numerical investigations performed on a set of 10 concrete cubes ($l = 150\,mm$) showed that a diameter equal to 20 mm can be chosen for the mesoscale specimens, since the so obtained value of the cross sectional area is representative of the mean obtained by the model. Cylindrical shape with aspect ratio $2:1$ has been used to simplify the test procedure.

Different set of tests have been performed: tensile and compressive uniaxial tests were conducted by means of a Universal Testing Machine, while a shear box has been used to evaluate the shear response of the specimens. The results of such investigations are reported in the next sections.

Figure 4.3: Tensile tests setup and typical failure mode

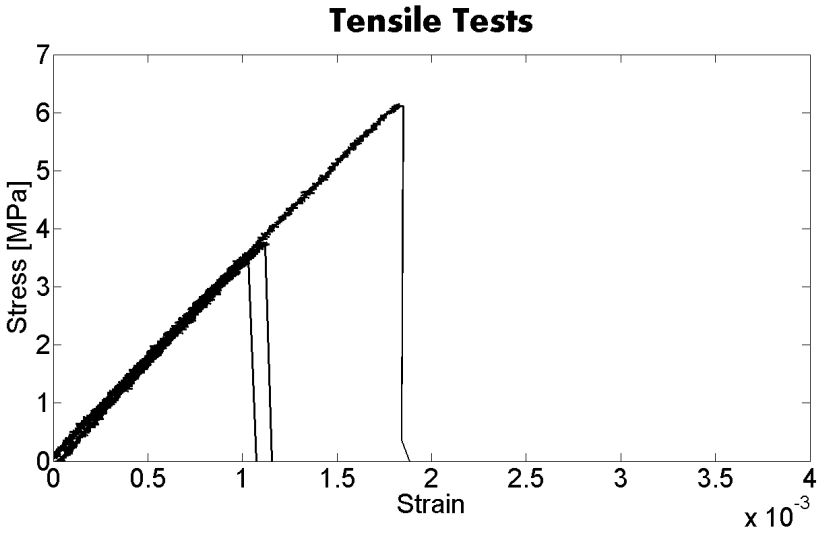

Figure 4.4: Tensile tests results

Tensile Tests

Fig. 4.3 shows the experimental setup used to perform the tensile tests. Epoxy resin was used to glue the specimens to the metal supports, which were then attached to a Universal Testing Machine.

Due to the high flexibility of the testing system (shown in Fig. 4.3), the tests were unable to retrieve the softening branch, so the results were used to evaluate the tensile strength of the mesoscale concrete only. The stress-strain curves obtained are reported in Fig. 4.4.

Shear Tests

Fig. 4.3 shows the experimental setup used to perform the shear tests. Direct shear was applied to the specimens by means of a shear box commonly used in geotechnical lab tests. Metal supports were produced in order to accommodate the mesoscale concrete specimens in the box, and rollers were used to avoid any friction between such supports.

The machine used to perform the tests is composed of a mechanical engine, and due to the fact that geotechnical tests usually require very low test speeds, it has been able to capture the post-peak behavior by imposing an adequately low strain rate.

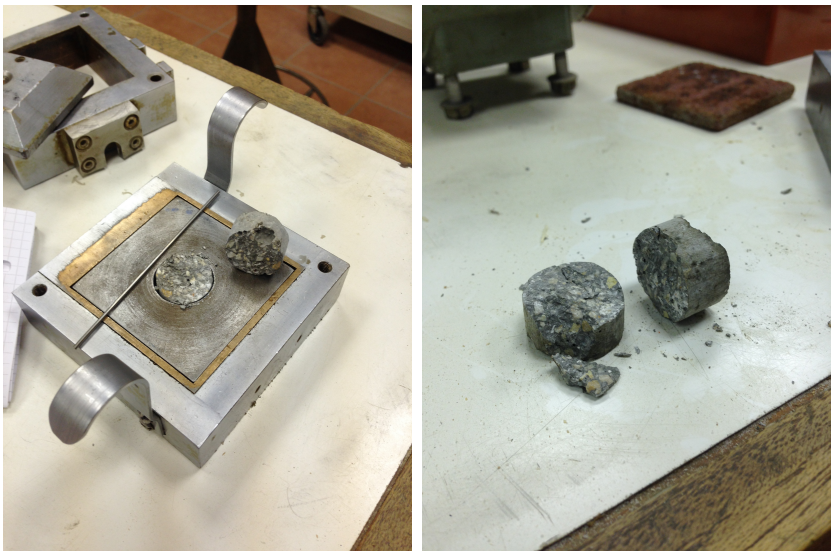

Figure 4.5: Shear tests setup and typical failure mode

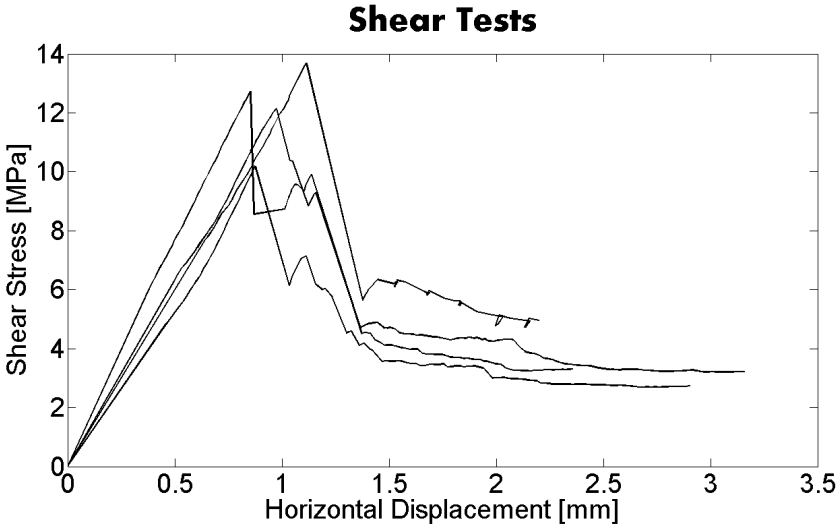

Figure 4.6: Shear tests results

Figure 4.7: Compressive tests setup and typical failure mode

Compressive Tests

Fig. 4.7 shows the experimental setup used to perform the compressive tests. Both monotonic and cyclic tests were performed, and the results are shown in Fig. 4.8.

4.2.2 Macroscale Tests

The mesoscale tests were followed by a *macroscale campaign*, which involved the testing of concrete elements of various shape and dimensions (i.e. cylinders, cubes, prisms). The size of the elements, together with the

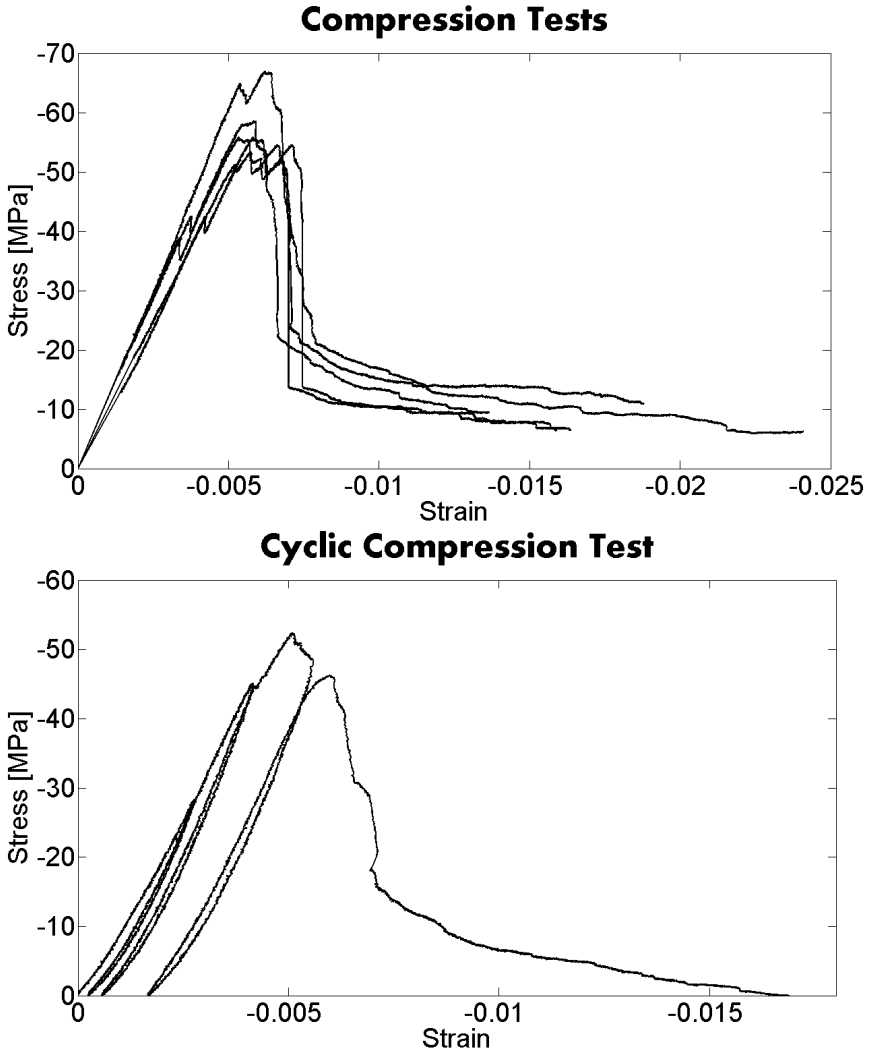

Figure 4.8: Compressive tests results

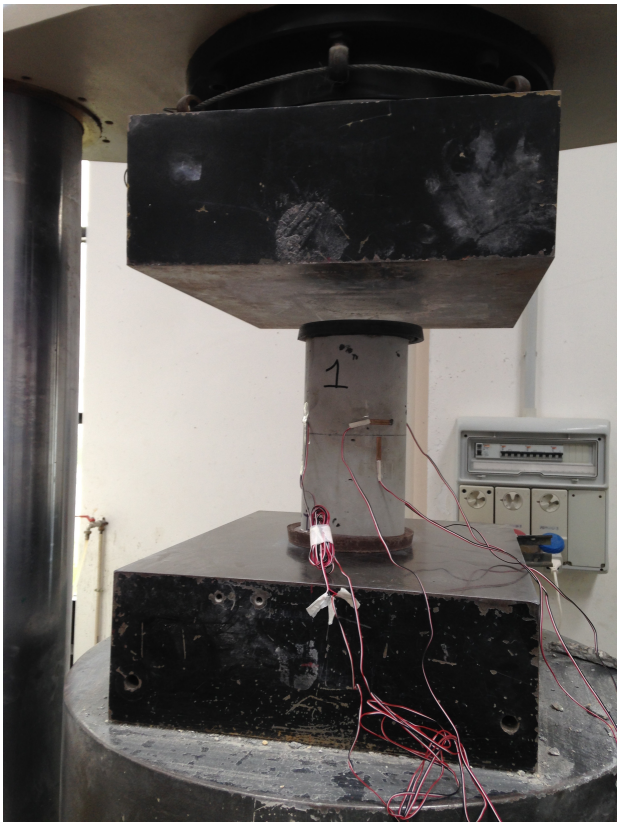

Figure 4.9: Macroscopic compressive tests setup for cylindrical specimens

aggregate dimensions, reflect the commonly used ones in test labs. The tests were performed in the University of Salerno.

Different sets of uniaxial compression tests were conducted by means of a Universal Testing Machine of capacity 500 kN. The results of such simulations are reported in the following sections.

Uniaxial Compression on Cylindrical Specimens

A set of 3 cylindrical specimens has been tested under uniaxial compression. Strain gages were attached as reported in Fig. 4.9. The testing speed was set equal to 0.1 mm/min. The results of the simulations in terms of stress-strain response are reported in Fig. 4.10, while the observed failure modes, which exhibit the typical shear band propagation, are shown in Fig. 4.11.

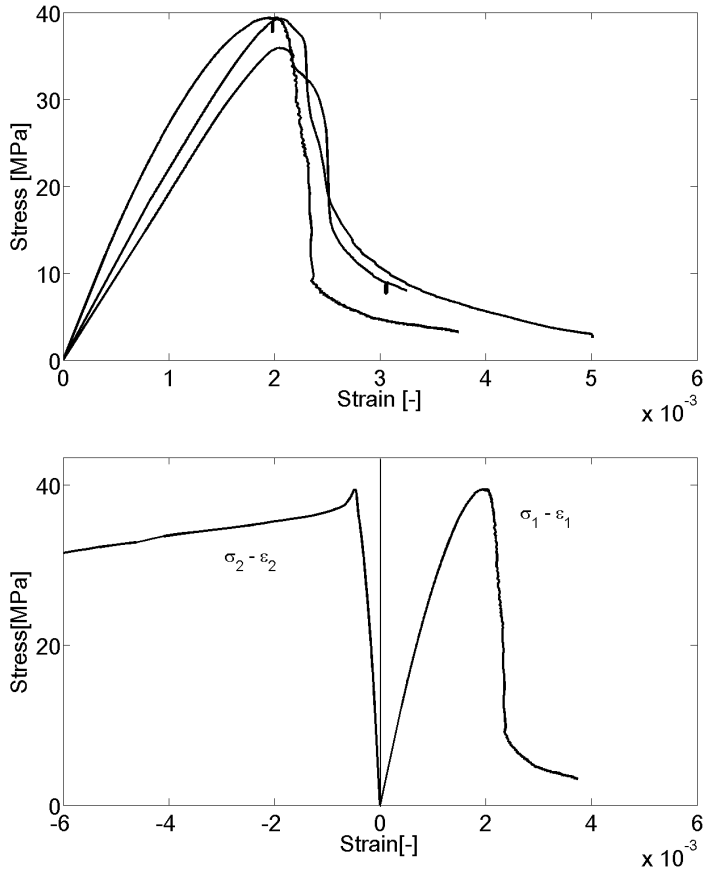

Figure 4.10: Stress-strain curves obtained on cylindrical specimens. Top: collection of all the axial response. Bottom: axial and lateral stress-strain response for specimen 1.

Figure 4.11: Failure modes observed on cylindrical specimens

Figure 4.12: Macroscopic compressive tests setup for cubical specimens

Uniaxial Compression on Cubical Specimens

A set of 6 cubical specimens has been tested under uniaxial compression. The test setup and arrangement of the strain gages are shown in Fig. 4.12. The testing speed was set equal to 0.1 mm/min. The results of the simulations in terms of stress-strain response are shown in Fig. 4.13, while the observed failure modes are reported in Fig. 4.14.

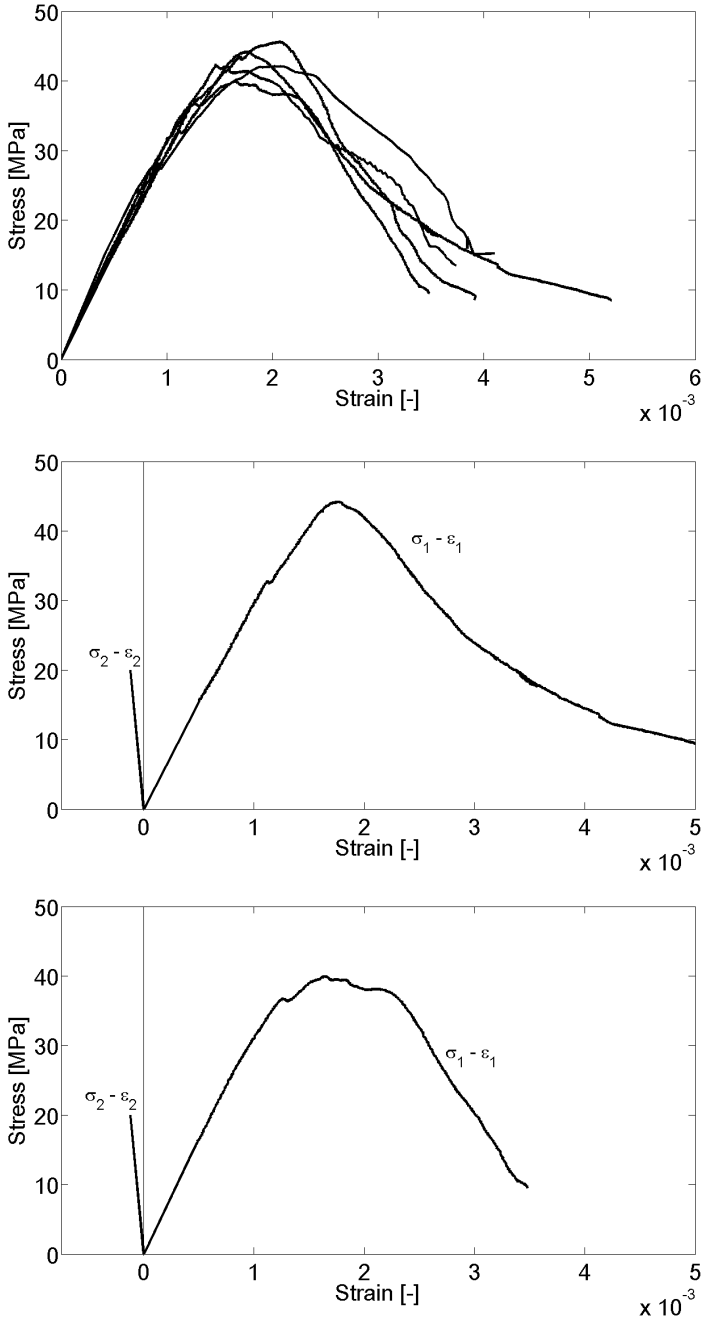

Figure 4.13: Stress-strain curves obtained on cubical specimens. Top: collection of all the axial response. Bottom: axial and lateral stress-strain response for specimens 4 and 5.

Figure 4.14: Failure modes observed on cubical specimens

Chapter 5

Numerical Results

5.1 Fully Dynamic Model

The results of the simulations performed on the fully dynamic model are reported in the next sections. Different lab tests have been modeled, including the ones performed in the experimental campaign presented in Chapter 4. The different cases analyzed involve: (1) uniaxial compression on cubical and cylindrical specimens, with a focus on the damage localization in compression, (2) biaxial compression, (3) fracturing behavior.

5.1.1 Uniaxial Compression

Uniaxial compressive failure of concrete has been deeply investigated in various works available in literature [129] [128] [86] [85]. Several variables influence the overall response of the material, such as: size and aspect ratio of the specimen, boundary conditions and granulometric composition. In order to correctly predict what type of failure occurs in the different cases, a model must be able to capture the evolution of damage throughout the member, describing the mechanical interaction between parts of the element properly.

The herein presented random lattice particle model proved itself capable of predicting the correct failure typology for different cases. In the following

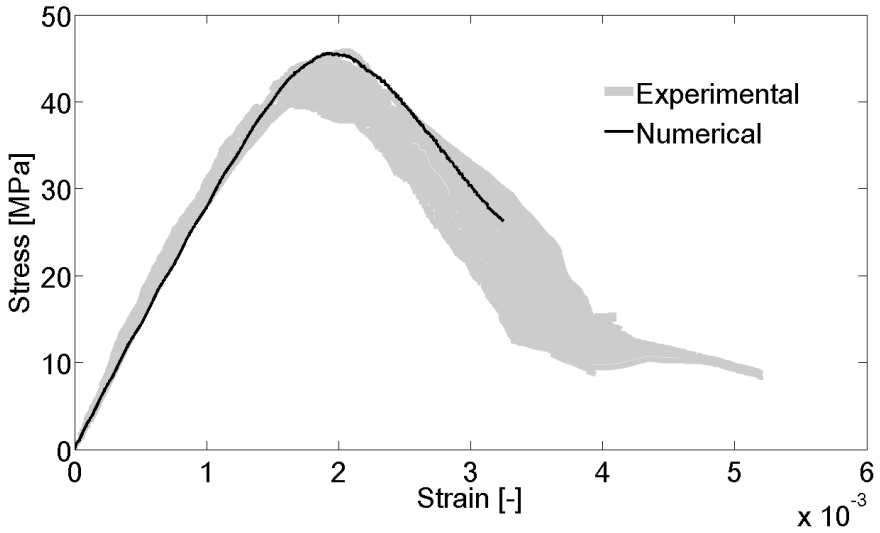

Figure 5.1: Cubical specimens: numerical vs experimental stress-strain curves

sections the comparison between the experimental and numerical response of various uniaxial tests is presented, both in terms of stress-strain response and observed crack pattern at failure.

Cubical Specimens

The comparison between the experimental and the numerical simulation of the uniaxial compression test performed is presented in this section. Since the experimental tests were conducted as a part of the multiscale experimental campaign presented in Chapter 4, in the numerical model the values of the measured relevant quantities were used. A full recap of all the mechanical quantities (i.e. the ones measured in the meso and macroscopic tests, the ones used in the model and those evaluated from the numerical results) is given in Table 5.1, which shows the correspondence between the mesoscopical values measured in the test, the ones used in the lattice particle model and the macroscopical quantities, both the ones measured in the lab tests and the numerically simulated ones.

The comparison between experimental and numerical response shows how the model is capable of predicting both the stress-strain curve (see Fig. 5.1) and the crack pattern observed in the tests. Fig. 5.2 shows how the numerical

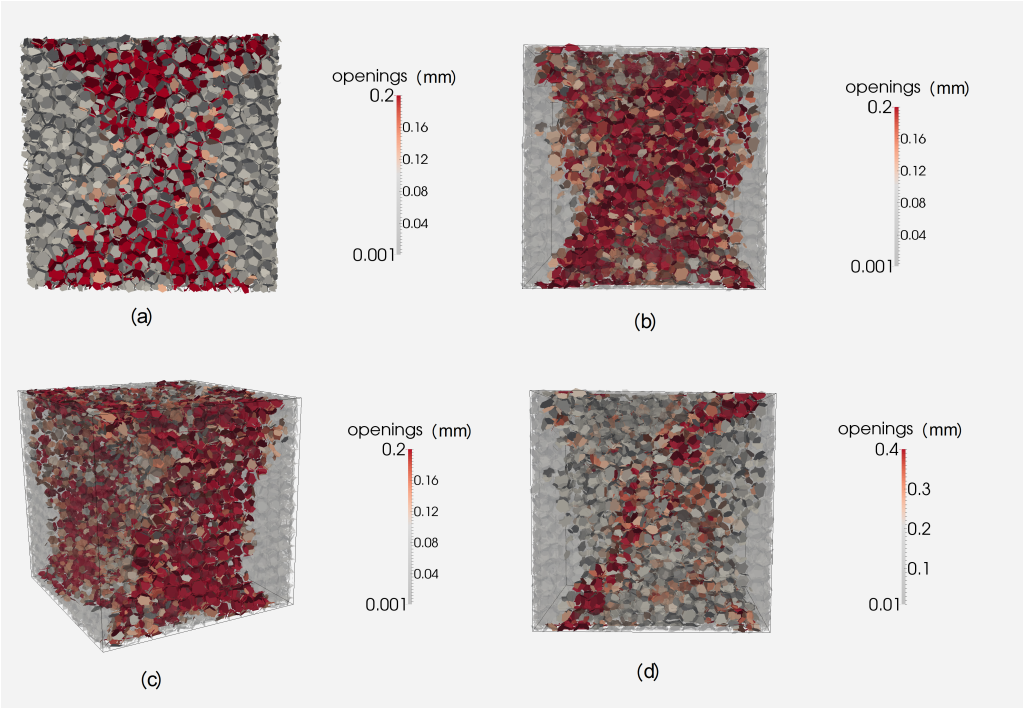

Figure 5.2: Numerical crack paths at failure for the cubical specimen under uniaxial compression: (a) section view; (b) face 1; (c) 3-d view; (d) face 2

Figure 5.3: Comparison between experimental and numerical crack pattern at failure

Table 5.1: Comparison between mesoscopical parameters measured, used and macroscopical quantities measured on the cubical specimens. For the experimentally evaluated quantities, the minimum and maximum measured values are reported

Quantity	Mesoscopical measured value	Mesoscopical used value	Macroscopical measured value	Macroscopical evaluated value
Compressive Strength	52-68 MPa	60 MPa	40-45 MPa	44 MPa
Young's Modulus	42000-45000 MPa	46500MPa	29800-30500MPa	30088 Mpa
Poisson's Ratio	-*	-*	0.178	0.18
Tensile Strength	3.5-6 MPa	4.5 MPa	-	-
Shear Strength	10-13.5 MPa	13.5MPa	-	-

* values of the Poisson's Ratio were not measured during mesoscale tests. Its value is not a parameter of the model, α is used instead according to Eq. 3.26

simulation correctly reproduces the typical "hourglass" shape of the high friction uniaxial compressive tests, together with a macroscopic shear band that spreads from the top to the bottom of the specimen. Such crack was also observed in the experimental tests, as clearly shown by Fig. 5.3.

Cylindrical Specimens

The comparison between the experimental and the numerical simulation of the uniaxial compression test is presented in this section. Since the experimental tests were conducted as a part of the multiscale experimental campaign presented in Chapter 4, in the numerical model the values of the measured mesoscale mechanical properties were used. The macroscopic

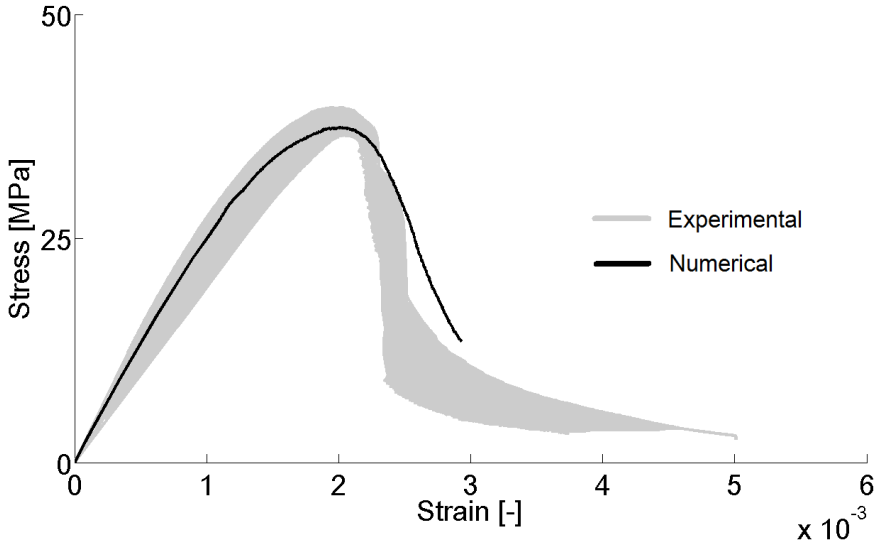

Figure 5.4: Cylindrical specimens: numerical vs experimental stress-strain curves

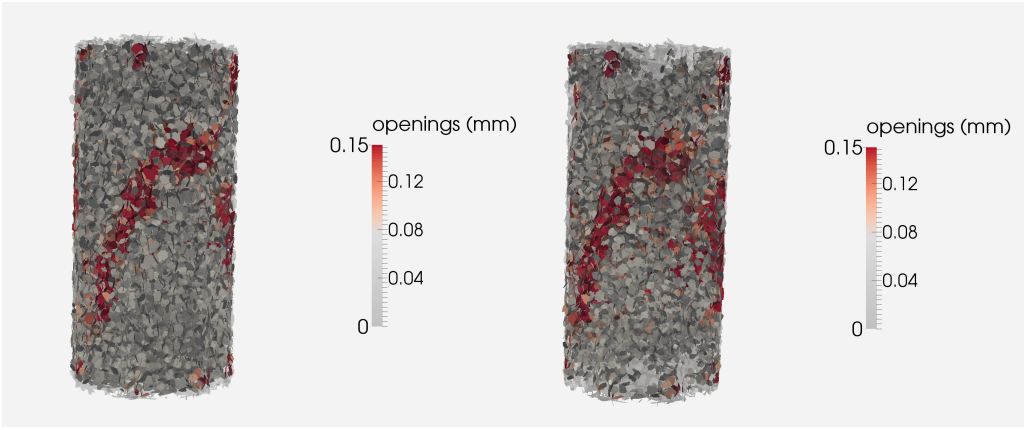

Figure 5.5: Numerical crack paths at failure for the cylindrical specimen under uniaxial compression: different views

Table 5.2: Comparison between mesoscopical parameters measured, used and macroscopical quantities measured on the cylindrical specimens. For the experimentally evaluated quantities, the minimum and maximum measured values are reported

Quantity	Mesoscopical measured value	Mesoscopical used value	Macroscopical measured value	Macroscopical evaluated value
Compressive Strength	52 68 MPa	60 MPa	36-41 MPa	37.5 MPa
Young's Modulus	42000-45000 MPa	46500MPa	29800-30500MPa	30088 Mpa
Poisson's Ratio	-*	-*	0.2	0.18
Tensile Strength	3.5-6 MPa	4.5 MPa	-	-
Shear Strength	10-13.5 MPa	13.5MPa	-	-

* values of the Poisson's Ratio were not measured during mesoscale tests. Its value is not a parameter of the model, α is used instead according to Eq. 3.26

Figure 5.6: Comparison between experimental and numerical crack pattern at failure

response of cylinders were then numerically evaluated and compared to those obtained in the lab tests.

The comparison between the experimental and numerical response shows how the model is capable of predicting both the macroscopic stress-strain response (see Fig. 5.4) and the crack pattern at failure. Fig. 5.5 shows how the model is able to localize the damage in a big shear band which runs at an angle of approximately $\pi/4$. The direct comparison with the observed failure mode is given in Fig. 5.6.

The model also proved capable of predicting the stress-strain response of such elements. A full recap of all the mechanical quantities used in the model and the corresponding (measured) macroscopic ones is given in Table 5.2.

Influence of the Aspect Ratio and Localization of Damage in Compression

Different studies in literature investigated the influence of the aspect ratio on the compressive response of concrete [88] [129] [130] [75]. Experimental evidences show that failure under uniaxial compression is caused by shear macrocracks that form due to the applied load. Also, the height of the

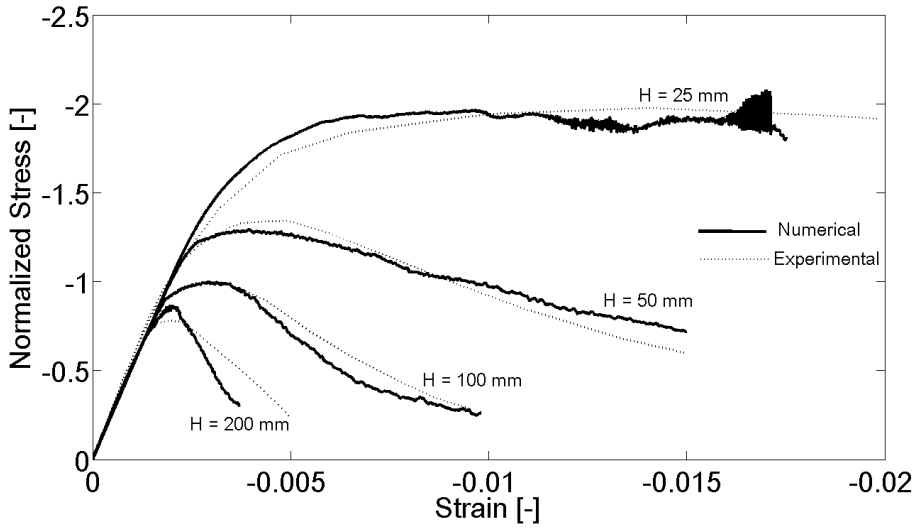

Figure 5.7: Numerical and experimental normalized stress-strain curves for prisms of different heights

specimen plays an important role in both the peak load and the post-peak softening behavior: taller elements, in fact, exhibit lower strength values and a more brittle failure. This is caused by the localization of damage: taller specimen undergo damage in a zone that is relatively smaller compared to shorter ones, leading to lower strength and ductility. Following the study from Van Mier and coworkers [129], a set of prisms with different aspect ratio has been modeled and tested under uniaxial compression.

The parameters used in the numerical simulations were evaluated based on the information given on the paper by the authors, by fitting the response for the specimen with aspect ratio equal to 1 (see Table 5.3). By keeping the evaluated set of parameters constant, all the other tests were then simulated. The numerical results show good agreement with the experimental ones. Fig. 5.7 shows the difference in terms of normalized stress versus strain. while Fig. 5.8 shows the different failure modes obtained. The numerical tests show that the localization of damage creates more distributed crack patterns for the shorter specimens and localized failure in taller one. Also, the post-peak curve tends to become more brittle as the height increases. Both aspects are correctly captured by the model.

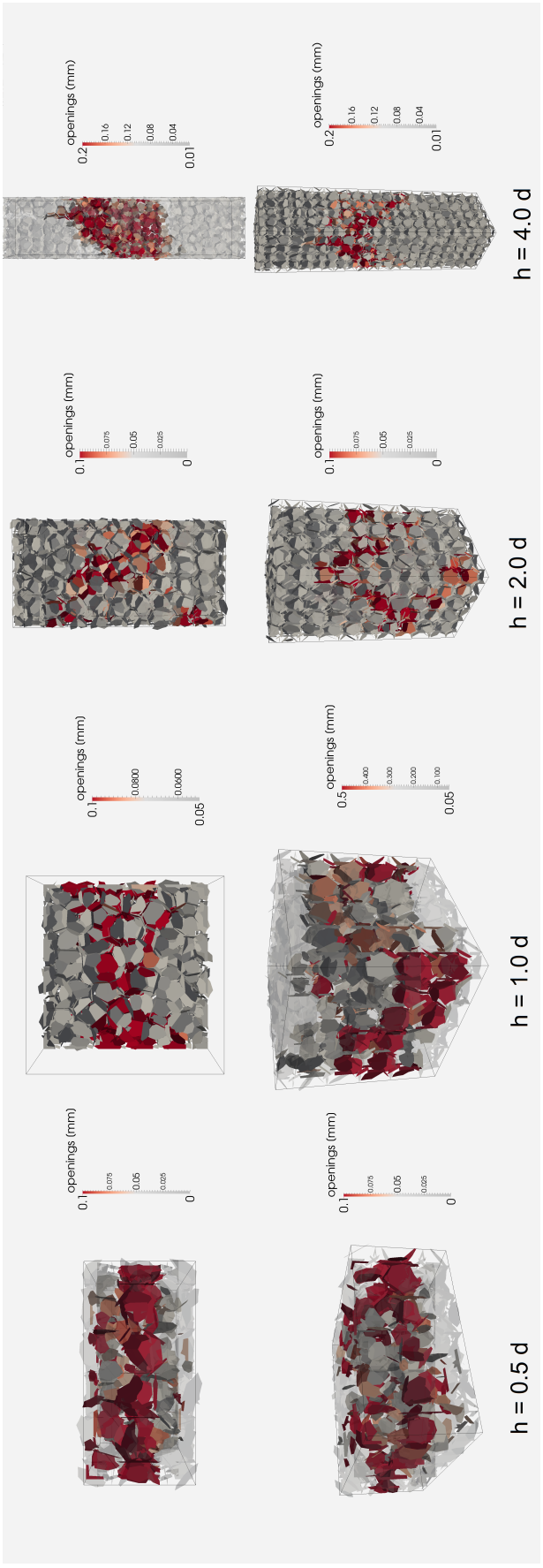

Figure 5.8: Failure modes of prisms with different heights under uniaxial compression

Table 5.3: Values of the mechanical properties used in the simulations for the tests performed by Van Mier et al. [129]

σ_t (MPa)	5	$G_s(N/mm)$	0.16
σ_c (MPa)	90	K_c	13750
σ_s (MPa)	11	k_{c1}	1
E (MPa)	55000	k_{c2}	5
α	0.25	n_t	3
G_t (N/mm)	0.04	n_c	1

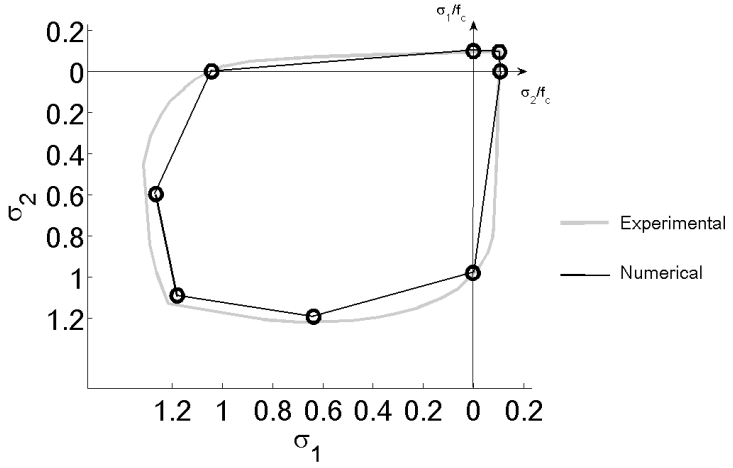

Figure 5.9: Experimental and numerical biaxial failure domain

5.1.2 Biaxial Behavior

The capability of the model to represent biaxial stress states in concrete elements has been tested against the classical study of Kupfer [82]. In this work, the authors tested 200mm by 200mm square panels, with out of plane thickness equal to 50mm. The biaxial loading condition was applied through steel plates, while keeping the ratio between the macroscopic stress applied constant during the tests. The experimental results have already been discussed (see Fig. 2.13) and the comparison with the numerical results is shown.

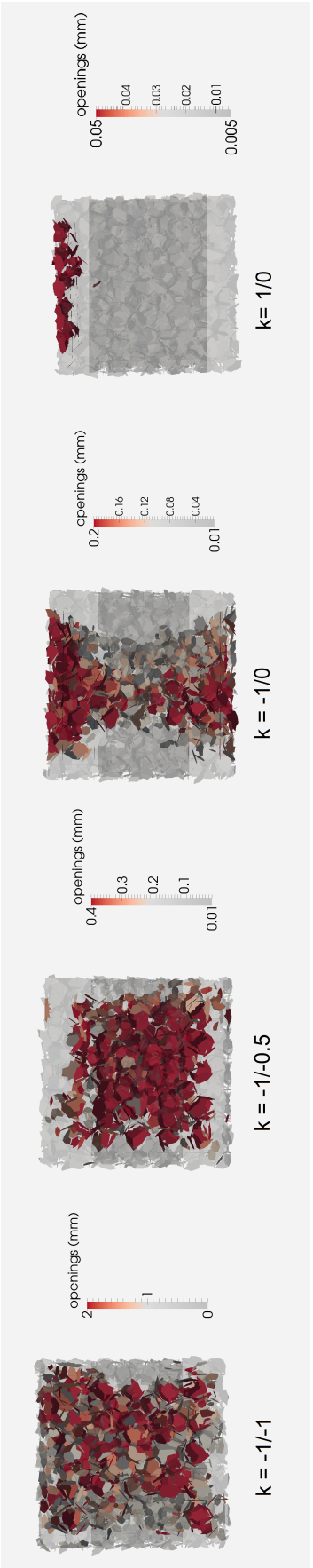

Figure 5.10: Failure modes of prisms under different biaxial stress states

Fig. 5.9 shows the numerical prediction of the $\sigma_1 - \sigma_2$ domain obtained. The model is able to predict the increase in compressive strength due to biaxial stress states.

It is worth noticing that only one set of parameters has been used in all the simulations. Such parameters have been calibrated on the uniaxial compressive test, to obtain the same stiffness and strength as the one measured in the experiments. This set of values of the mechanical properties is able to predict both tensile and multiaxial compressive states, being this one of the unique feature of random lattice particle models.

Also, the correct prediction of different failure modes is one of the main features of the lattice particle method, since the material heterogeneity is explicitly taken into account. Classical continuum mechanics-based fine element models would predict uniform stress and strain for some of the discussed cases, leading to incorrect results or forcing the user to impose damage localization in a certain zone, biasing the obtained results. This aspect is particularly evident by analyzing the case of the biaxial tension experiment conducted in this study. Seen the uniform stress field in the element, continuum mechanics theories are not able to predict the localization of damage in the element, with the consequence that the numerically evaluated crack patterns are undetermined and only influenced by numerical roundoff. The lattice particle model here presented, by modeling the concrete mesostructure, is capable of predicting a diagonal crack line in this case, as observed during lab tests. A comparison of the numerical and experimental crack pattern at failure is given in Fig. 5.11.

5.1.3 Fracturing Behavior

The fracturing and splitting behavior of concrete under different loading conditions has also been analyzed. Different sets of tests available in literature have been numerically simulated. The results of such investigation are reported in the next sections.

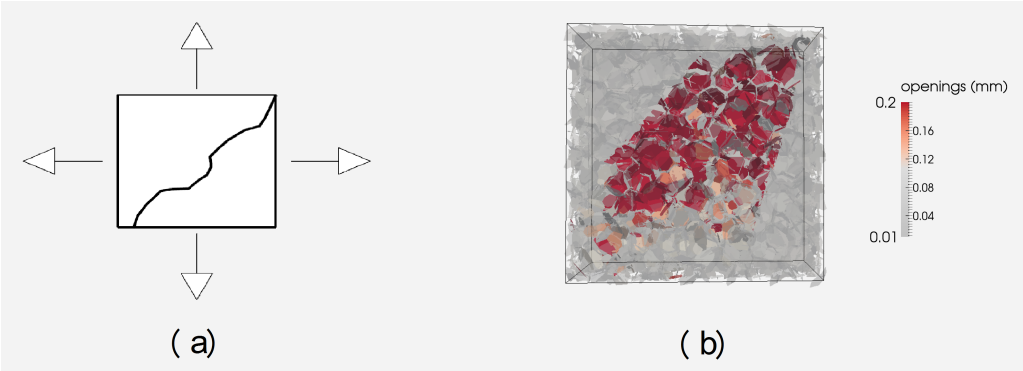

Figure 5.11: Experimental and numerical crack patterns at failure for biaxial tension

Table 5.4: Values of the mechanical properties used in the simulations for the tests performed by Kupfer et al. [82]

σ_t (MPa)	4.6	$G_s(N/mm)$	0.16
σ_c (MPa)	78	K_c	13125
σ_s (MPa)	9.5	k_{c1}	1
E (MPa)	52500	k_{c2}	5
α	0.25	n_t	2
G_t (N/mm)	0.04	n_c	1

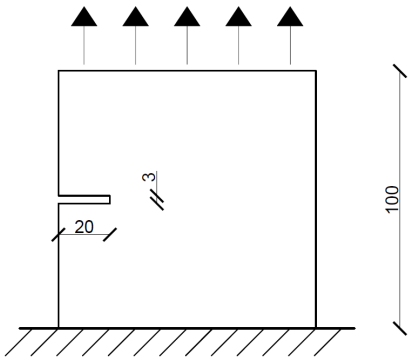

Figure 5.12: Test setup and dimensions of the notched specimen under uniaxial tensile stress

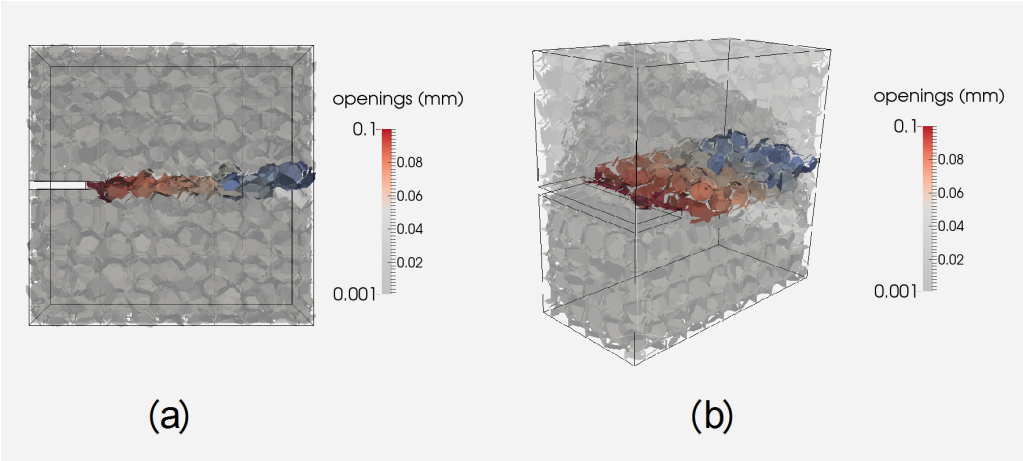

Figure 5.13: Numerically evaluated crack patterns for the notched specimen under uniaxial tension: (a) lateral view; (b) 3-d view

Tensile Tests on Notched Specimens

Fig. 5.12 shows the test setup. A notched specimen of dimensions 100mm by 100mm, with thickness equal to 50mm has been tested under tension [40]. The model is able to predict both the force-displacement curve and the observed crack pattern (shown in Fig. 5.14 and 5.13, showing a crack orthogonal to the direction of the tensile load applied, which starts from the edge of the notch and propagates up to failure.

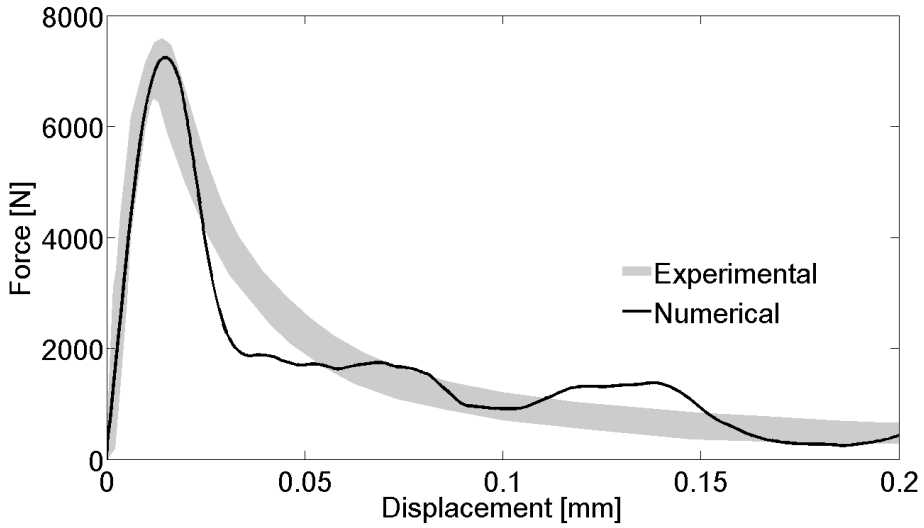

Figure 5.14: Force-displacement curve for the notched specimen under uniaxial tension

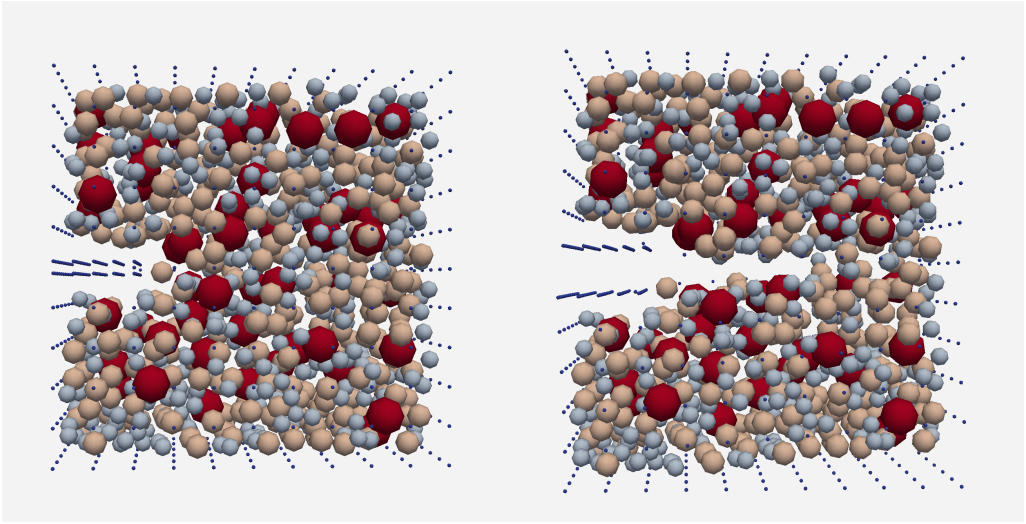

Figure 5.15: Initial and final (amplified 100x) state for the notched specimen tensile test

Table 5.5: Values of the mechanical properties used in the simulations for the tensile test on notched specimen

σ_t (MPa)	4	$G_s(N/mm)$	0.1
σ_c (MPa)	78	K_c	13750
σ_s (MPa)	12	k_{c1}	1
E (MPa)	55000	k_{c2}	5
α	0.25	n_t	2
G_t (N/mm)	0.025	n_c	1

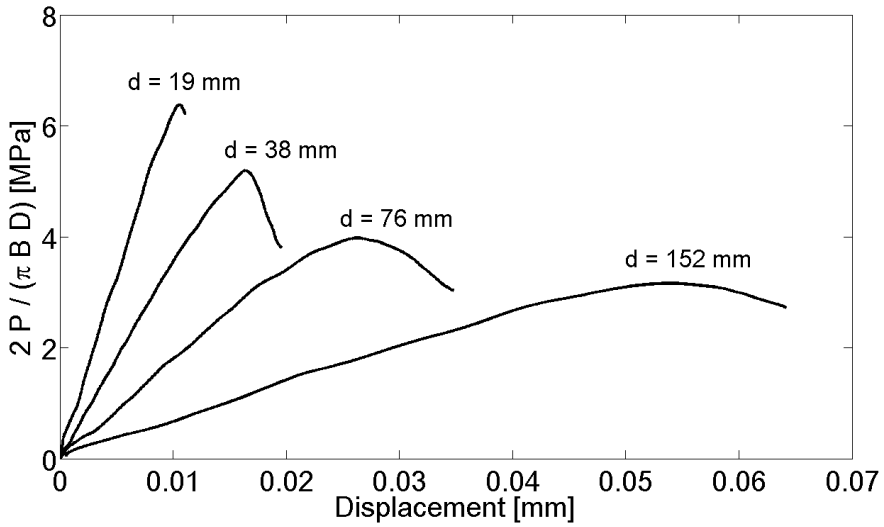

Figure 5.16: Estimated tensile strength for different diameters in Brazilian splitting tests

Table 5.6: Values of the mechanical properties used in the simulations for the tests performed by Bazant al. [21]

σ_t (MPa)	4	$G_s(N/mm)$	0.1
σ_c (MPa)	78	K_c	13750
σ_s (MPa)	12	k_{c1}	1
E (MPa)	55000	k_{c2}	5
α	0.25	n_t	2
G_t (N/mm)	0.025	n_c	1

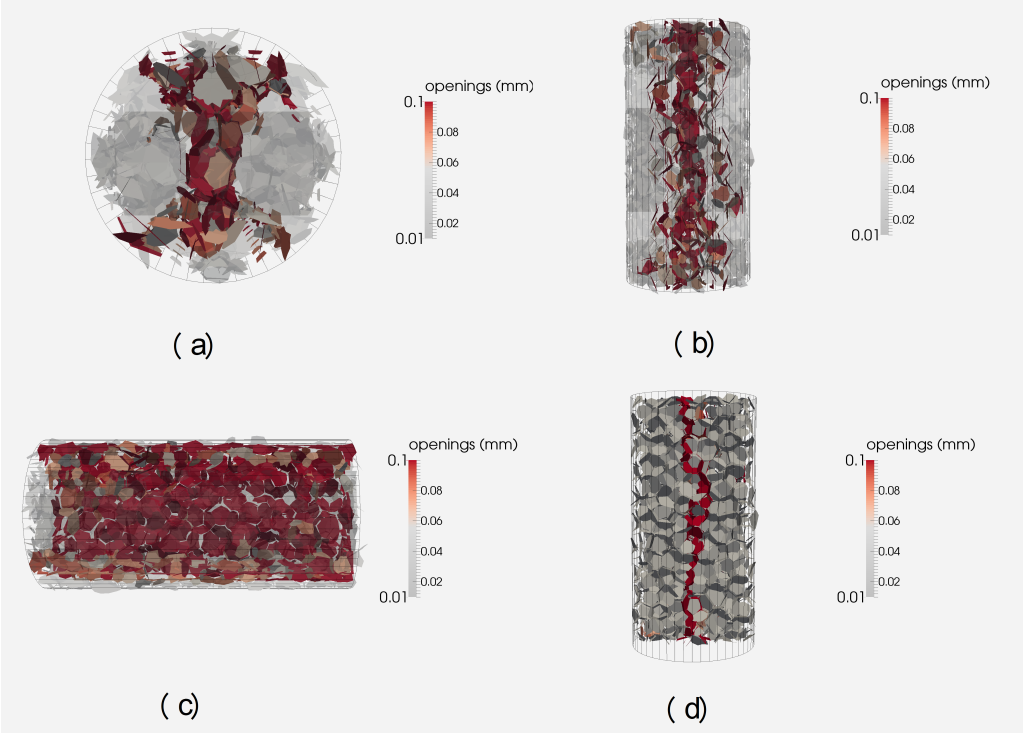

Figure 5.17: Typical failure mode for the Brazilian splitting tests: (a) front view, (b) bottom view, (c) side view, (d) section view

Brazilian Splitting Tests

The experimental campaign performed by Bazant et al. [21] has been simulated. The work aims to the investigation of the size effect on the evaluated tensile strength f_t by using Brazilian splitting tests [104]. While keeping the length of all the specimens equal to 51mm, cylinders with different diameters were used. The experimental and numerical results obtained are reported in Fig. 5.16 in terms of the estimated tensile strength versus displacement.

It is shown how the model is able to correctly predict the tensile forces arising orthogonally to the applied loads. Also, experimental evidences show how the predicted tensile strength reduces as the specimen diameter increases. The random lattice particle model presented is able to capture this aspect, as shown in Fig. 5.17.

5.2 Spring Network

The previously presented numerical results, obtained by means of the *fully dynamic model* will be compared with the ones obtained by the *spring network* model in the next sections. The results will be compared by keeping the same randomly generated distribution for every specific set of specimens tested. The main differences between the two approaches have already been described in Sec. 3, and the differences between the parameters used and their value will be given in Sec. 5.3.

5.2.1 Uniaxial Compression

The uniaxial compressive tests performed in the multiscale experimental campaign have been numerically modeled by means of the spring network model. The peculiarities of such modeling technique have already been discussed in Sec. 3.4, with the main advantages being represented by the lower computational effort and the capability of integrating the equations of motion by means of a static scheme.

The next sections will present the results of the same set of experimental tests earlier presented (see Sec. 5.1), while the comparison between the two modeling approaches will be given in 5.3.

Cubical Specimens

The comparison between the experimental and the numerical simulation of the uniaxial compression tests performed on cubical specimens is presented in this section.

Such comparison shows how the model is capable of predicting the stress-strain curve and failure mode. Fig. 5.19 shows how the numerical simulation correctly reproduces the lateral expansion of the specimen, with the subsequent expulsion of material that leads to the strain-softening behavior. Fig. 5.18 shows how the model is capable of predicting peak stress, strain and the slope of the post-peak behavior. It is worth noticing that

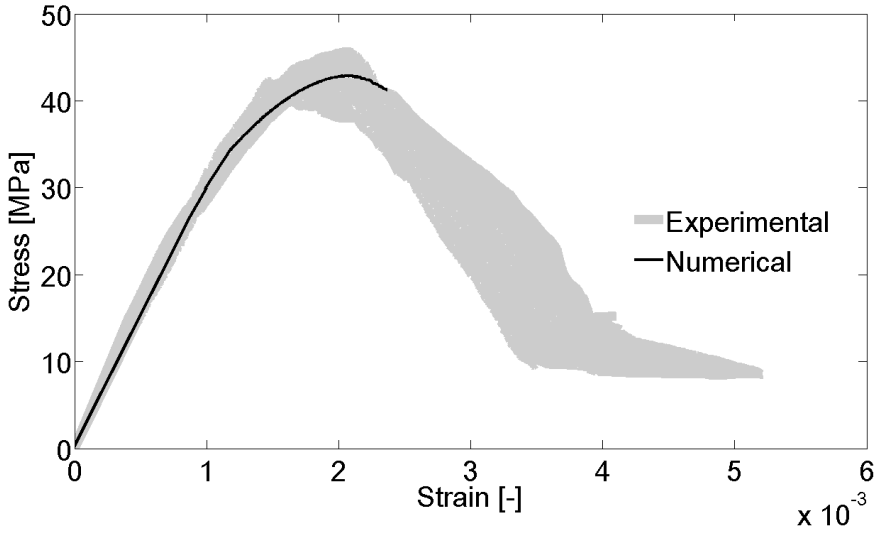

Figure 5.18: Cubical specimen: numerical vs experimental

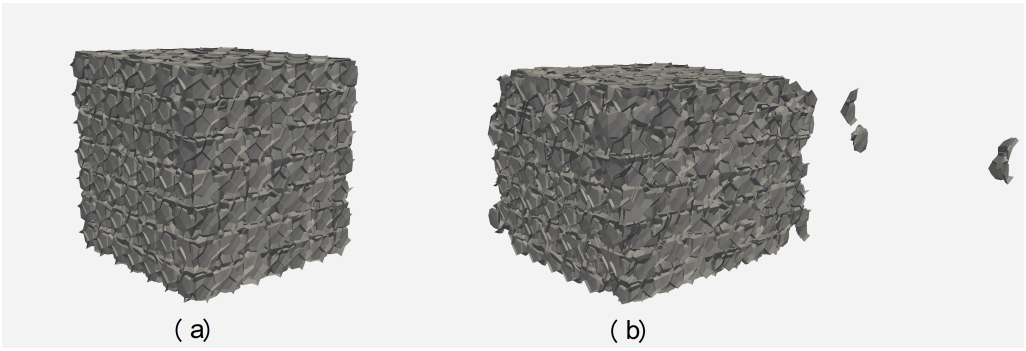

Figure 5.19: Cubical specimen: (a) initial and (b) final deformed (amplified 50x) shape

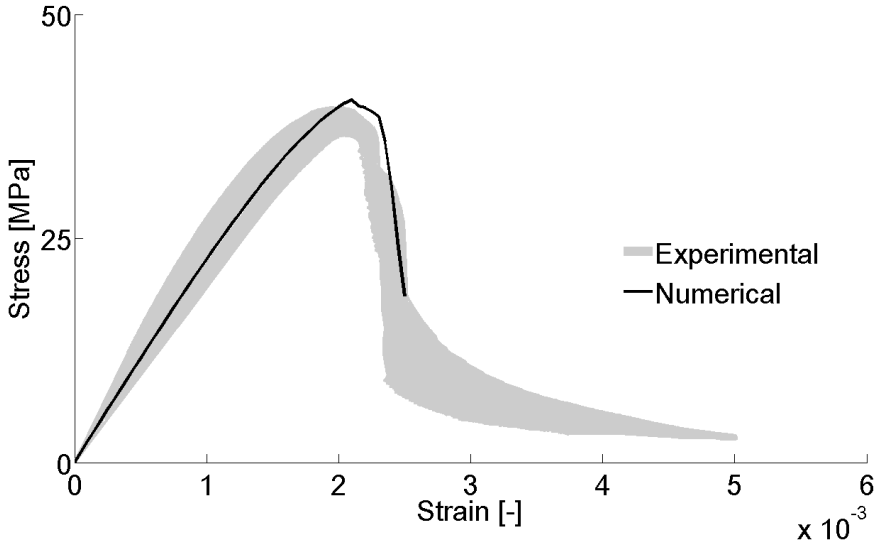

Figure 5.20: Cylindrical specimens: numerical vs experimental

the static integration scheme used in the spring network model fails after the peak due to the singularity of the stiffness matrix. When one or more aggregate pieces get expelled by the element, in fact, the degrees of freedom associated with the particles have near-zero stiffness terms that lead to a singular matrix. This phenomenon is shown in Fig. 5.18.

Cylindrical Specimens

The comparison between the experimental and the numerical simulation of the uniaxial compression tests performed on cylindrical specimens is presented in this section.

Such comparison shows how the model is capable of predicting the stress-strain curve measured during the tests (see Fig. 5.20). The failure mode observed in the tests exhibit a macroscopic shear band spreading from the top of the specimen. While the damage localization zone is still captured by the simulation, the top and bottom part of the elements are not damaged (see Fig. 5.21). This is due to the choice of not including shear stiffness in the formulation of the constitutive law of the lattice struts. This aspect will be discussed in Sec. 5.3.

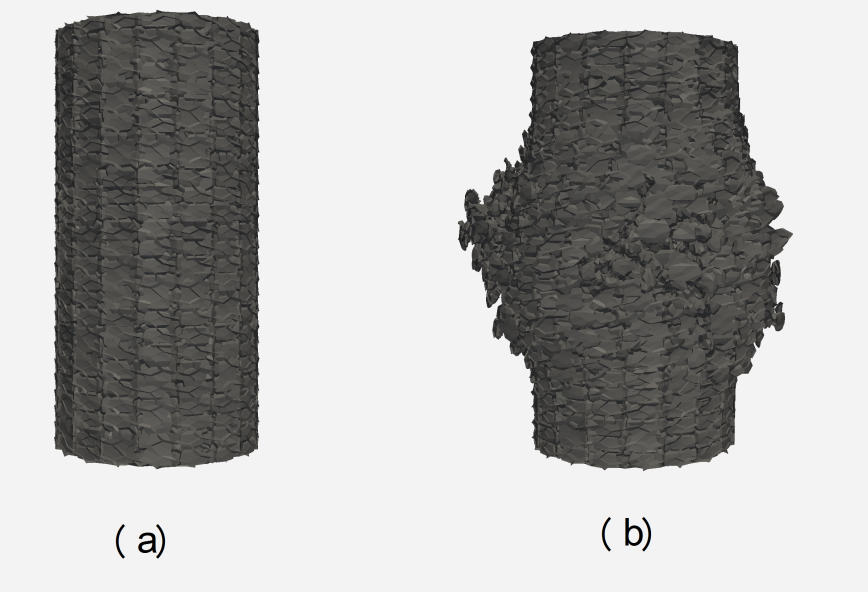

Figure 5.21: Cylindrical specimen: (a) initial and (b) final (amplified 50x) deformed shape

5.2.2 Fracturing Behavior

The spring network model has also been tested against experimental tests involving the fracturing (i.e. tensile) behavior of concrete. The results for both uniaxial tension on notched specimens and indirect tensile tests will be presented in the next sections.

Tensile Tests on Notched Specimens

The uniaxial tension experiment performed on notched specimens has been numerically simulated by means of the spring network model. Fig. 5.22 shows the obtained results in terms of the force-displacement curve. Fig. 5.23 shows the initial and the deformed (amplified $100x$) shape at failure. The model is capable of localizing the damage at the edge of the notch, showing a crack spreading across the member. The direction of the damaged zone, though, is not perfectly orthogonal. Comparison with the results obtained from the fully dynamic model will be given in the next Section.

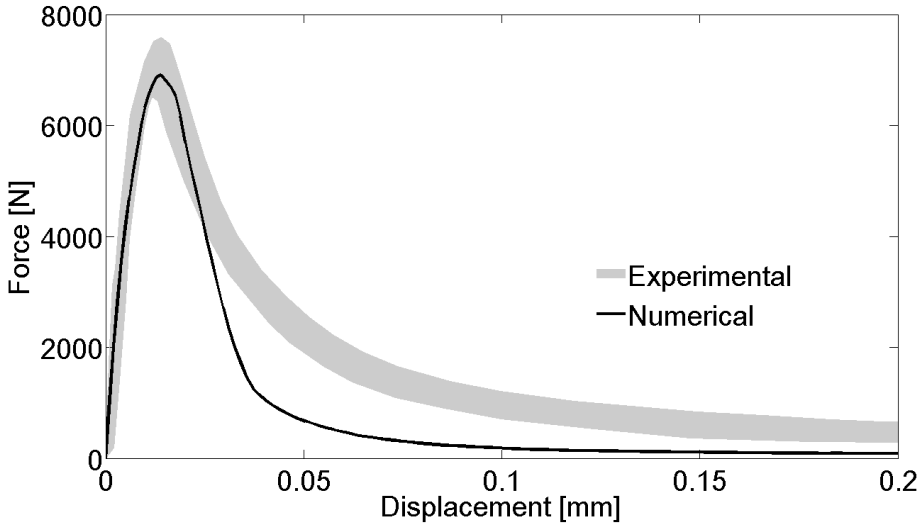

Figure 5.22: Force-displacement curve for the notched specimen under uniaxial tension

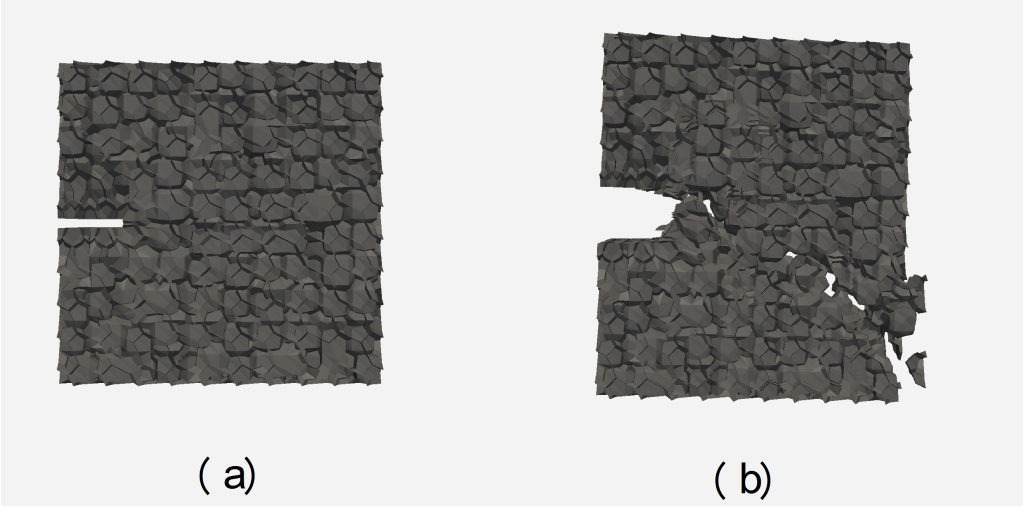

Figure 5.23: Notched specimen: (a) initial and (b) final (amplified $100x$) deformed shape

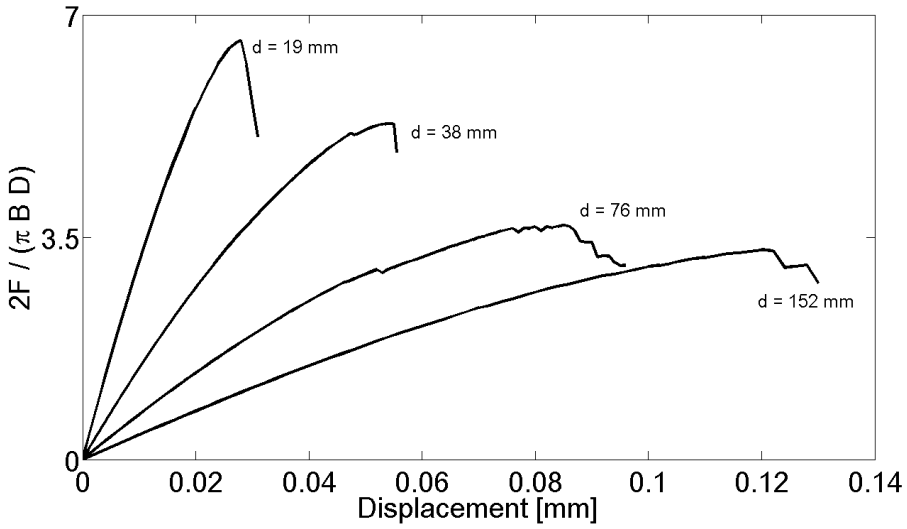

Figure 5.24: Estimated tensile strength for different diameters in Brazilian splitting tests

Brazilian Splitting Tests

The experimental campaign performed by Bazant et al. [21] has been simulated by means of the spring network model. Fig. 5.24 shows the different normalized force vs displacement curves obtained. The model is able to correctly predict how the estimated tensile stress decreases as the diameter of the specimen increases. Fig. 5.25 shows the initial and final deformed shape predicted by the model. The macroscopic tensile crack that leads to the failure of the element, parallel to the direction of the applied load, is correctly reproduced by the numerical model.

A comparison of the results obtained with the different modeling approaches will be given in Sec. 5.3.

5.3 Comparison

A comparison between the numerical results obtained with the *fully dynamic model* and the *spring network model* will be given in this section.

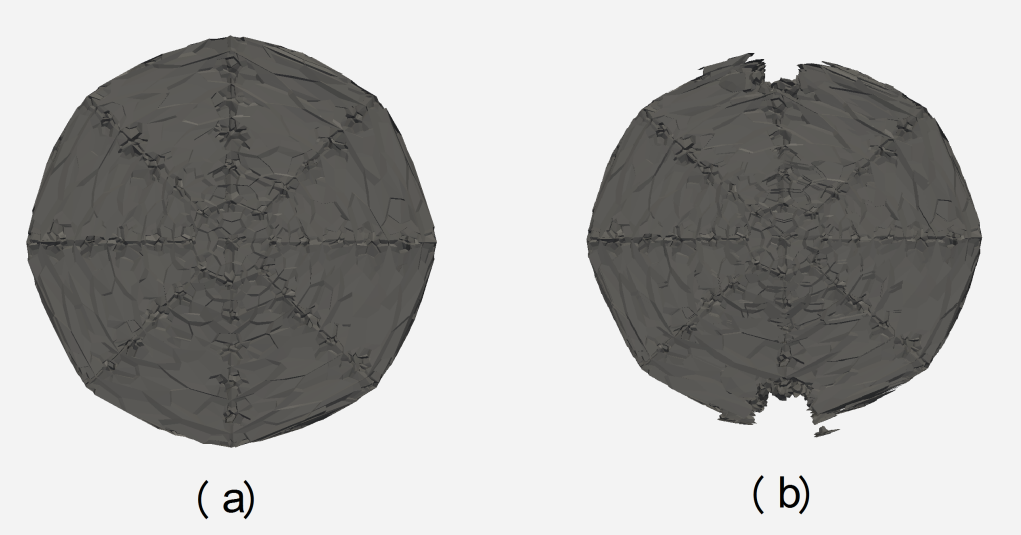

Figure 5.25: Brazilian test (d = 152 mm): (a) initial and (b) final (amplified $250x$) deformed shape

5.3.1 Uniaxial Compression

The uniaxial compressive behavior of concrete elements was investigated. The comparison between the numerical results obtained with the two different approaches will be presented in the following sections.

Cubical Specimens

The numerical results obtained with the two different approaches have already been presented. Fig. 5.26 shows the comparison between the numerically evaluated stress-strain curves. While the elastic behavior can still be reproduced by both models, the fully dynamic one proves more reliable in the prediction of the post-peak behavior. The former approach, also, allows for the control of the steepness of the softening branch, by varying the G_s/G_t ratio (full details are given in Chapter 6).

Moreover, the crack path at failure is more realistically reproduced by the fully dynamic model (see Fig. 5.2 and 5.3) which predicts the "hourglass" shape together with the formation of a major diagonal shear band, as observed in the lab tests. Fig. 5.18 shows how the spring network model captures the overall behavior of the element, but the lack of the

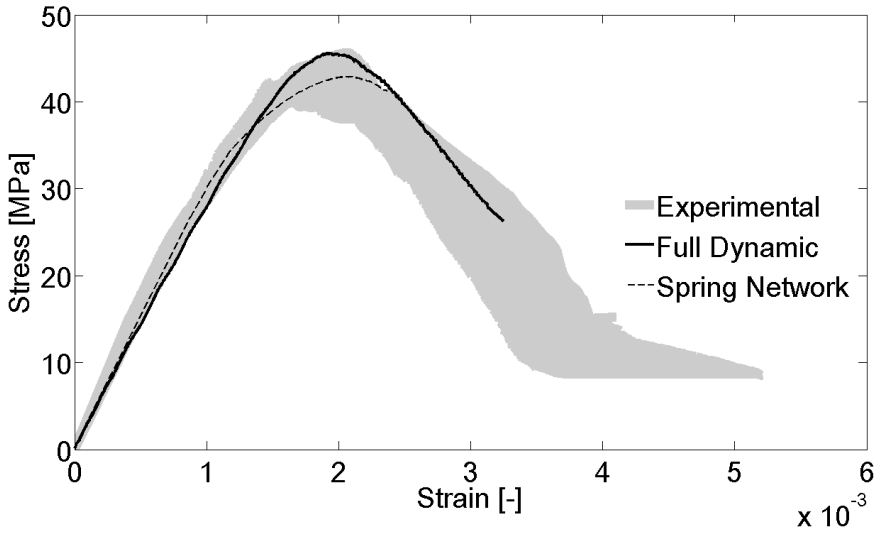

Figure 5.26: Cubical specimen: fully dynamic vs spring network models

transversal behavior of the lattice struts results in a less realistic predicted crack distribution.

Cylindrical Specimens

This section will deal with the comparison of the results obtained from the two different modeling approaches. The numerically evaluated stress-strain curves are reported in fig. 5.27. The elastic behavior is correctly reproduced by both models, the peak strength and strain values are captured, as well as the post-peak behavior. As already mentioned, the fully dynamic model is capable of representing the desired post-peak ductility while the spring network model exhibits a more brittle response on the uniaxial test performed.

The crack path at failure evaluated by means of the fully dynamic model matches the experimental evidences (see Fig. 5.6), which predicts a major shear band running at an angle of approximately $\pi/4$ with respect to the horizontal direction. Fig. 5.21, instead, shows how the spring network model predicts a different failure mode for the examined case, showing a lateral expulsion of the elements undergoing tension, but no diagonal shear band.

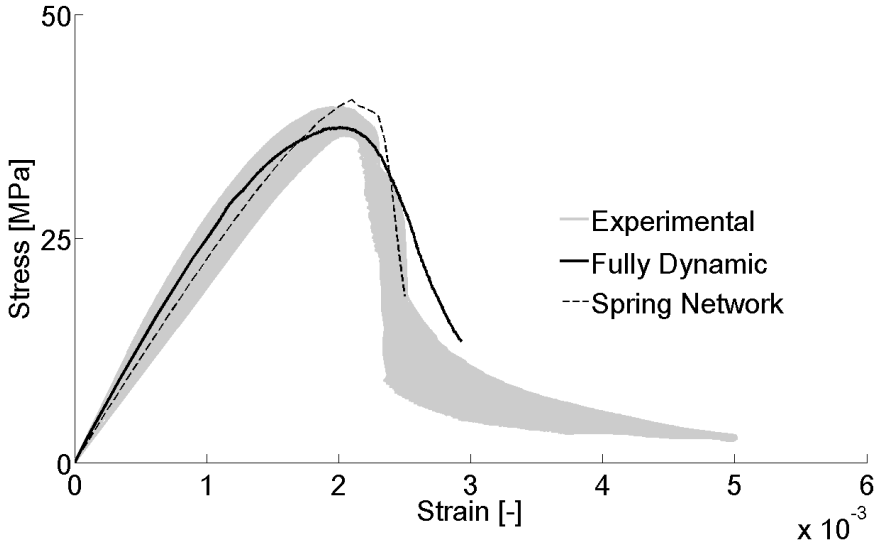

Figure 5.27: Cylindrical specimen: fully dynamic vs spring network models

5.3.2 Fracturing Behavior

Tensile Tests on Notched Specimens

Fig. 5.28 shows the numerically evaluated stress-strain curves obtained by means of the different modeling techniques. The behavior of the notched specimen subject to tension is correctly predicted by both models, being the processes dominated by fracture Mode I. It is shown how the fully dynamic and the spring network models can predict the peak load and displacement values, together with the strain-softening response.

The crack path at failure predicted by the dully dynamic model matches the experimental evidences (see Fig. 5.13), exhibiting a macroscopic crack starting at the edge of the notch and running in a plane perpendicular to the applied load. The spring network model correctly predicts the damage to start at the notch edge, but shows an inclined crack with respect to the direction of the applied load (see Fig. 5.23).

Brazilian Splitting Tests

This section will deal with the comparison of the results obtained by means of the two different modeling techniques presented. Fig. 5.29 shows

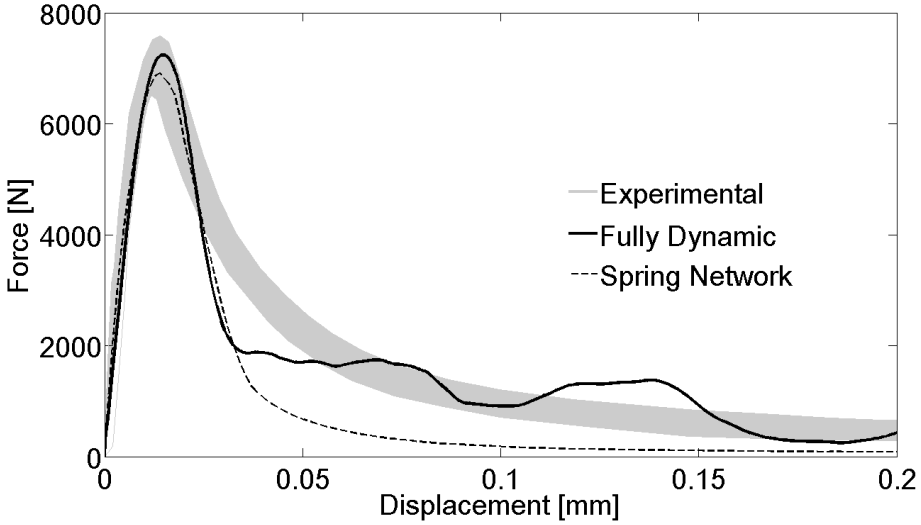

Figure 5.28: Notched specimen: fully dynamic vs spring network models

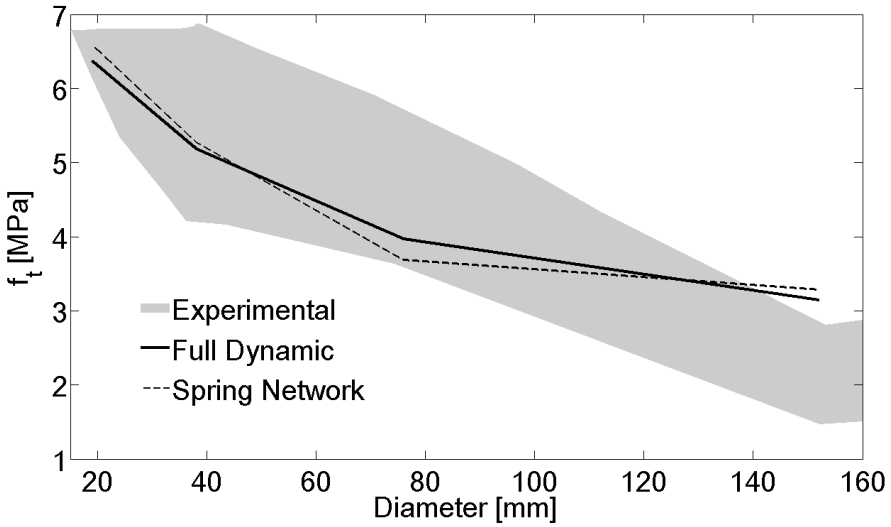

Figure 5.29: Brazilian splitting tests: fully dynamic vs spring network models

the results of the splitting Brazilian tests performed on cylinder of different diameters. The reduction in the estimated tensile strength caused by the increase of the specimen size is correctly reproduced by both models.

The fully dynamic model is capable of representing the crack pattern at failure (see Fig. 5.17). Since the simulated tests are dominated by fracture Mode I, the spring network model also proves capable of representing the macroscopic crack parallel to the plane of the applied load that leads to the failure of the element.

Chapter 6

Conclusions

The present work has dealt with the definition of a random lattice particle model. Two possible approaches have been presented, each one of them presenting peculiarities and unique features: (1) a fully dynamic model, which takes into account shear behavior of the struts and particle rotations, (2) a spring network model, in which only the axial interaction among adjacent cells is considered. The two versions of the model have been implemented in a specifically written computer program, and their features will be discussed separately.

The fully dynamic random lattice particle model has been defined on the basis of existing models in literature [58] [55] [26] but presents new unique features:

- the constitutive law stress boundary is defined as an ellipse in the $\sigma_N - \sigma_T$ space, with the advantage of having a continuous law to define such limit. Also, this choice makes it possible to describe both cohesive ($\epsilon_N > 0$) and frictional ($\epsilon_N < 0$) behavior with the same function, greatly simplifying the definition of the material response at the mesoscopic level

- the nonlinear post-peak response of the struts shows a smooth transition from pure tension to pure shear to compression, thanks to the

continuity of the law used to define the softening modulus H as a function of the coupling strain ω

- the constitutive law is applied on the geometrical center of mass of the resisting cross area of the strut. The volumetric deformation of the connections is evaluated as the weighted average of the values acting on the different facets contained in all the tetrahedrons insisting on that edge. The information on the volumetric strain is used to calculate the hardening modulus used in the post-peak branch of the compressive response, which shows a perfectly-plastic behavior for positive volumetric deformation and a hardening response for negative ones

- the central difference scheme used to numerically integrate the equation of motion is highly parallelized in order to reduce the computational time required for the simulations

- the post-processing of the calculated data is performed through the open source software ParaView [3], and the data exchange between Matlab and the post-processor is performed by a specifically written Python script

The so defined model proved efficient in the description of both the stress-strain response and crack pattern at failure for a wide range of tests performed on concrete elements (see Sec. 5.1). In particular, the model was able to predict the peak strength and strain for uniaxial and biaxial compressive states, as well as the slope of the post-peak curve. The numerically evaluated crack patterns showed an excellent agreement with the ones obtained in the lab tests.

The full model relies on the definition of 12 parameters. The definition of such quantities has been given in Sec. 3.3.2 and their influence on the macroscopic behavior of the lattice is described below.

- E_N (Young's modulus in normal direction) and $\alpha = E_T/E_N$ govern the elastic behavior of the lattice. In particular, approximated relationships can be evaluated in order to predict the macroscopic stiffness and Poisson's Ratio of the lattice

- tensile strength σ_t and the corresponding fracture energy G_t govern the tensile behavior of the lattice and consequently their relevance is stronger in numerical simulations involving tensile fracture processes (Mode I)

- shear strength σ_s and the corresponding fracture energy G_s govern the frictional behavior of the connections. Such parameters affect the lattice behavior in compression, but have limited influence on the tensile resistance

- compressive strength σ_c and hardening modulus K_c govern the macroscopic compression, in particular they have a strong influence on multiaxial compressive states. The two parameters k_{c1} and k_{c2} control the variation of the hardening modulus with respect to the averaged volumetric strain acting in the connection

- Softening exponents n_t and n_c govern the transition of the softening slope from tension ($\omega = \pi/2$) to pure shear ($\omega = 0$) and compression ($\omega = -\pi/2$), and they are defined in such a way the transition among all the possible states is smooth. These parameters only affect the ductility of the lattice, since they control how the softening modulus H changes in-between the 3 just mentioned known states. By increasing n_t and/or decreasing n_c the response tends to be more ductile

By exploiting the results obtained by means of the full model, a simplified approach has been proposed, in which the lattice struts only share axial forces. This choice greatly reduces both the needed parameters and the computational costs involved (particle rotations can be neglected so that,

for a given number of particles, the total degrees of freedom is equal to one half of the total unknowns of the corresponding full model). It has been recognized that such model cannot incorporate frictional effects, due to the lack of shear strength and stiffness. This means that the behavior in the direction transversal to the element axis can only be lumped in the axial response of the connection.

The so constructed model has the following features:

- the equations of motion can be solved statically
- the tensile behavior is history dependent and shows strain-softening in the post-peak branch. The slope of the exponential stress decay is governed by the tensile fracture energy provided
- the compressive response is perfectly plastic if the averaged volumetric strain is positive, hardening for all the other cases
- the model is computationally extremely efficient

The spring network model requires to define 7 parameters, described below.

- the value of E (Young's modulus) governs the elastic behavior of the lattice. In particular, the same approximated laws derived for the full model can be used, by imposing $\alpha = 0$ (no shear stiffness), it is not possible to control the macroscopic Poisson's Ratio
- tensile strength σ_t and the corresponding fracture energy G_t govern the tensile behavior of the lattice struts. Since this is the only kind of mesoscale damage the model is able to reproduce, phenomena dominated by tension (such as direct tension and splitting tests) are correctly simulated by this model
- compressive strength σ_c and its hardening modulus K_c govern the macroscopic compression, in particular they have a strong influence on

multiaxial compressive states. The two parameters k_{c1} and k_{c2} control the variation of the hardening modulus with respect to the averaged volumetric strain acting in the connection

Based on the just defined features and drawbacks of the two methods, and according to the numerical results presented in Chapter 5, it has been shown that the *fully dynamic model* is capable of representing a wide range of fracture processes in cementitious materials (such as uni- and bi-axial compression, fracturing and splitting behavior) in terms of both the load-displacement curve and the crack pattern at failure. On the other hand, the *spring network model* is a simplified version of the former, and it is able to numerically simulate fracture phenomena controlled by Mode I with a satisfactory accuracy, seen the lower computational cost involved.

Together with the definition of the two models, a *multiscale* experimental campaign has been performed, by testing two different concretes at two different scales:

- a *mesoscale concrete*, produced by using aggregate of maximum diameter equal to the lowest diameter explicitly modeled in the numerical simulations, has been cast in cylinders of dimensions similar to the average size of the lattice struts. Tensile, shear and compression tests have been conducted on such specimens

- a *macroscale concrete*, produced by using the complete aggregate curve has been cast in cubes and cylinder of the usual dimensions used for experiments. A total of 9 compressive tests have been performed on such specimen

The term multiscale is used because the two materials represent different scales of the same material. The mesoscale concrete is thought to be describing the response of the mortar lying in-between coarse aggregate pieces. The particle dimensions used in the numerical simulations reflects the size of the aggregate used in the casting of the two types of concrete. This

means that the information obtained from the mesoscale concrete tests can be used in the lattice particle model to investigate the behavior of concrete at the macroscale. Comparison between numerical and experimental tests showed that by using the evaluated mesoscale material properties the model is able to predict the correspondent macroscale quantities.

Bibliography

[1] M. Modeer A. Hillerborg and P. Petersson. "Analysis of Crack Formation and Crack Growth in Concrete by Means of Fracture Mechanics and Finite Elements". In: *Cement and Concrete Research* 6 (1976), pp. 773–781.

[2] Duff A Abrams. "Effect of Time of Mixing on the Strength and Wear of Concrete". In: *Am Concrete Inst Journal & Proceedings* (1918).

[3] James Ahrens, Berk Geveci, and Charles Law. "ParaView: An End-User Tool for Large-Data Visualization". In: *The Visualization Handbook* (2005), p. 717.

[4] Pierre-Claude Aitcin. *High-Performance Concrete*. CRC Press, 2011.

[5] Pierre-Claude Aitcin and P Kumar Mehta. "Effect of Coarse Aggregate Characteristics on Mechanical Properties of High-Strength Concrete". In: *ACI Materials Journal* 87.2 (1990).

[6] Mohammed Alnaggar, Gianluca Cusatis, and Giovanni Di Luzio. "Lattice Discrete Particle Modeling (LDPM) of Alkali Silica Reaction (ASR) Deterioration of Concrete Structures". In: *Cement and Concrete Composites* 41 (2013), pp. 45–59.

[7] AHM Andreasen. "Uber die Beziehung zwischen Kornabstufung und Zwischenraum in Produkten aus losen Kornern (mit einigen Experimenten)". In: *Kolloid-Zeitschrift* 50.3 (1930), pp. 217–228.

[8] D Asahina et al. "Simulating the Poisson Effect in Lattice Models of Elastic Continua". In: *Computers and Geotechnics* 70 (2015), pp. 60–67.

[9] *ASTM C 125 - Standard Terminology Relating to Concrete and Concrete Aggregates*. Active Standards.

[10] *ASTM C 29 - Standard Test Method for Bulk Density (Unit Weight) and Voids in Aggregate*. Active Standards.

[11] Byong Youl Bahn and Cheng-Tzu Thomas Hsu. "Stress-Strain Behavior of Concrete Under Cyclic Loading". In: *ACI Materials Journal* 95.2 (1998).

[12] G. Barrenblatt. "The Formation of Equilibrium Cracks During Brittle Fracture, General Ideas and Hypothesis, Axially Symmetric Cracks". In: *Journal of Applied Mathematics and Mechanics* 22 (1959), pp. 622–636.

[13] Klaus-Jürgen Bathe. *Finite Element Procedures*. Klaus-Jurgen Bathe, 2006.

[14] Z. Bazant. "Crack Band Model for Fracture of Geomaterials". In: *4th International Conference of Numerical Methods in Geomechanics* 3 (1982), pp. 1137–1152.

[15] Z. Bazant. "Instability, Ductility, and Size Effect in Strain-Softening Concrete". In: *Journal of the Engineering Mechanics Division* 12 (1976), pp. 331–344.

[16] Z. Bazant and F. Lin. "Nonlocal Smeared Cracking Model for Concrete Fracture". In: *Journal of Structural Engineering* 114 (1988), pp. 2493–2510.

[17] Z. Bazant and B. Oh. "Crack Band Theory for Fracture of Concrete". In: *Materials and Structures* 16 (1983), pp. 155–177.

[18] Z. Bazant and B. Oh. "Microplane Model for Progressive Fracture of Concrete and Rock". In: *Journal of Engineering Mechanics* 111 (1985), pp. 559–582.

[19] Z. Bazant and J. Ozbolt. "Nonlocal Microplane Model for Fracture, Damage, and Size Effect in Structures". In: *Journal of Engineering Mechanics* 116 (1990), pp. 2485–2505.

[20] Z. Bazant and G. Pijaudier-Cabot. "Nonlocal Continuum Damage, Localization Instability and Convergence". In: *Journal of Applied Mechanics* 55 (1988), pp. 287–293.

[21] Zdenek P Bazant and Jaime Planas. *Fracture and Size Effect in Concrete and Other Quasibrittle Materials*. Vol. 16. CRC press, 1997.

[22] Zdenek P Bazant et al. "Size Effect in Brazilian Split-Cylinder Tests: Measurements and Fracture Analysis". In: *ACI Materials Journal* 88.3 (1991), pp. 325–332.

[23] Stefano Berton and John E Bolander. "Crack Band Model of Fracture in Irregular Lattices". In: *Computer methods in applied mechanics and engineering* 195.52 (2006), pp. 7172–7181.

[24] Robert Herman Bogue. "The Chemistry of Portland Cement". In: *Soil Science* 79.4 (1955), p. 322.

[25] J. Bolander and S. Saito. "Fracture Analyses Using Spring Networks with Random Geometry". In: *Engineering Fracture Mechanics* 61 (1998), pp. 569–591.

[26] J. Bolander and N. Sukumar. "Irregular Lattice Model for Quasistatic Crack Propagation". In: *Physical Review B* 71.094106 (2005).

[27] SV Borisov, SA Magarill, and NV Pervukhina. "Analysis of Atomic Structures as the Development of Belovs Lattice Crystallography". In: *Crystallography Reports* 56.6 (2011), pp. 935–940.

[28] *Building Code Requirements for Structural Concrete and Commentary*. ACI 318-14.

[29] Danilo Capecchi, Giuseppe Ruta, and Patrizia Trovalusci. "From classical to Voigts molecular models in elasticity". In: *Archive for history of exact sciences* 64.5 (2010), pp. 525–559.

[30] Danilo Capecchi, Giuseppe Ruta, and Patrizia Trovalusci. "Voigt and Poincarés mechanistic–energetic approaches to linear elasticity and suggestions for multiscale modelling". In: *Archive of Applied Mechanics* 81.11 (2011), pp. 1573–1584.

[31] *Cement - Part 1: Composition, specifications and conformity criteria for common cements*. European Committee for Standardization.

[32] L Paul Chew. "Constrained Delaunay Triangulations". In: *Algorithmica* 4.1-4 (1989), pp. 97–108.

[33] Ronald Cominsky, Rita B Leahy, and Edward T Harrigan. *Level One Mix Design: Materials Selection, Compaction, and Conditioning*. SHRP-A-408. 1994.

[34] *Concrete Part 1: Specification, performance, production and conformity*. UNI EN 206-1.

[35] Upendra J Counto. "The Effect of the Elastic Modulus of the Aggregate on the Elastic Modulus, Creep and Creep Recovery of Concrete". In: *Magazine of Concrete Research* 16.48 (1964), pp. 129–138.

[36] P. Cundall. "A Computer Model for Simulating Progressive Large Scale Movements in Blocky Rocks Systems". In: *Proceedings of the Symposyum of the International Society of Rock Mechanics* 2 (1971).

[37] P. Cundall. "BALL - A Program to Model Granular Media Using the Distinct Element Media". In: *Technical Note* (1978).

[38] P. Cundall and O. Strack. "A Discrete Numerical Model for Granular Assemblies". In: *Geotechnique* 29 (1979), pp. 47–65.

[39] G. Cusatis, Z. Bazant, and L Cedolin. "Confinement-Shear Lattice Model for Concrete Damage in Tension and Compression: II. Computation and Validation". In: *Journal of Engineering Mechanics* 129 (2003), pp. 1449–1458.

[40] G Cusatis, M Polli, and L Cedolin. "Mesolevel Analysis of Fracture Tests for Concrete". In: *Fracture Mechanics of Concrete Structures, Proceedings of the Fifth International Conference on Fracture Mechanics of Concrete and Concrete StructuresFraMCoS-5, Vail Cascade Resort, Vail Colorado, Ia-FraMCos, USA*. 2004, pp. 345–351.

[41] Chandan Dasgupta and Bi Halperin. "Phase Transition in a Lattice Model of Superconductivity". In: *Physical Review Letters* 47.21 (1981), p. 1556.

[42] Ken Day. *Concrete Mix Design, Quality Control and Specification*. CRC Press, 2003.

[43] Boris Delaunay. "Sur la Sphere Vide". In: *Izv. Akad. Nauk SSSR, Otdelenie Matematicheskii i Estestvennyka Nauk* 7.793-800 (1934), pp. 1–2.

[44] Dorothy E Denning. "A Lattice Model of Secure Information Flow". In: *Communications of the ACM* 19.5 (1976), pp. 236–243.

[45] *Design of Concrete Structures. General Rules and Rules for Buildings*. BS EN.

[46] G Lejeune Dirichlet. "Über die Reduction der Positiven Quadratischen Formen mit Drei Unbestimmten Ganzen Zahlen." In: *Journal für die reine und angewandte Mathematik* 40 (1850), pp. 209–227.

[47] D. Dugdale. "Yielding of Steel Sheets Containing Slits". In: *Journal of Mechanics and Physics of Solids* 8 (1960), pp. 100–108.

[48] Herbert Edelsbrunner and Nimish R Shah. "Incremental Topological Flipping Works for Regular Triangulations". In: *Algorithmica* 15.3 (1996), pp. 223–241.

[49] Elsevier, ed. *Fracture Mechanics of Concrete: Concepts, Models and Determination of Material Properties*. ACI Committee. 1992.

[50] A Cemal Eringen and DGB Edelen. "On Nonlocal Elasticity". In: *International Journal of Engineering Science* 10.3 (1972), pp. 233–248.

[51] P. Roelfstra F. Wittman and H. Sadouki. "Simulation and Analysis of Composite Structures". In: *Materials Science and Engineering* 68 (1984), pp. 239–248.

[52] Luciano Feo, Ayman S Mosallam, and Rosa Penna. "Mechanical Behavior of Web-Flange Junctions of Thin-Walled Pultruded I-Profiles: an Experimental and Numerical Evaluation". In: *Composites Part B: Engineering* 48 (2013), pp. 18–39.

[53] Steven Fortune. "A Sweepline Algorithm for Voronoi Diagrams". In: *Algorithmica* 2.1-4 (1987), pp. 153–174.

[54] William B Fuller and Sanford E Thompson. "The Laws of Proportioning Concrete". In: *Transactions of the American Society of Civil Engineers* 59.2 (1907), pp. 67–143.

[55] D. Pelessone G. Cusatis and A. Mencarelli. "Lattice Discrete Particle Model (LDPM) for Failure Behavior of Concrete. I: Theory". In: *Cement and Concrete Composites* 33 (2011), pp. 881–890.

[56] D. Pelessone G. Cusatis A. Mencarelli and J. Baylot. "Lattice Discrete Particle Model (LDPM) for Failure Behavior of Concrete. II: Calibration and Validation". In: *Cement and Concrete Composites* 33 (2011), pp. 891–905.

[57] Z. Bazant G. Cusatis and L. Cedolin. "Confinement-Shear Lattice CSL Model for Fracture Propagation in Concrete". In: *Computer Methods in Applied Mechanics Engineering* 195 (2006), pp. 7154–7171.

[58] Z. Bazant G. Cusatis and L. Cedolin. "Confinement-Shear Lattice Model for Concrete Damage in Tension and Compression: I. Theory". In: *Journal of Engineering Mechanics* 129 (2003), pp. 1439–1448.

[59] Serena Gambarelli, Nicola Nisticò, and Joško Ožbolt. "Microplane Model for Concrete: Part I. State of the Art". In: *Advances in Civil and Infrastructure Engineering* (2015).

[60] Peter Grassl and Milan Jirasek. "Meso-Scale Approach to Modelling the Fracture Process Zone of Concrete Subjected to Uniaxial Tension". In: *International Journal of Solids and Structures* 47.7 (2010), pp. 957–968.

[61] Leslie Greengard and Vladimir Rokhlin. "A Fast Algorithm for Particle Simulations". In: *Journal of computational physics* 73.2 (1987), pp. 325–348.

[62] A. Griffith. "The Phenomenon of Rupture and Flow in Solids". In: *Philosophical Transactions of the Royal Society of London* 221 (1921), pp. 163–198.

[63] A. Griffith. "Theory of Rupture". In: *1st International Congress on Applied Mechanics* (1924), pp. 55–63.

[64] Leonidas J Guibas, Donald E Knuth, and Micha Sharir. "Randomized Incremental Construction of Delaunay and Voronoi Diagrams". In: *Algorithmica* 7.1-6 (1992), pp. 381–413.

[65] MATLAB Users Guide. "The mathworks". In: *Inc., Natick, MA* 5 (1998), p. 333.

[66] A. Gupta and H. Akbar. "Cracking in Reinforced Concrete Analysis". In: *Journal of Structural Engineering* 84 (1984), pp. 135–1741.

[67] J Hardy, O de Pazzis, and Y Pomeau. "Molecular Dynamics of a Classical Lattice Gas: Transport Properties and Time Correlation Functions". In: *Phys. Rev. A* 13 (1976), pp. 1949–1961.

[68] Amy Henderson, Jim Ahrens, Charles Law, et al. *The ParaView Guide*. Kitware Clifton Park, NY, 2004.

[69] Mark D Hill and Michael R Marty. "Amdahl's Law in the Multicore Era". In: *Computer* 7 (2008), pp. 33–38.

[70] A. Hillerborg. "Analysis of one single crack". In: *Fracture Mechanics of Concrete (Developments in Civil Engineering)* (1983), pp. 223–249.

[71] A. Hillerborg. "Numerical Methods to Simulate Softening and Fracture of Concrete". In: *Fracture mechanics of concrete: structural application and numerical calculation* (1985), pp. 141–170.

[72] Teddy J Hirsch. "Modulus of Elasticity of Concrete Affected by Elastic Moduli of Cement Paste Matrix and Aggregate". In: *ACI Journal Proceedings*. Vol. 59. 3. ACI. 1962.

[73] A. Hrennikoff. "Solution of Problems of Elasticity by the Framework Method". In: *Journal of Applied Mechanics* 12 (1941), pp. 169–175.

[74] T. Shiraishi J. Bolander and Y. Isogawa. "An Adaptive Procedure for Fracture Simulation in Extensive Lattice Networks". In: *Engineering Fracture Mechanics* 54 (1996), pp. 325–334.

[75] Daniel C Jansen and Surendra P Shah. "Effect of Length on Compressive Strain Softening of Concrete". In: *Journal of Engineering Mechanics* 123.1 (1997), pp. 25–35.

[76] Ray A Jarvis. "On the Identification of the Convex Hull of a Finite Set of Points in the Plane". In: *Information Processing Letters* 2.1 (1973), pp. 18–21.

[77] Milan Jirásek and Zdenek P Bazant. *Inelastic Analysis of Structures*. John Wiley & Sons, 2002.

[78] T. Kawai. "Some Considerations on the Finite Element Method". In: *International Journal of Numerical Methods in Engineering* 16 (1980), pp. 81–120.

[79] Karl Kordina. *Experiments of the Influence of the Mineralogical Character of Aggregates on the Creep of Concrete*. Ed. by Rilem. Periodic Bullettin, 1958.

[80] E Kroner. "Elasticity Theory of Materials with Long Range Cohesive Forces". In: *International Journal of Solids and Structures* 3.5 (1967), pp. 731–742.

[81] IA Kunin. "The Theory of Elastic Media with Microstructure and the Theory of Dislocations". In: *Mechanics of generalized continua*. Springer, 1968, pp. 321–329.

[82] Helmut Kupfer, Hubert K Hilsdorf, and Hubert Rusch. "Behavior of Concrete Under Biaxial Stresses". In: *ACI Journal proceedings*. Vol. 66. 8. ACI. 1969.

[83] Geo Leach. "Improving Worst-Case Optimal Delaunay Triangulation Algorithms". In: *4th Canadian Conference on Computational Geometry*. Citeseer. 1992, pp. 340–346.

[84] Heather N Lechtman and Linn W Hobbs. "Roman Concrete and the Roman Architectural Revolution". In: *High-Technology Ceramics: Past, Present, and Future-The Nature of Innovation and Change in Ceramic Technology*. Vol. 3. The American Ceramic Society, Inc., 1986, pp. 81–128.

[85] Yong-Hak Lee and K William. "Mechanical Properties of Concrete in Uniaxial Compression". In: *ACI materials journal* 94.6 (1997).

[86] Tony CY Liu, Arthur H Nilson, and Floyd O Slate Floyd. "Stress-Strain Response and Fracture of Concrete in Uniaxial and Biaxial Compression". In: *ACI Journal Proceedings*. Vol. 69. 5. ACI. 1972.

[87] J. Mohle M. Yip and J. Bolander. "Automated Modeling of Three-Dimensional Structural Components Using Irregular Lattices". In: *Computer-Aided Civil and Infrastructure Engineering* 20 (2005), pp. 393–407.

[88] Gro Markeset and Arne Hillerborg. "Softening of Concrete in Compression-Localization and Size effects". In: *Cement and Concrete Research* 25.4 (1995), pp. 702–708.

[89] Christian Meyer. "Concrete as a Green Building Material". In: *Construction Materials Mindess Symposium*. 2005.

[90] Sidney Mindess, J Francis Young, and David Darwin. *Concrete*. Ed. by Pearson Education. Prentice Hall, 2003.

[91] B. Neal. "The Rapid Calculation of the Plastic Collapse Load for a Framed Structure". In: *ICE Proceedings: Engineering Divisions* 1 (1952), pp. 58–71.

[92] Adam M Neville. *Properties of Concrete*. Ed. by Wiley. New York, 1995.

[93] *Norme Tecniche per le Costruzioni*. Italian. Ministero delle Infrastrutture.

[94] JP Ollivier, JC Maso, and B Bourdette. "Interfacial Transition Zone in Concrete". In: *Advanced Cement Based Materials* 2.1 (1995), pp. 30–38.

[95] M. Ortiz. "An Analytical Study of the Localized Failure Modes of Concrete". In: *Mechanics of Materials* 6 (1987), pp. 159–174.

[96] Ronfu Ou and Robert E Fulton. "An Investigation of Parallel Numerical Integration Methods for Nonlinear Dynamics". In: *Computers & Structures* 30.1 (1988), pp. 403–409.

[97] Josko Ozbolt, Yijun Li, and Ivica Kozar. "Microplane Model for Concrete with Relaxed Kinematic Constraint". In: *International Journal of Solids and Structures* 38.16 (2001), pp. 2683–2711.

[98] H. Sadouki P. Roelfstra and F. Wittmann. "Le Beton Numerique". In: *Materials and Structures* 107 (1985), pp. 327–335.

[99] G. Pijaudier-Cabot and Z. Bazant. "Nonlocal Damage Theory". In: *Journal of Engineering Mechanics* 113 (1987), pp. 1512–1533.

[100] Vitruvius Pollio. *Vitruvius: The Ten Books on Architecture*. Harvard university press, 1914.

[101] TC Powers and TL Brownyard. "Studies of the Physical Properties of Hardened Cement Paste". In: *Bull* 22 (1948).

[102] Walter H Price. "Factors Influencing Concrete Strength". In: *ACI Journal Proceedings*. Vol. 47. 2. ACI. 1951.

[103] RILEM Draft Recommendation. "Determination of the Fracture Energy of Mortar and Concrete by Means of Three-Point Bend Tests on Notched Beames". In: *Materials and Structures* 18.106 (1985), pp. 285–290.

[104] C Rocco et al. "Size Effect and Boundary Conditions in the Brazilian Test: Theoretical Analysis". In: *Materials and Structures* 32.6 (1999), pp. 437–444.

[105] P. Roelfstra. "Numerical Analysis and Simulation of Crack Formation in Composite Materials such as Concrete". In: *Fracture of Non-Metallic Materials* (1987), pp. 358–384.

[106] Jim Ruppert. "A Delaunay Refinement Algorithm for Quality 2-Dimensional Mesh Generation". In: *Journal of algorithms* 18.3 (1995), pp. 548–585.

[107] WILLIAM EGBERT Schaap. "DTFE: The Delaunay Tesselation Field Estimator, University of Groningen, The Netherlands, 2007". PhD thesis. Ph. D. Dissertation.

[108] E. Schlangen and J. Van Mier. "Simple Lattice Model for Numerical Simulation of Fracture of Concrete Materials and Structures". In: *Materials and Structures* 25 (1992), pp. 534–542.

[109] H. Schreyer and Z. Chen. "One-Dimensional Softening with Localization". In: *Journal of Applied Mechanics* 53 (1986), pp. 791–797.

[110] Karen L Scrivener, Alison K Crumbie, and Peter Laugesen. "The Interfacial Transition Zone (ITZ) Between Cement Paste and Aggregate in Concrete". In: *Interface Science* 12.4 (2004), pp. 411–421.

[111] A. Serrano and J. Rodriguez-Ortiz. "A Contribution to the Mechanics of Heterogeneous Granular Media". In: *Proc. Symp. Plasticity and Soil Mechanics Cambridge* 1 (1973).

[112] David F Shanno. "Conditioning of Quasi-Newton Methods for Function Minimization". In: *Mathematics of computation* 24.111 (1970), pp. 647–656.

[113] Jonathan Richard Shewchuk. "Sweep Algorithms for Constructing Higher-Dimensional Constrained Delaunay Triangulations". In: *Proceedings of the sixteenth annual symposium on Computational geometry*. ACM. 2000, pp. 350–359.

[114] James M Shilstone Sr. "Concrete mixture optimization". In: *Concrete International* 12.6 (1990), pp. 33–39.

[115] Jovanca Smith et al. "Discrete Modeling of Ultra-High-Performance Concrete With Application to Projectile Penetration". In: *International Journal of Impact Engineering* 65 (2014), pp. 13–32.

[116] *Standard Practice for Selecting Proportions for Normal, Heavyweight, and Mass Concrete (Reapproved 2009)*. ACI.

[117] *Standard Specification for Portland Cement*. Active Standards.

[118] *Standard Test Method for Compressive Strength of Hydraulic Cement Mortars (Using 2-in. or [50-mm] Cube Specimens)*. Active Standards.

[119] *Standard Test Method for Splitting Tensile Strength of Cylindrical Concrete Specimens*. Active Standards.

[120] Peter Su and Robert L Scot Drysdale. "A Comparison of Sequential Delaunay Triangulation Algorithms". In: *Proceedings of the eleventh annual symposium on Computational geometry*. ACM. 1995, pp. 61–70.

[121] P. Symonds and B. Neal. "Recent Progress in the Plastic Methods of Structural Analysis". In: *Journal of the Franklin Institute* 252 (1951), pp. 469–492.

[122] G. Taylor. "Plastic Strain in Metals". In: *Journal of the Institute of Metals* 62 (1938), pp. 307–324.

[123] *Testing Aggregates. Methods for Determination of Particle Size and Shape*. British Standard, 1975.

[124] Jeanne Marie Teutonico et al. "The Smeaton Project: Factors Affecting the Properties of Lime-Based Mortars". In: *APT bulletin* (1993), pp. 32–49.

[125] Patrizia Trovalusci. "Molecular approaches for multifield continua: origins and current developments". In: *Multiscale Modeling of Complex Materials*. Springer, 2014, pp. 211–278.

[126] Patrizia Trovalusci, Danilo Capecchi, and Giuseppe Ruta. "Genesis of the multiscale approach for materials with microstructure". In: *Archive of Applied Mechanics* 79.11 (2009), pp. 981–997.

[127] Richard A Vaia and Emmanuel P Giannelis. "Lattice Model of Polymer Melt Intercalation in Organically-Modified Layered Silicates". In: *Macromolecules* 30.25 (1997), pp. 7990–7999.

[128] MR van Vliet and JG van Mier. "Experimental investigation of concrete fracture under uniaxial compression". In: *Mechanics of Cohesive-frictional Materials* 1.1 (1996), pp. 115–127.

[129] JGM Van Mier et al. "Strain-Softening of Concrete in Uniaxial Compression". In: *Materials and Structures* 30.4 (1997), pp. 195–209.

[130] Johannes Gerardus Maria Van Mier. *Strain-Softening of Concrete Under Multiaxial Loading Conditions*. Technische Hogeschool Eindhoven, 1984.

[131] Jinku Wang, Moran Wang, and Zhixin Li. "A Lattice Boltzmann Algorithm for Fluid-Solid Conjugate Heat Transfer". In: *International Journal of Thermal Sciences* 46.3 (2007), pp. 228–234.

[132] Eric W. Weisstein. *Moore Neighborhood.* MathWorld - A Wolfram Web Resource. http://mathworld.wolfram.com/MooreNeighborhood.html.

[133] M. T. Kazemi Z. Bazant M. Tabbara and G. Pijaudier-Cabot. "Random Particle Model for Fracture of Aggregates or Fiber Composites". In: *Journal of Engineering Mechanics* 116 (1990), pp. 1686–1705.

[134] T. Belytschko Z. Bazant and T. Chang. "Continuum Model for Strain-Softening". In: *Journal of Engineering Mechanics* 110 (1984), pp. 1666–1692.

[135] YB Zaitsev and FH Wittmann. "Simulation of Crack Propagation and Failure of Concrete". In: *Materiaux et Construction* 14.5 (1981), pp. 357–365.

[136] Borut Žalik and Ivana Kolingerová. "An Incremental Construction Algorithm for Delaunay Triangulation Using the Nearest-Point Paradigm". In: *International Journal of Geographical Information Science* 17.2 (2003), pp. 119–138.

[137] A. Zubelewicz and Z. Bazant. "Interface Element Modeling of Fracture in Aggregate Composites". In: *Journal of Engineering Mechanics* 113 (1987), pp. 1619–1630.